



NTNU – Trondheim
Norwegian University of
Science and Technology

Experimental and Numerical Study on the Perforation of Empty and Sand-filled Aluminium Panels

Fredrik Risåsen Bjerke
Lars Magnus Hansen

Civil and Environmental Engineering (2 year)

Submission date: June 2015

Supervisor: Tore Børvik, KT



Co-supervisor: Jens Kristian Holmen, KT

Norwegian University of Science and Technology
Department of Structural Engineering



MASTER'S THESIS 2015

SUBJECT AREA: Computational Mechanics	DATE: 10 June 2015	NO. OF PAGES: 158 18 + 120 + 20
--	-----------------------	------------------------------------

TITLE: Experimental and Numerical Study on the Perforation of Empty and Sand-filled Aluminium Panels Eksperimentelt og numerisk studie på perforasjon av tomme og sand-fylte aluminiumspaneler	
BY: Fredrik Risåsen Bjerke Lars Magnus Hansen	 


SUMMARY: The discrete particle approach has previously proven to give excellent agreement between experiments and numerical analysis for blast and penetration in granular medias. The main objective in this thesis is to further investigate the accuracy of the particle-based approach for penetration in granular materials, and compare the numerical output with conducted experiments. A literature survey on penetration in granular media is also carried out to understand the main mechanisms. Ballistic limit curves and ballistic limit velocities have been identified by experiments performed at SIMLab, NTNU, on empty and sand-filled AA6005-T6 aluminium panels impacted by 7.62 mm APM2 bullets. Three different fractions of granular media have been tested, with a median grain size of 0.15 mm, 0.55 mm and 0.95 mm. The experiments showed minor differences in ballistic limit velocity between each fraction of sand, but an increase of at least 32.5 % is seen when going from empty to sand-filled panels. The non-linear explicit finite element software IMPETUS Afea Solver is employed in the numerical work in this thesis. The parameters in the particle model were calibrated through numerical simulations against gas-gun component tests. In addition, drop-tower component tests were carried out, allowing the particle-based method to be validated over multiple velocity domains. The component experiments and numerical simulations are in good agreement for impacts in the high velocity domain. In the numerical simulations for empty and sand-filled panels a standard Johnson-Cook constitutive relation is used for all structural parts, while fracture is modelled with a Johnson-Cook criterion for the aluminium panel and a Cockcroft-Latham criterion for lead tip and brass jacket. The numerical results were finally compared to experimental observations, which showed that IMPETUS Afea Solver is able to capture the main trends in the perforation process. The influence of various numerical input was also investigated in a rather comprehensive sensitivity study. This showed that the input for the aluminium panel seems reasonable compared to computational cost for the complex model applied in this thesis.
--

RESPONSIBLE TEACHER:	Professor Tore Børvik.
SUPERVISORS:	Professor Tore Børvik and PhD candidate Jens Kristian Holmen.
CARRIED OUT AT:	SIMLab, The Department of Structural Engineering, NTNU.



MASTEROPPGAVE 2015

FAGOMRÅDE: Beregningsmekanikk	DATO: 10. juni 2015	ANTALL SIDER: 158 18+ 120 + 20
----------------------------------	------------------------	-----------------------------------

TITTEL: Eksperimentelt og numerisk studie på perforasjon av tomme og sand-fylte aluminiumspaneler Experimental and Numerical Study on the Perforation of Empty and Sand-filled Aluminium Panels	
UTFØRT AV: Fredrik Risåsen Bjerke Lars Magnus Hansen	

<p>SAMMENDRAG: Den diskrete partikkelmetoden har tidligere gitt utmerket samsvar mellom eksperimenter og numeriske simuleringer for eksplosjonslaster og ballistisk penetrasjon i granulatmaterialer. Hovedmålet med denne oppgaven er å studere modellens nøyaktighet i penetrasjonsproblemer og sammenligne numeriske simuleringer med utførte eksperimenter. Et litteraturstudie innen penetrasjon av sand er utført for å forstå de grunnleggende mekanismene.</p> <p>Ballistiske kurver og ballistiske grenser har blitt funnet for en 7,62 mm APM2-kule for tomme og sand-fylte AA6005-T6 aluminiumspaneler gjennom eksperimenter utført ved SIMLab, NTNU. Tre forskjellige sandtyper med en gjennomsnittlig kornstørrelse på 0,15 mm, 0,55 mm og 0,95 mm har blitt testet. Eksperimentene viste små forskjeller i ballistisk grense mellom hver sandfraksjon. En økning på 32 % ble derimot funnet fra tomme til sandfylte paneler.</p> <p>Det ikke-lineære eksplisitte elementmetodeprogrammet IMPETUS Afea Solver er brukt til å gjennomføre numeriske simuleringer. Parameterne i den innebygde partikkelmodellen er kalibrert gjennom numeriske simuleringer basert på eksperimenter med en gasskanon. I tillegg ble fallverkseksperimenter gjennomført for å sjekke gyldigheten til partikkelmetoden i flere hastighetsområder. Bortsett fra noen avvik er det generelt sett funnet godt samsvar mellom komponenteksperimentene og de numeriske simuleringene. Samsvaret mellom materialeeksperimentene og de numeriske simuleringene er gode for penetrasjon i høyhastighetsområdet. I simuleringene med tomme og sandfylte paneler ble Johnson-Cook sin konstitutive relasjon valgt for å representere materialegenskapene til alle strukturelle komponenter, mens bruddkriteriet ble valgt til henholdsvis Johnson-Cook for aluminiumspanelet og Cockcroft-Latham for kulas messingkappe og blytupp. De numeriske resultatene ble til slutt sammenlignet med observasjoner fra de ballistiske eksperimentene, noe som viste at IMPETUS Afea Solver er kapabel til å vise hovedtrendene i perforasjonsprosessen.</p> <p>Påvirkningen av valg og verdier bestemt i de numeriske simuleringene er også undersøkt i et eget sensitivitetsstudie. Valgene som er gjort underveis ble funnet til å være fornuftige med tanke på beregningstid for den komplekse modellen som er brukt i dette studiet.</p>
--

FAGLÆRER:	Professor Tore Børvik.
VEILEDERE:	Professor Tore Børvik og Ph.D.-kandidat Jens Kristian Holmen.
UTFØRT VED:	SIMLab, Institutt for konstruksjonsteknikk, NTNU.

MASTER'S THESIS 2015

for

Fredrik Risåsen Bjerke and Lars Magnus Hansen

Experimental and Numerical Study on the Perforation of Empty and Sand-Filled Aluminium Panels

1. INTRODUCTION

Extruded aluminium panels are commonly used in offshore platforms, bridge decks, as components in trains or ships, and in lightweight protective structures. Weight is an imperative factor for all these applications which makes traditional steel and concrete systems impractical. In this study the focus is the protective ability of the panels. Filling them with a granular material such as sand has shown promise in the past, but more experimental data is required. New numerical tools are now available to predict penetration in sand, and validation and testing of these will be a central part of the study.

2. OBJECTIVES

The main objective of the research project is to determine both experimentally and numerically how empty and sand-filled aluminium sandwich panels behave under impact loading.

3. A SHORT DESCRIPTION OF THE RESEARCH PROJECT

The main topics in the research project will be as follows;

1. A literature survey is done to understand the mechanisms of impact dynamics, constitutive modelling of aluminium and sand, and explicit finite element methods.
2. Impact testing is done in the ballistic laboratory at SIMLab to find the ballistic limit velocities of various combinations of aluminium panels and sand types.
3. Material parameters for the sand must be obtained through appropriate component test methods.
4. The material model of the granular material needs to be calibrated against component experiments.
5. The numerical models need to be validated against the experimental results. Simulations of the impact tests are performed by using the IMPETUS Afea Solver and its novel particle-based method. The numerical results have to be compared and discussed with respect to the experimental findings.

Supervisors: Tore Børvik (NTNU) and Jens Kristian Holmen (NTNU)

The thesis must be written according to current requirements and submitted to Department of Structural Engineering, NTNU, no later than June 10th, 2015.

NTNU, January 14th, 2015

Tore Børvik
Professor

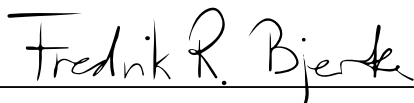
Acknowledgements

This Master's thesis is written in the spring of 2015 in collaboration with the research center, Structural Impact Laboratory (SIMLab). It is the final stage to complete the degree of Master of Science in Civil and Environmental Engineering, with specialization in Computational Mechanics at the Norwegian University of Science and Technology (NTNU).

Our supervisors, Professor Tore Børvik and PhDC Jens Kristian Holmen are greatly acknowledged for their scientific enthusiasm, positiveness and engaging mood. They are also appreciated for guidance and helpful insight in the IMPETUS Afea Solver, arranging of weekly meetings and proofreading.

Thanks also to Technical Engineer Trond Auestad for guiding us through all experiments including; Ballistic experiments on empty and sand-filled aluminium panels, gas-gun tests and drop-tower tests. Furthermore, thanks to Senior Engineer Tore Wisth for supplying necessary experimental equipment and visualization of experimental results like; Production of our sand container, three sabots, providing the ball-bearing ball with a diameter of 10 mm and cutting of the perforated panels. In addition, Dr. Lars Olovsson is acknowledged for giving an introduction to the IMPETUS Afea Solver with its code based input-files and powerful features.

Trondheim, June, 2015



Fredrik Risåsen Bjerke



Lars Magnus Hansen

Abstract

The discrete particle approach has previously proven to give excellent agreement between experiments and numerical analysis for blast loading and penetration in granular medias. The main objective in this thesis is to further investigate the accuracy of the particle-based approach for penetration in granular materials, and compare the numerical output with conducted experiments. A literature survey on penetration in granular media is also carried out to understand the main mechanisms.

Ballistic limit curves and ballistic limit velocities have been identified by experiments performed at SIMLab, NTNU, on empty and sand-filled AA6005-T6 aluminium panels impacted by 7.62 mm APM2 bullets. Three different fractions of granular media have been tested, with a median grain size of 0.15 mm, 0.55 mm and 0.95 mm. The experiments showed minor differences in ballistic limit velocity between each fraction of sand, but an increase of at least 32.5 % is seen when filling the empty panels with granular media tested in this study.

The non-linear explicit finite element software IMPETUS Afea Solver is employed in the numerical work in this thesis. The parameters in the particle model were calibrated through numerical simulations against gas-gun component tests. In addition, drop-tower component tests were carried out, allowing the particle-based method to be validated over multiple velocity domains. The component experiments and numerical simulations are in good agreement for impacts in the high velocity domain. In the numerical simulations for empty and sand-filled panels a standard Johnson-Cook constitutive relation is used for all structural parts, while fracture is modelled with a Johnson-Cook criterion for the aluminium panel and a Cockcroft-Latham criterion for lead tip and brass jacket. The numerical results were finally compared to experimental observations, which showed that IMPETUS Afea Solver is able to capture the main trends in the perforation process.

The influence of various numerical input was also investigated in a rather comprehensive sensitivity study. This showed that the input for the aluminium panel seems reasonable compared to computational cost for the complex model applied in this thesis.

Contents

Acknowledgements	i
Abstract	iii
Contents	vii
Nomenclature	ix
1 Introduction	1
2 Theoretical Background	3
2.1 Ballistics	3
2.2 Impact Dynamics	4
2.2.1 Terminology	4
2.3 Perforation Mechanisms	6
2.4 Ballistic Limit Velocity	7
2.5 The Recht-Ipson Model	8
2.6 Modeling of Material Behaviour	9
2.6.1 Metals	9
2.6.2 Sand	12
2.7 Finite Element Method	12
2.7.1 IMPETUS Afea Solver	13
2.8 State of the Art	14
2.8.1 Penetration in Granular Media	15
2.8.2 Observations at the Meso- and Macro-Scale	17
2.8.3 Effects of Essential Features in Sand Impact	18
2.8.4 Numerical Modelling in Geomechanics	22
3 Target Materials	24
3.1 Aluminium	24
3.2 Granular Media	26
4 Ballistic Experiments: AA6005-T6 Panels	30
4.1 Experimental Work	30
4.2 Experimental Results	33
4.2.1 AA6005-T6 Panels without Sand	35
4.2.2 AA6005-T6 Panels with Sand	38
4.2.3 Cross Sections	42

4.2.4	Ballistic Limit Velocities	44
5	Component Experiments	47
5.1	Compressed Gas-Gun (280 m/s)	47
5.1.1	Set-up Design	47
5.1.2	Experimental Set-up	52
5.1.3	Results	54
5.2	Drop-Tower (2-10 m/s)	56
5.2.1	Data Processing	58
5.2.2	Experimental Results	58
6	Calibration of Material Constants	61
6.1	Aluminium	61
6.2	Bullet Parts	62
6.3	Sand	64
6.3.1	Compressed Gas-Gun: Numerical Investigation	64
6.3.2	Drop-Tower: Numerical Investigation	68
6.3.3	Discussion	72
7	Numerical Simulations	74
7.1	Empty AA6005-T6 Aluminium Panel	74
7.1.1	Numerical Base Model	74
7.1.2	Numerical Results	77
7.2	Sand Filled Aluminium Panel	84
7.2.1	Numerical Base Model	84
7.2.2	Energy Balance Check	85
7.2.3	Numerical Results	85
7.3	Comparisons	88
7.3.1	Numerical Output for Empty and Sand-filled Panels	88
7.3.2	Experimental and Numerical Response	89
8	Sensitivity Studies	92
8.1	Straight Plate	92
8.1.1	Rigid Steel Core versus Full Bullet	93
8.1.2	Element Erosion	94
8.1.3	Mesh Sensitivity	95
8.1.4	Contact Friction Coefficient	95
8.2	Slanting Web	96
8.2.1	Element Orientation	98
8.2.2	Steel Core versus Full Bullet	98
8.2.3	Mesh Sensitivity	99
8.2.4	Bullet Impact Angle to Slanting Web	101
8.3	Sand	101
8.3.1	The Variation in Energy Balance	106
9	Discussion	108
10	Concluding Remarks	111

11 Further Work	114
Bibliography	120
Appendix:	121
A Chemical Components and Sieve Analysis of Granular Media	121
B Water Content Calculations	128
C Sand container	129
D IMPETUS Afea Solver Input Files	131
D.1 Extruded Aluminium Panel With Sand	131
D.2 Circular Sand Box Simulation	135
D.3 Sand Drop-Tower Simulation	138

Nomenclature

χ	Taylor-Quinney coefficient
ΔT	Temperature change
$\Delta \varepsilon_{eq}$	Increment of the equivalent plastic strain
Δt_{cr}	Critical time step
$\dot{\varepsilon}_0$	User-defined reference strain rate
$\dot{\varepsilon}_{eq}$	Plastic strain rate
$\dot{\varepsilon}_{eq}^*$	Dimensionless plastic strain rate
ϕ	Volume fraction of sand.
ϕ	Volume fraction
ρ	Material Density
σ^*	Triaxiality ratio
σ_1	Major principal stress
σ_H	Hydrostatic stress
σ_{eq}	Equivalent stress
v_i	Initial velocity
v_r	Residual velocity
v_{bl}	Ballistic limit velocity
ε_f	Fracture strain
ε_{eq}	Plastic strain
A, B, n	Material constants for Power hardening law
a, p	Recth-Ipson constants/empirical constants
C_c	Coefficient of curvature
c_d	The dilatational wave speed

C_p	Specific heat
C_u	Coefficient of uniformity
D	Damage parameter
D_1 to D_5	Material constants for JC fracture criterion
d_m	Median grain size
d_s	Particle diameter in numerical sand model
E	Young's modulus
g	Gravity of Earth
k_B	Boltzmann constant
k_s	Parameter for soil-soil stiffness in the rheological model of sand implemented in IMPETUS Afea Solver
L_e	Characteristic element length
m_p	Mass of projectile
m_{pl}	Mass of plug
T	Temperature
T^*	Homologous temperature
W	Plastic work per unit volume
W_{cr}	Critical plastic work
APM2	Type of armour piercing bullet
B15	A fraction of sand with median grain size of 0.15 mm
B55	A fraction of sand with median grain size of 0.55 mm
B95	A fraction of sand with median grain size of 0.95 mm
CPU	Central processing unit
DEM	Discrete element methods
FDM	Finite-difference methods
fps	Frames per second.
GPU	Graphics processing unit
h	Hours
HSR	High Strain Rate

ISO	International Organization for Standardization
JC	Johnson-Cook
MJC	Modified Johnson-Cook
PSOIL-card	IMPETUS Afea Solver command for setting up a soil domain and defining soil parameters
w×h×t	Width×Height×Thickness.

Chapter 1

Introduction

During international peacekeeping operations a key factor is to keep the personal safe from possible threats. They will be especially vulnerable in the first phase before a proper camp is installed. Protective structures are typically made of high strength steel due to their proven ballistic performance [1]. To save transportation weight, an idea is to use lightweight extruded aluminium panels and fill them with local granular media to improve their protective properties [2].

Ballistic and blast load experiments have earlier been carried out to check the response to a 20 ft standard ISO container protected by extruded panels filled with four different fractions of granular media with diameters in the range from 0-22 mm. Blast loadings were then numerically analysed with the non-linear finite element code LS-DYNA. However, the ballistic impact experiments on these panels were not investigated in terms of numerical simulations. The protecting system was at that time shown to meet all functional, manufacturing and logistic requirements from the performed full-scale validation tests [2].

New experimental tests to check the capacity of extruded panels filled with granular media of fine sand were done in the ballistic laboratory at SIMLab. Three different fractions in the fine sand range were tested and characterized with rather simple techniques. The penetration tests of sand were performed in different velocity regimes, by both ballistic impact from a compressed gas-gun and mechanical impact from a drop-tower. These types of alternative material tests were carried out with the purpose to give relevant results for calibration of the material model used in the numerical analysis.

Granular medium is difficult to model because of the complicated behavior under dynamic conditions. The nature of sand has therefore been investigated in a literature survey, specially when subjected to projectile penetration.

The novel particle-based method implemented in the explicit non-linear finite element software IMPETUS Afea Solver opens new possibilities to capture important physical behavior of sand during penetration events. This discrete particle approach has previously proven to give excellent agreement between experiments and numerical analysis for blast loading [3, 4] and penetration in granular medias [5]. The method has therefore been

adopted in the numerical work by running calibration simulations in addition to full size impact simulations of the target panel filled with the characterized sand.

The thesis is split into relevant chapters. An overview with a short summary from each of them is given below:

Chapter 2, Theoretical Background: Gives an overview of the most relevant theory used in this thesis. The chapter contains a brief introduction to ballistics, numerical modelling of material behavior and a state of the art on phenomena in granular media undergoing different loads.

Chapter 3, Target Materials: The manufacturing of the AA6005-T6 panel is shortly described. Different parts of the panel are defined and sand fractions are characterized.

Chapter 4, Ballistic Experiments: AA6005-T6 Panels: A review of experimental work performed on the aluminium panel without and in combination with the different sand fractions is presented. Experimental results and ballistic limit curves are presented and discussed.

Chapter 5, Component Experiments: Experimental methods related to the testing of granular media are presented, including the results of these.

Chapter 6, Calibration of Material Constants: Material constants for the aluminium panel and bullet parts are converted from a modified Johnson-Cook model to the standard Johnson-Cook model. Material constants for the rheological model for the sand are calibrated by reproducing the component experiments numerically. A discussion of limitations in this model is also presented.

Chapter 7, Numerical Simulations: Numerical base models for empty and sand-filled panels are created and numerical result presented. In addition the effects of projectile oblique angle in addition to panel plate thickness are investigated.

Chapter 8, Sensitivity Study: A rather comprehensive parameter study is executed on simplified models to validate the numerical results.

Chapter 9, Discussion: The effect of the most important parameters and the use of the discrete particle module in design of protective structures are discussed in this chapter.

Chapter 10, Conclusion: A summary of experimental and numerical results with the conclusive remarks.

Chapter 11, Further Work: Further work in the area of experimental and numerical analysis of penetration in sand are proposed.

Chapter 2

Theoretical Background

In this chapter the theoretical background relevant for this thesis will be presented. To begin with an introduction to ballistics and impact dynamics will be given, including the specific terminology from this subject field. Furthermore the mechanics of materials needed to recreate the behaviour of the materials used during impact, will be explained. It is assumed that the reader is familiar with basic mechanics and physics. Additionally the non-linear finite element method (NFEA) with the used numerical solver is shortly described. Lastly, an overview of previous work concerning material behaviour and penetration in granular media will be presented.

2.1 Ballistics

Ballistics is the science of mechanics that studies the motion, behaviour and effects of free-flying objects with initially forced movement, such as bullets, missiles and rockets [6]. The use of ballistics has intrigued engineers and physicists in all times. Specially the potentiality in use of powerful and effective ranged weapons in military applications, has motivated this field of science through the history [7]. It origins from the oldest known projectiles of stones and spears, to bows and arrows, dating back in ancient times, to catapults, trebuchets and the first gun-like devices in medieval times [6].

The field of ballistics can be further divided into four disciplines; interior ballistics, intermediate ballistics, exterior ballistics, and terminal ballistics [8]. Interior ballistics deals with the interaction between the gun, projectile and propelling charge, in other words the accelerating of the projectile. Intermediate ballistics studies the initial motion of the projectile as it is exiting the muzzle and entering the free flight phase. Exterior ballistics encompasses the projectile in flight from the time it has left the muzzle until impact with the target. Lastly and most focused in this thesis, terminal ballistics, which covers all aspects of events that occur when the projectile reaches the target. Terminal ballistics with the description of the target during impact is of special interest with regards to fortification like structures used for additional strengthening in military defences.

2.2 Impact Dynamics

An impact can be defined as the collision between two or more solid bodies. The interaction can be elastic, plastic, fluid or any combination of these [9]. The impact phenomena can be affected by geometric and material characteristics of the target and projectile, in addition to the strain rate, impact angle and striking velocity involved [10].

The impact velocity will normally be the key factor to decide which physical process that will dominate the impact. The impact velocity can be divided into certain velocity regimes or ranges; *low-velocity domain* (0-25 m/s), *subordnance domain* (25-500 m/s), *nominal ordnance range* (500-1300 m/s), *ultraordnance domain* (1300-3000 m/s) and the *hypervelocity range* (>3000 m/s). The lowest domain at 0-25 m/s is typically seen in free-falling projectiles, and can with the lowest velocities be described in large parts by structural dynamics, with the effect of primarily elastic and maybe some local plasticity at impact. The subordnance and nominal ordnance regimes are achievable with pneumatic or powder guns, with the result of plastic defects and where the viscous material strength still is significant. Beyond these velocity regimes, the impact effect may be described with fluid behaviour where density and compressibility is more important than material strength, or even the effect of explosive vaporization of colliding solids. To reach these velocity regimes, it may be required everything from gas-guns and explosives to meteors and shaped charge jets [11, 10]. It must be said that the described effects do not present a complete picture, since the characterization of the projectile and target element is of large importance. This thesis will focus on the former described velocity regimes.

2.2.1 Terminology

Penetration mechanics is in the literature described using a variety of definitions. In order to keep track of the terminology used in this thesis, some definitions will be disambiguated and presented in the following section. The use of terms are mainly based on the previous work by Backman and Goldsmith [11].

An object striking a target is the principal part of ballistics. This object will often be referred to as the *projectile*, in the meaning that it is a device designed for ballistic performance and with a structure that serves specific ballistic functions. Examples are bullets, bombs, missiles, rockets, artillery shells etc. A part of this object would be the *penetrator* which refers to the part of the projectile that is supposed to have the main terminal ballistic function. The projectile may also contain a *striker*, which refers to an object that is considered to initiate an impact.

The geometry of the projectile nose shape is an important factor for the evolution of a given perforation mechanism, as will be later discussed. Examples of common nose shapes are hemispherical, ogive, blunt, parabolic and conical. Projectile nose shapes used in this thesis are illustrated in Figure 2.1. The ogive nose is most common for small-caliber bullets, while many of the other shapes are employed to investigate penetration characteristics [7].

The penetration which means the process where the object get struck by the penetrator, can roughly be said to have three possible outcomes:

- *Perforation*, which means that the penetrator goes through the *target element*, and maintains residual velocity.
- *Embedment*, which means that the penetrator stopped during contact with the target element.
- *Ricochet*, which means that the penetrator rebounds or get deflected with a change in trajectory in any direction, without either being stopped by the target element or passing through it.

The *target* is further defined as the object that is meant to be impaired by the projectile, with a *target element* which is the section of the target that is directly affected by the impact. This section will often be the component in a model. As an example from this thesis, one single aluminium panel could be identified as the target element, used to strengthen a given target, e.g. a container or any other structure. Since there is no specified protecting target in this thesis, the target will generally refer to the aluminium panels.

The thickness of the target element will have an important role of the penetration process, and can therefore be a convenient way to classify target elements. Backman and Goldsmith came up with the following operational definitions [11]:

- *Semi-infinite*, if the penetration process does not influence the rear surface of the target.
- *Thick*, if the rear surface is influenced by the penetration process, only after substantial travel of the projectile into the target.
- *Intermediate*, if the rear surface exerts considerable influence on the deformation process during the whole penetration.
- *Thin*, if no stress and deformation gradients exist throughout the target elements thickness.

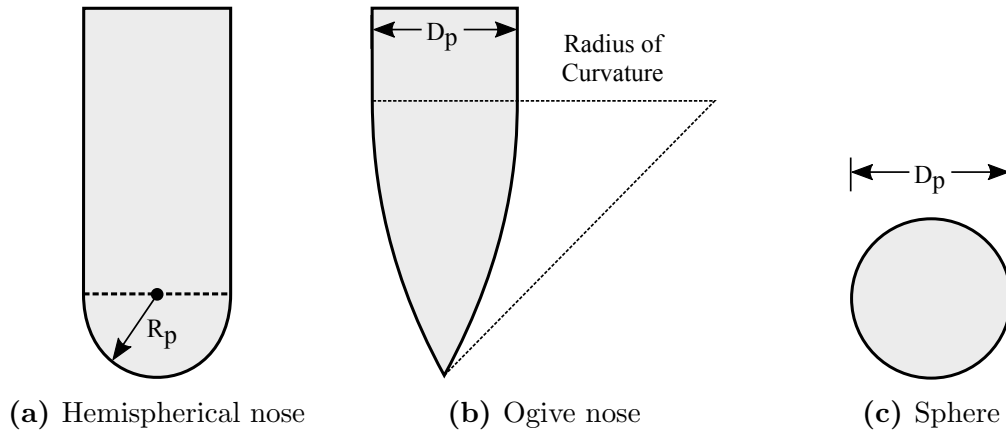


Figure 2.1: Different nose shapes used in this thesis.

2.3 Perforation Mechanisms

A material subjected to impact may fail in a variety of ways, depending on several influencing factors. In addition to the impact velocity, these variables may be material properties, projectile shape, target support, and relative dimensions of projectile and target. The dominant failure modes for thin and intermediate thickness targets are shown in Fig. 2.2. It is important to note that the dominant mode in the failure process often may be accompanied by several other modes.

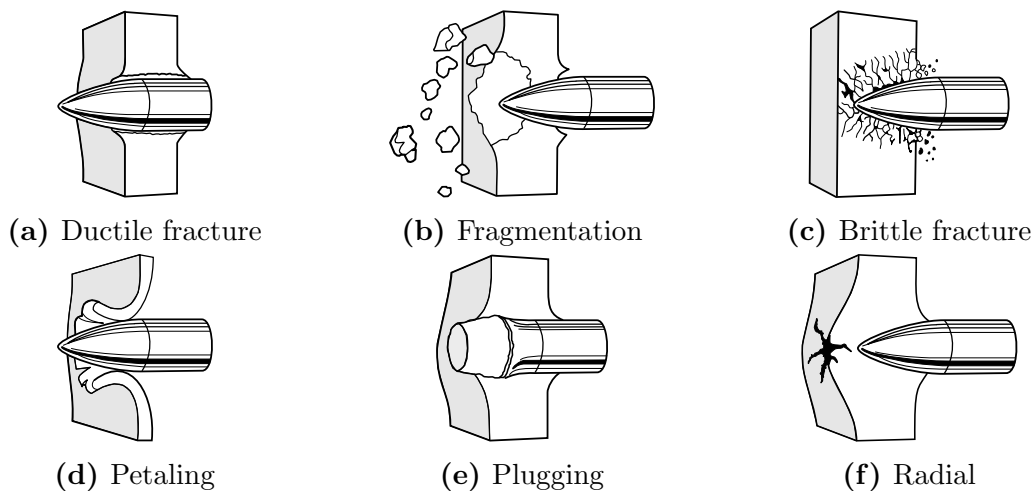


Figure 2.2: Failure modes in impacted plates, redrawn per [11].

A description of each failure mode are presented below [11, 9]:

Ductile hole growth (Fig. 2.2a) occurs when material is pushed away in the radial direction as the projectile perforates the target. This results in an increased size of the penetration hole and a thickened area around the edge of the hole. Often initiated by conical or ogival projectiles.

Fragmentation (Fig. 2.2b) is typical in thin or brittle materials subjected to high impact velocities.

Brittle fracture (Fig.2.2c) is a result of crack initiation and propagation perpendicular to impact direction in brittle materials during impact, such as seen in glass material impacts.

Petaling (Fig. 2.2d) is a failure mode caused by high radial and circumferential tensile stresses near the tip of the projectile, after passage of the initial stress wave. The bending moments created from the motion of the plate being pushed forward by the projectile is the origin to the characteristic deformation pattern. The star-shaped crack is created when the tensile strength of the plate material is reached. Thin plates struck by ogival or conical bullets at low impact velocities, or blunt projectiles close the the ballistic limit are prone to this failure mode.

Plugging failure (Fig. 2.2e) is normally caused by so called "adiabatic shear banding". The mechanism is driven by the work of plastic deformation, which is converted almost entirely into heat. The high deformation rates prevents this heat from propagating a significant distance away from the plastic zone, resulting in rising temperature and further local plastic flow and straining. This process continues and results in the propagation of a narrow band of intense plastic strain through the material until unloading or fracture occurs. The failure mode is normally caused by blunt or hemispherical-nosed projectiles on intermediate to thin target plates with an impact velocity close to the ballistic limit.

Radial cracking (Fig. 2.2f) is common in materials where the tensile strength is considerably lower than the compressive strength, such as ceramics. It is generated by the compressive wave that propagates away from the impact point in the target, building up large circumferential tensile stress waves. When the tensile strength is exceeded, radial cracks may occur.

2.4 Ballistic Limit Velocity

The *ballistic limit velocity*, v_{bl} , is the greatest impact velocity a given target can withstand without being perforated by a given projectile [8]. This limit is typically found in experiments by shooting a few projectiles that achieve complete penetration, and measuring the residual velocity through the use of x-rays or high-speed cameras. There are several definitions of the ballistic limit, like the army, protection, and navy ballistic limit listed by Backman and Goldsmith [11]. The different definitions depend on which requirements wanted for a perforation, like if the projectile only breaches the target before embedment or maintains residual velocity. The ballistic limit velocity is based on the navy definition in this thesis, where the definition of perforation requires residual velocity of the projectile.

With the initial and residual velocity data, the ballistic limit velocity can be described by generating a curve, as shown in Figure 2.3. There are several factors affecting the ballistic limit velocity, like material hardness, yaw at impact, projectile density, projectile nose shape, measurement errors, etc. It is therefore important to note that this is a

statistical representation of the ballistic limit for a given projectile, impact direction and target, such that the curve is showing the trend.

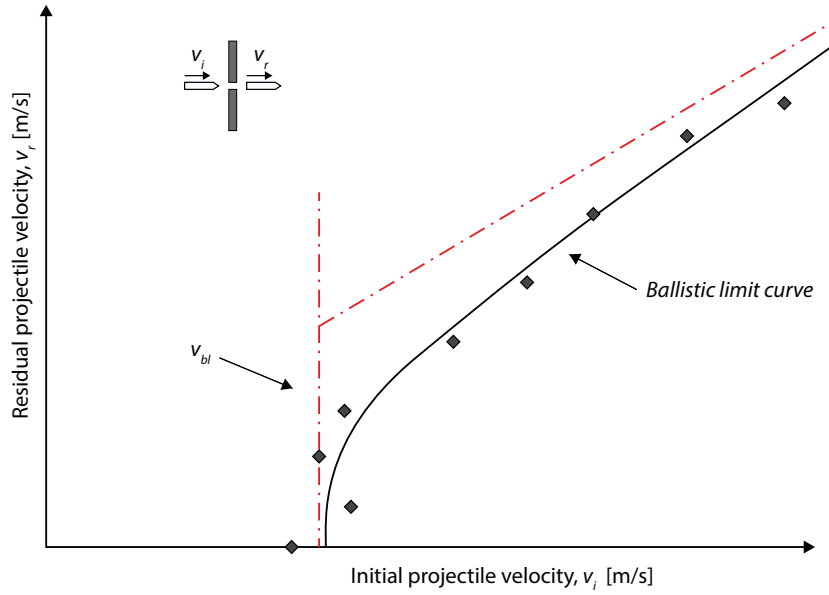


Figure 2.3: Illustration of a ballistic limit curve.

2.5 The Recht-Ipson Model

Recht and Ipson proposed in 1963 analytical equations relating the ballistic limit velocity and ballistic curve for relatively thin plates. Both blunt and sharp-nosed projectiles were considered. They utilized conservation of momentum and energy, in order to find an equation that is valid for blunt projectiles impacting a thin plate [12]:

$$v_r = a(v_i^p - v_{bl}^p)^{1/p}, \quad a = \frac{m_p}{m_p + m_{pl}}, \quad p = 2 \quad (2.1)$$

where m_p is the projectile mass, m_{pl} is the plate plug mass, v_r is the residual projectile velocity, v_i is the initial projectile velocity, v_{bl} is the ballistic limit velocity. For sharp nosed projectiles the major failure process becomes ductile hole growth with no plug ejected, reducing a to $a = 1$.

Lambert and Jonas [13] generalized Eq. 2.1 by using a , p , and v_{bl} as empirical constants. This generalization will be used in this thesis to establish ballistic limit velocities and trend lines through experimental data.

2.6 Modeling of Material Behaviour

The mechanics of materials used in this thesis will be briefly presented in the following. A more comprehensive description of the equations and the theory behind them can be found in the literature [14, 15].

2.6.1 Metals

Constitutive Relations and Failure Criteria

A material model is used to describe the relation between stress and strain for a given material with a so-called constitutive relation. A classic and simple example of this is the Hooke's law that applies for an elastic material with a linear relationship between stress and strain. The mechanical response of structures exposed to impact loading requires more advanced constitutive descriptions of the material's stress-strain relationship. A complete model that considers large strains, high strain rates, temperature softening, varying stress states, loading history and strain- or work hardening behaviour is difficult to obtain, so it is necessary to introduce assumptions according to the need of the application [16].

The constitutive relation is often expressed in terms of the equivalent stress σ_{eq} , defined in terms of accumulated plastic strain ε_{eq} , plastic strain rate $\dot{\varepsilon}_{eq}$ and temperature T [17].

$$\sigma_{eq} = f(\varepsilon_{eq}, \dot{\varepsilon}_{eq}, T) \quad (2.2)$$

In addition to the constitutive relation a fracture criterion is necessary to complete the material model, such that the model is able to deal with damage and failure. Damage evolution is usually described by a damage parameter. Failure takes place when the damage parameter reaches a predefined value.

Rheological Model

Rheological models are often used to give a convenient representation of the material behaviour with elements like springs, dashpots and frictional elements connected in series or in parallel. The specific use of aluminium plates combined with ballistic penetration gives rise to a thermoelastic-thermoviscoplastic model with an elastic spring, non-linear dashpot and frictional element (Fig.2.4). When work-hardening is present, the strength is increasing.

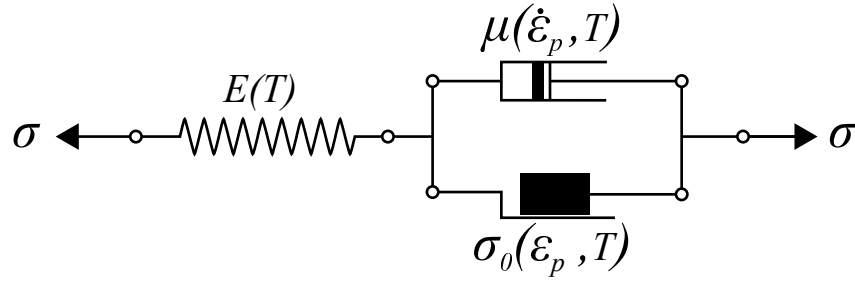


Figure 2.4: Thermoelastic-thermoviscoplastic rheological model, redrawn per [18].

Johnson-Cook Material Model

The material model used in this thesis is based on a multiplicative constitutive relation where the strain hardening, strain-rate hardening and temperature softening are independent of each other. This means that the parameters may be calibrated independently of each other. This phenomenological model which is based on empirical values was proposed by Johnson and Cook [19]. The equivalent von Mises stress is expressed as:

$$\sigma_{eq} = [A + B \varepsilon_{eq}^n][1 + C \ln \dot{\varepsilon}_{eq}^*][1 - T^{*m}] \quad (2.3)$$

A , B , C , n and m are five material constants related to strain hardening, strain rate hardening and temperature softening. ε_{eq} is the equivalent plastic strain, while $\dot{\varepsilon}_{eq}^* = \dot{\varepsilon}_{eq}/\dot{\varepsilon}_0$ is the dimensionless plastic strain rate, where $\dot{\varepsilon}_0$ is a user-defined reference strain rate. The homologous temperature is defined as $T^* = (T - T_r)/(T_m - T_r)$, where T is the current material temperature, and the suffixes r and m indicate the room temperature and the material's melting temperature, respectively.

The model calculates the temperature change caused by dissipation of plastic work due to adiabatic heating as

$$\Delta T = \int_0^{\varepsilon_{eq}} \chi \frac{\sigma_{eq} d\varepsilon_{eq}}{\rho C_p} \quad (2.4)$$

where ρ is the material density, C_p is the specific heat and χ is the Taylor-Quinney coefficient that represents the proportion of plastic work converted into heat.

In order to avoid unwanted effects when the plastic strain-rate $\dot{\varepsilon}_{eq}^*$ becomes smaller than 1, a modified version of the Johnson Cook without the logarithmic term in the strain-rate sensitivity bracket was put out by Børvik et al. [20] with inspiration from Camacho and Ortiz [21].

$$\sigma_{eq} = [A + B \varepsilon_{eq}^n][1 + \dot{\varepsilon}_{eq}^*]^C[1 - T^{*m}] \quad (2.5)$$

The Cockcroft-Latham Fracture Criterion

Cockcroft and Latham proposed a fracture criterion in 1968 [22]. This fracture criterion assumes failure to occur when the integral of the maximum principle tensile stress along the plastic strain path reaches a critical value. Expressed in relation to the damage parameter it means that the material fails once the damage parameter has evolved from 0 to 1. The damage parameter is given as

$$D = \frac{W}{W_{cr}} \leq 1, \quad W = \int_0^{\varepsilon_f} \langle \sigma_1 \rangle d\varepsilon_{eq} \quad (2.6)$$

where W is the plastic work per unit volume with respect to the equivalent stress, ε_f is the equivalent plastic strain at fracture, ε_{eq} is the equivalent plastic strain and σ_1 is the major principal stress. The value $\langle \sigma_1 \rangle = 0$ if $\sigma_1 < 0$, and $\langle \sigma_1 \rangle = \sigma_1$ if $\sigma_1 \geq 0$, indicating that damage will not grow, and fracture can not occur with compressive stress state. The critical value of the plastic work per unit volume W_{cr} can be determined from one simple uniaxial tensile test [1].

The Johnson-Cook Fracture Criterion

Johnson and Cook [23] also presented a fracture criterion that accounts for strain path, strain rate, temperature and stress triaxiality. The damage parameter D of a material element is expressed as

$$D = \sum \frac{\Delta\varepsilon_{eq}}{\varepsilon_f} \quad (2.7)$$

where failure is assumed to occur when $D \geq 1$.

$\Delta\varepsilon_{eq}$ is the increment of the equivalent plastic strain that occurs during an integration cycle. ε_f is the actual value of the fracture strain, which is defined as

$$\varepsilon_f = (D_1 + D_2 \exp(D_3\sigma^*)) (1 + D_4 \ln \dot{\varepsilon}_{eq}^*) (1 + D_5 T^*) \quad (2.8)$$

where D_1 to D_5 are material constants. σ^* is the stress triaxiality ratio defined as σ_H/σ_{eq} , where σ_H is the hydrostatic stress. As in the constitutive model the various phenomena are taken into account uncoupled from each other.

A modified version of the Johnson-Cook fracture strain model can be found by applying the modified expression for the strain-rate sensitivity again [20].

$$\varepsilon_f = (D_1 + D_2 \exp(D_3\sigma^*)) (1 + \dot{\varepsilon}_{eq}^{D_4}) (1 + D_5 T^*) \quad (2.9)$$

2.6.2 Sand

The sand grains are modelled using a rheological model with a penalty based contact formulation. The model includes the mass of the particles (m_p), two linear springs acting in the normal (k_n) and the tangential direction (k_s) and a linear dashpot with a damping coefficient, c . In addition the tangential spring force is limited by a Coulomb friction coefficient, μ . This model was proposed by Deshpande et al. [15] to better understand dynamic soil-structure interactions in landmine explosions, and is shown in Figure 2.5. The normal and tangential contact forces become:

$$F_n = k_n \delta_n + c \dot{\delta}_n \quad (2.10)$$

and

$$F_s = \begin{cases} -k_s \delta_s & \text{if } |F_s| < |\mu F_n|, \\ -\mu |F_n| \text{sign}(\delta_s) & \text{otherwise} \end{cases} \quad (2.11)$$

where δ_n and δ_s are the relative displacements in the normal and tangential directions. Note that the direction of the tangential force is dependent of the direction of relative motion.

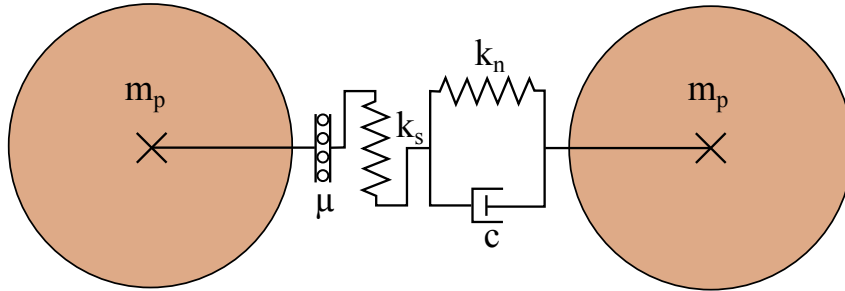


Figure 2.5: Rheological model for interaction between sand particles.

2.7 Finite Element Method

The finite element method is a numerical technique to establish approximate solutions for partial differential equations [24]. An explicit time integration is best suited for impact and wave propagation problems where small time steps are necessary [24]. One disadvantage with the explicit time integration is that it is conditionally stable. This means that the calculation "blows up" unless the time step is below a critical time step. Assuming no damping the equations become:

$$\Delta t_{cr} = \frac{L_e}{c_d}, \quad c_d = \sqrt{\frac{E}{\rho}} \quad (2.12)$$

where Δt_{cr} is the critical time step, L_e is characteristic element length, c_d is the dilatational wave speed in the material, E is Young's modulus and ρ is the material density.

In an explicit method numerical instability is difficult to detect because energy can be artificially dissipated. An important task is therefore to perform an energy balance check to warn of numerical instability. In this thesis a deviation of less than 5 % in the energy balance are assumed acceptable. For a thorough review of the finite element method the reader is referred to Cook et al. [24].

2.7.1 IMPETUS Afea Solver

In this thesis IMPETUS Afea Solver is used, which is a general non-linear finite element software specially created for prediction of structural behaviour under extreme loading and large deformations [25]. The software consists of different modules, including the Finite Element (FE) module and Discrete Particle (DP) module used in this thesis. The solver utilizes the computational force of the graphics processing unit (GPU), which can speed up the numerical simulations significantly [25]. Furthermore, the solver is purely Lagrangian with a node-to-surface penalty based contact algorithm. Figure 2.6 shows the robust higher order 64-node element implemented in IMPETUS Afea Solver, which is used to model the impact zones undergoing large deformations and high strain rates in this thesis.

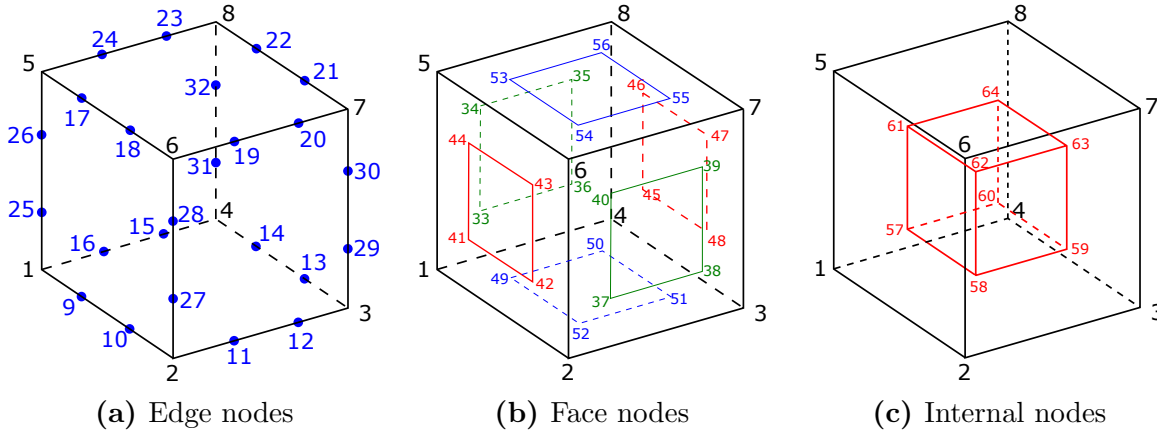


Figure 2.6: 64-node cubic hexahedron element in IMPETUS Afea Solver[26].

Discrete Particle Module

The discrete particle module implemented in IMPETUS Afea Solver uses the rheological model described in Section 2.6.2, with the simplifications that $k_n = k_s = k$ and only translational degrees of freedom are included. The last simplification will highly increase the critical time step needed in the model, which reduces the computational cost. This is described in Børvik et al. [3] and they argue that as long the aggregate behaviour can be tuned by the soil parameters, i.e stiffness, damping, friction and initial packing, this simplification is acceptable for high rate deformations. The model is based on rigid

mono-sized spherical particles that interact through contact and elastic collisions. The method is based on a Lagrangian formulation and has several advantages over Lagrangian-Eulerian approaches. Both advection errors and severe contact problems are avoided with this formulation [3].

The primary focus in this thesis is to capture the projectile trajectory and deceleration when impacting the target consisting of an extruded aluminium panel filled with granular media. The simple model is phenomenological, so one can not expect to capture the micromechanics in the sand [5]. As of now the model does not include phenomena like fracture of individual grains, strain rate sensitivity and the mentioned rotational degrees of freedom of the particles.

2.8 State of the Art

In this section previous work of penetration in granular media is presented, with the main inspiration from Omidvar et al. [27, 7]. Firstly the properties of granular materials will be discussed, before the different response to penetration are considered. Lastly a short summary of the development of numerical modelling in geomechanics is presented.

Granular materials are basically large conglomerations of discrete macroscopic particles. In noncohesive soils like sand and gravel, the forces between the particles are only repulsive, meaning that external boundaries and gravity will determine the shape of the material [28]. Granular materials can be studied at a number of interrelated scales. The *macro scale* or continuum scale where the physical phenomena of a volume with granular material is described, is the most important for practical engineering purposes, even though this scale is influenced by physical phenomena at underlying scales, like the *micro scale*, where properties of individual soil particles, like crystalline anisotropy, shape and texture, and inter-granular kinetics and kinematics such as rotation, translation and crushing are studied. An overlapping scale between these two can be referred to as the *meso-scale*, where collective behaviour of rearrangement, dilation, strain localization, and force chains take place [7]. In this scale the number of grains can easily be recognized and counted by eye.

Jaeger and Nagel [28] have examined some of the particular properties of granular materials that appear under different conditions. In dry sand, many of the flow and static properties of the system can be determined by neglecting the interstitial fluid, e.g. air. Even though it seems simple, a granular material cannot be entirely compared to any familiar forms of matter, like solids, liquids or gases. Therefore it needs to be considered as a state of matter in its own rights. A sand pile at rest behaves like a solid, but if the pile is tilted several degrees above the angle of repose, the grains at the boundary layer of the pile will behave as a flowing fluid. There are especially three important aspects that contribute to the unique properties of granular materials: Firstly, the ordinary temperature plays no role. Granular flow is very similar to flow in dense gases, thinking that both consist of discrete particles with negligible cohesive forces between them. The energy scale in gases, $k_B T$, which is the product of the Boltzmann constant (k_B)

and the temperature (T) is shown to be insignificant related to granular materials. This is because the relevant energy scale, the potential energy mgd of a grain with mass m , and a diameter d in the earth's gravity g , is at least 10^{12} times $k_B T$ for a typical sand in room temperature. Therefore ordinary thermodynamic arguments become useless in granular materials. Since $k_B T \approx 0$, it implies that entropy considerations is outweighed by dynamical effects, and that no exploration of phase space will take place, which is normally an important feature of temperature. The temperature in ordinary gases or liquids will also provide a microscopic velocity range, which is completely suppressed in granular materials, where the velocity scale is imposed by any microscopic flow itself. The second unique property of granular materials is the dissipative interactions between grains because of static friction and the inelasticity of collisions [28].

Another noticeable behaviour of sand is the lack of height-dependent pressure head, like we find in normal fluids. If granular material is filled in a tall cylindrical container, the pressure at the base of the container does not increase indefinitely as the height of the material inside it is increased. The static friction with the sides of the container conducts the container walls to support the extra weight, like in an hour glass, so the maximum pressure value is reached independent of the height [28].

2.8.1 Penetration in Granular Media

Terminal ballistics in granular media requires insight in both penetration mechanisms and geomechanics, adopting ideas and language from both fields.

The study of impact and travel of projectiles in granular media can be traced back to 1742 [29] with the Robin-Euler penetration depth formula [5]. In the past century the motivation of the research field has spread from mainly military interest into use in civilian applications. This includes among other things, subsurface investigation of soil and rock at special locations, planetary impact, installation of deep sea anchors and foundations, nuclear waste disposal, mining, and aircraft landing studies [7].

It is earlier shown that the volume fraction ϕ of the granular media has a huge influence on the dynamics of impact. This is most likely due to changes in flow and the influence of boundaries from compaction and dilation. Among the findings, it is seen that an increased ϕ , leads to exertion of increasingly larger forces on the sidewalls from the grains, and presumably also on the intruder. This occurrence at shallower depths causes to ultimately reduce the gravitational forces on the grains [30]. The volume fraction or the so called packing state or compaction of granular media will often be referred to as loose and dense sand, being the outer points in the relevant volume fraction scale.

Penetration Phases in Granular Material

The penetration into a granular material can often be separated into distinct phases. The first phase is the transient phase, which involves the initial impact and a shallow penetration. This phase is characterized by a transient interaction between projectile and granular material, forming a crater. The second phase is often considered to be the quasi-steady-state, where the force on the penetrator changes relatively slowly with time. This state lasts until the near end of the penetration, where new transient effects associated with the stopping of the projectile are introduced. This includes transition from dynamic to static friction, inertia effects due to sand particle motion, and the elastic rebound of the sand. Projectile penetration in granular media is often dominated by one of the phases. Transient penetration is typically the subject of earth and planetary sciences, where the size ratio of projectile to target is huge. A deep penetration where the terminal penetration phase dominates, is suggested to have penetration depth of approximately 1-3 projectile diameters plus the nose length [7].

Energy Transfer from Projectile to Granular Media

Impact of a projectile in granular media will generate stress waves that propagate through the granular media as well as the projectile. These stress waves are attenuated both by dispersing over the geometry and by depositing energy into granular media. The ability to dissipate energy in granular media is related to the penetration resistance. The dissipation of the kinetic energy at the projectile is at first caused by initiation of particle motion and stress waves in the granular media, leading to frictional and collisional dissipation as the projectile overcomes resisting forces from the particles. The physical phenomena of the energy transfer in granular media are rather dependent of the velocity regime and the associated strain rates imposed. An impact in the ultraordnance domain of velocity would produce a high-pressure shock wave, causing densification due to void collapse, comminution, and possibly also phase changes in the crystal lattice of the particles. At high enough pressures this densification would be accompanied by heat dissipation and melting of individual grains. Most of these phenomena would be missing in the subordnance domain, causing little change in the grain geometry.

The dissipation process in deep penetration of a granular medium is often driven by considerable compression and shear. The shear deformation of sand is a highly dissipative phenomenon, where the energy absorption is lead by friction and volume change as grains slide, roll and climb over one another. The friction between grains is elevated by the high mean stress which exist in front of a penetrating projectile. The volume change caused by shear leads to pressure-volume work and energy dissipation. The high stresses from the pressure can locally result in fracture of grains, and even complete comminution. The fracture of grains is an additional source to energy dissipation, because of the subsequent creation of new surface area [7].

2.8.2 Observations at the Meso- and Macro-Scale

Observations at the meso-scale of penetration in dry sand have been studied using X-Ray radiography and synthetic transparent soils produced by refractive index matching. Both methods use digital image cross-correlation (DIC) to obtain deformation fields within a plane inside the soil target during penetration [31].

Omidvar et al. [7] has presented some observations and ideas from the literature which tries to explain soil-projectile interactions. Its important to note that they may not be universal for all situations and that further study is required to assess validity of the mechanisms.

Observations during Penetration

The transient stage of penetration is characterized by significant energy loss and elevated resistance to penetration. Studies suggest that this energy decay may result from the formation of a compaction front with a body of sand set in motion ahead of the projectile [32]. The compaction front, acting like a bow shock, travels ahead of the projectile and compacts the particles into a denser arrangement. At high enough impact velocity a second wave will further load the contact of these particles and initiate particle crushing. Significant amount of energy and momentum is transferred to the sand grains and the formation of a cavity behind the penetrating projectile may occur. Soil grains directly in front of the projectile moves in line with the projectile while grains several projectile diameters ahead, moves normal to penetration direction. The lateral soil movement along the projectile afterbody diminishes when the projectile tip passes a give point [7].

Deceleration of Projectile

A rapid deceleration of the projectile is observed upon impact, which is related to the translation of resisting forces from sand to projectile. Observations show that the initial deceleration peak diminishes as the impact velocity decreases. A gradual increase in deceleration by a broad peak is instead observed at very low velocities. The initial peak deceleration is then followed by oscillating deceleration and with a relatively sustained magnitude. Regions with stronger and weaker soil layers may be identified here. Towards the end of penetration there is a sudden rise and fall in resistance to penetration, as seen in Figure 2.7. This phenomenon is applicable to both very low and higher velocity regimes, and has been attributed to the quasi-elastic rebound of soil. This peak may be used to estimate elastic soil properties. It is suggested that this peak is related to the transition from inertial resistance regime to one of quasi static frictional resistance. It is further found that the pressure in front of the projectile is proportional to the velocity squared [7].

A soil needs a long distance over which the force acts in order to have a specified amount of energy dissipated, contra other materials. This is seen as the area under the curves in Figure 2.7.

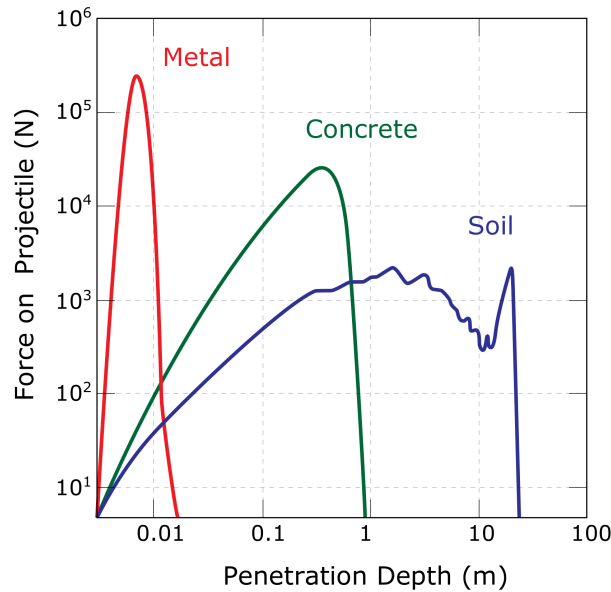


Figure 2.7: Typical resistance behaviour of metals, concrete and sand subjected to projectile penetration (Redrawn per Backman [33]).

2.8.3 Effects of Essential Features in Sand Impact

Particle Crushing

It has been shown that the number of contact points between sand grains is important for the crushing effect. A sand in loose condition will have considerable fewer contact points between individual grains, thereby having more concentrated contact stresses, which again favors particle crushing. Crushing will therefore begin at a smaller overall stress in loose conditioned sand than in dense [34]. Also the surface shape of the sand grains is found to have an effect on crushing, where more angular grains will have more stress concentrations than rounded and sub-rounded grains, thus more prone to crushing [35]. There is a general agreement that crushing of particles decreases both in uniaxial and triaxial compression with increased rate of loading. The reason for this could be that crushing is a time consuming phenomenon requiring accumulation of strain energy and propagation of micro-cracks, according to Omidvar et al. [27]. In projectile penetration into granular media, studies have shown that a threshold velocity of about 70-100 m/s marks a reduction of the resistance mechanism as the projectile slows down. At this threshold also the particle crushing gets significantly reduced [7]. These various observations of particle crushing would need further evaluation at the meso- and micro-scale to employ better understanding in the problem.

Projectile Instability

The penetration depth is in many cases limited by the projectile trajectory and stability. In an oblique impact curved trajectories are very likely to occur during penetration of the target. In normal impact there may be introduced certain lateral disturbances because of small oblique angle or angular velocity, which may cause instability problems [36]. The resisting forces introduced along the projectile's length in the penetration of granular materials, may be asymmetric because of the anisotropic and inhomogeneous nature of granular media. If the center of pressure is located ahead of the center of gravity, any deviation of the center of pressure will produce a torque. When the projectile develops a small oblique angle, the stresses will be higher on one side, which can result in a curved trajectory [7].

Omidvar et. al [7] have summed up some phenomena which may initiate projectile instability:

- Asymmetric loading of the projectile during penetration due to soil material variations or an oblique impact.
- Presence of larger individual grains in a rather uniform granular media.
- Failure and disintegration of projectile in high velocity impacts.
- Increased frictional interactions in the granular media.

Instability may also be favored by increase in impact velocity, increase in porosity, increases in grain size and uniformity of grains size distribution within the soil sample.

Saturation

The experimental testing conducted in this thesis is done with almost completely dry sand, so the main focus is nearly exclusively on dry granular material. Despite this, there is no doubt that most granular materials in natural environment, do have a level of saturation or are exposed for this at some time. Since there are some differences in the behaviour of dry and wet sand, the most important ones will be reviewed.

Horn and Deere [37] reported that quartz sand saturated with a highly polar fluid like water, will experience that the dynamic friction is appreciably less than static friction. But when surface moisture increases the frictional resistance that can be developed between surfaces of quartz sand increases. B.E Martin [38] found contrary that small amounts of water or saturation will lubricate the sand particles, thus reducing the friction and offering less resistance to compression. More water and a higher degree of saturation will lead to a point where the air-filled voids are nearly fully displaced by water, thus making it harder for sand particles to displace into interstitial gaps. With higher saturation degrees from this point, the sand will gradually behave stiffer. The effect observed from Split Hopkinson Pressure Bar tests is illustrated in Figure 2.8.

Several experiments of projectile penetration have shown a decrease in penetration resistance of saturated sand. In Børvik et al. [5] the penetration depth was actually found more than twice in wet sand than in dry sand when penetrated by 7.62 mm Ball and 12.7 mm AP bullets. The reasons for this behaviour under saturated conditions may be a combination of reduced friction between sand grains, partial liquefaction and increased pore pressure [7].

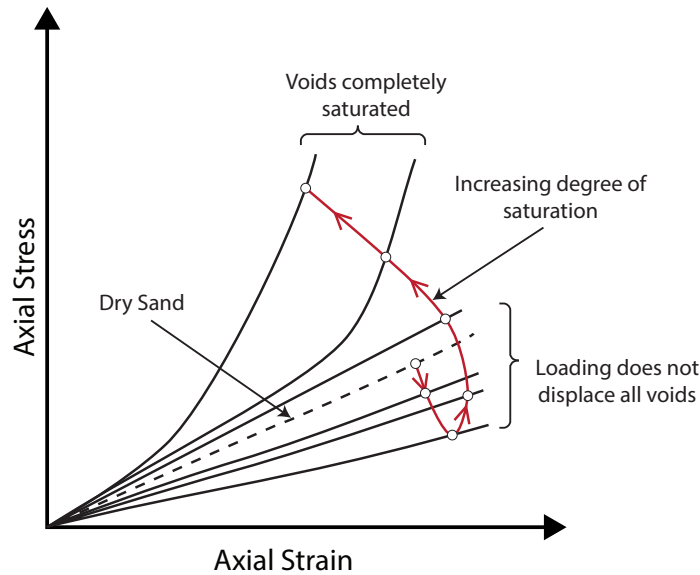


Figure 2.8: High strain rate loading by Split Hopkinson Pressure Bar tests on partially saturated sand (Redrawn per Omidvar et al. [27]).

Strain Rate Effects and Sensitivity in Sand

In testing of sand there is a conceptual difference between a static test and a high strain rate (HSR) test. In a slow test, the sand will have enough time to form shear bands and rearrange itself as stress is measured, while in an HSR test, the sand is flowing during the experiment and has not ceased to flow by the time measurements are made.

High strain rate testing of sand is typically done in four different ways; uniaxial compression tests, also referred to as confined compression or oedometer tests, Split Hopkinson Pressure Bar, triaxial compression and direct shear tests, and plane wave shock tests.

According to Omidvar et al. [27], there are three main mechanisms governing response of sand exposed to quasi-static uniaxial compression:

- Elastic compression of individual sand grains
- Slippage and rearrangement of grains
- Grain crushing

These mechanisms occur at different stress levels, so it is convenient to differentiate the response into four distinct zones. The main mechanisms from the response are also tried illustrated in Figure 2.9.

1. *The first zone:* The initial stress-strain response is characterized by elastic deformation of individual sand grains, since the axial stress level applied is not high enough to overcome the kinetic friction between the grains.
2. *The second zone:* As the applied stress is increasing, the static friction between the sand grains will be exceeded at one point. The "skeleton" of the sand will then be deformed since sand grains are sliding and rolling into available voids. This results in both shear deformation and compaction.
3. *The third zone:* The rearrangement of the sand grains into the voids results in a denser arrangement, thereby increasing contact points between the soil grains. A hardening response will occur in this phase as the particles "lock-up" into a denser arrangement.
4. *The fourth zone:* Individual grains will begin to crush when the stress level gets high enough, allowing further contraction of the "skeleton", and less resistance to compression. This sort of yielding behaviour continues as smaller particles are being fractured and the cycle continues.

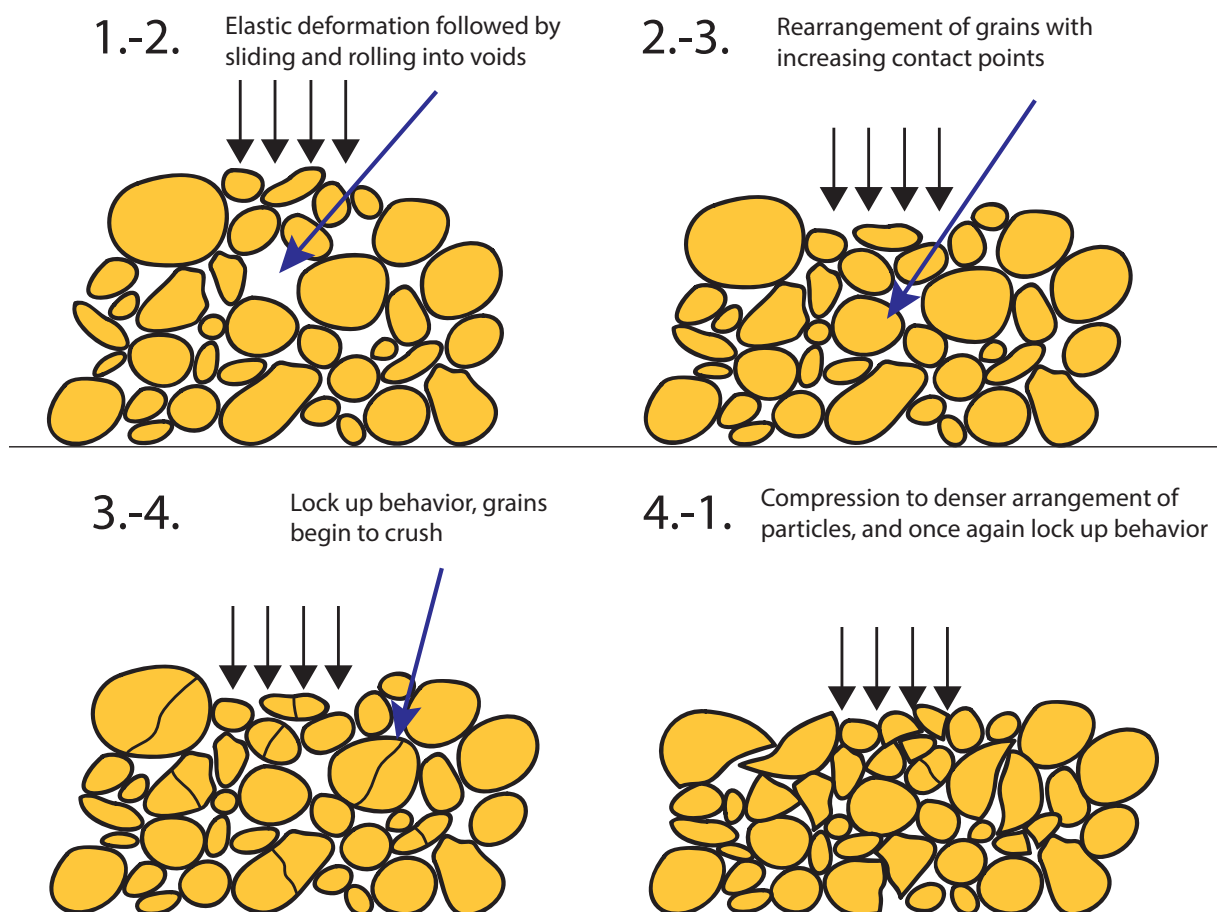


Figure 2.9: Illustration of sand grains exposed to uniaxial quasi-static load.

As stated, the mechanical response of sand at HSR will exhibit different response than under quasi-static loading. Under HSR loading, the sand particles will move and flow during the test until energy is dissipated. This leads to some new observations:

- Inertia forces will oppose the loading stress and promote stress wave propagation due to difference in stresses in front of, and behind the stress wave. The stress wave propagation occurs from one end of the sample to the other. The many propagations will superimpose over one another and lead to stress uniformity.
- A rapid particle rearrangement is observed.
- The particle crushing can also be observed when grain resistance is reached. Unlike quasi-static loading, a cyclic condition with particle crushing and rearrangement is not likely to happen because of the transient loads.

There are thus two main effects that distinguish HSR tests from quasi-static tests. The first occurs when strain rate increases, causing an increase in stiffness to occur in the sample. The second is the development of viscous flow because of stress level and strain rate [39]. It is reported that the strength of sand under HSR loading depends on the stress conditions within the testing method employed [27]. Overall, there are many aspects of the HSR response which need more research.

2.8.4 Numerical Modelling in Geomechanics

Mathematical descriptions of penetration into granular media have been developed empirical, analytical and in terms of phenomenological models. Phenomenological models are describing the nature with simple theories, commonly based on Newton's second law of motion like the earlier mentioned Robin-Euler penetration depth formula [29]. Empirical relationships are typically based on experimental data like the Young's equations for predicting penetration depth formulated through a product of several functions [40]. Analytical predictions are formulated in pure mathematical way like the cavity expansion described by Forrestal and Luk [41]. Issues that are difficult to address with analytical methods, like the role of friction, distribution of resisting forces, soil-projectile interactions during penetration, deformation and erosion of material may be better implemented numerical. Numerical models have therefore increasingly been employed in analysis of projectile penetration in soils, as they also can facilitate solutions of analytical derivations, and with more advanced constitutive models [7].

The numerical methods relevant to penetration of granular materials may be divided into continuum-scale and discrete methods. Continuum-scale methods solve the penetration by discretizing the continuum into a mesh of elements. Finite-element methods (FEM) or finite-difference methods (FDM) are commonly used continuum approaches for finding solutions to the response of soil and rock in the same manner as to many other structural problems. These methods assume that the material is a continuum, which gives some drawbacks when describing granular materials. Firstly the stress-strain relation for the

material may not exist, or be in a state which gives excessively complicated relations with many obscure parameters. Secondly, the natural development of cracks and rupture surfaces is not sufficiently handled by continuum approaches [42]. Therefore there has been a large interest in developing reasonable discrete element methods (DEM), where the granular media is treated as an assemblage of discrete interacting particles. DEM arrange the load transfer between particles by interaction laws, so no constitutive relationship for the bulk material is required [7].

There are several approaches to both continuum and discrete based studies of penetration into granular materials. The first continuum-based FEM for rock mechanics was proposed by Zienkiewicz and Cheung in 1967. In 1971 the representation of rock masses was initiated with DEM by P.A. Cundall [43]. Combining the continuum method and the discrete method is a more recent approach, where the structural elements are modelled using FEM and the granular media are modelled by employing DEM. There are still limitations to these approaches, like the ability to account for particle crushing, energy dissipation and phenomena at the meso-scale, in addition to high computational cost for a complex problem.

Since the knowledge of contact forces between particles is still not perfect, and the computational cost is prohibitive to a large problem, it is often impractical to utilize discrete models at the grain scale. E.g. in field-scale problems like natural hazards, such as landslides, rock avalanches, and for important industrial applications, such as powder handling, granulates in pharmacy etc, continuum description of granular materials is still of great importance for modeling [44]. There have been several attempts to bridge the solid and fluid-like behavioural regimes of granular media into a continuum description, among others by Andrade et al. [44].

Modeling with discrete particles is a method in development, which opens new avenues for dealing with particle crushing and other micro-scale parameters in penetration. Regarding the computational cost, Cundall [42] predicted a model size of 10 million particles to be a easy problem, and 100 million particles to be a hard problem to solve in the year of 2010. In 2020 he predicted corresponding 10 000 million and 100 000 million, in contrast to 10 000 and 100 000, which was the reality at the time of year 2000 [42]. These estimates were probably a bit too high, but also gives a comparison to the development so far and the future potentiality of the method.

Chapter 3

Target Materials

3.1 Aluminium

This study investigates the ballistic properties of aluminium panels extruded from aluminium alloy AA6005. After extrusion the panel was heat treated to a temper T6 to improve its mechanical properties. Temper T6 means that the solution is heat treated and then artificially aged, but not cold worked to increase additional strength [45]. The panels were produced by Hydro Aluminium at Raufoss in Norway, and were intended to be used as the deck of a bridge [46]. The panel consist of two 6 mm thick plates separated by four 3 mm thick slanting webs, providing three cavities and a total panel thickness of 130 mm. The cross section outline is shown in Figure 3.1.

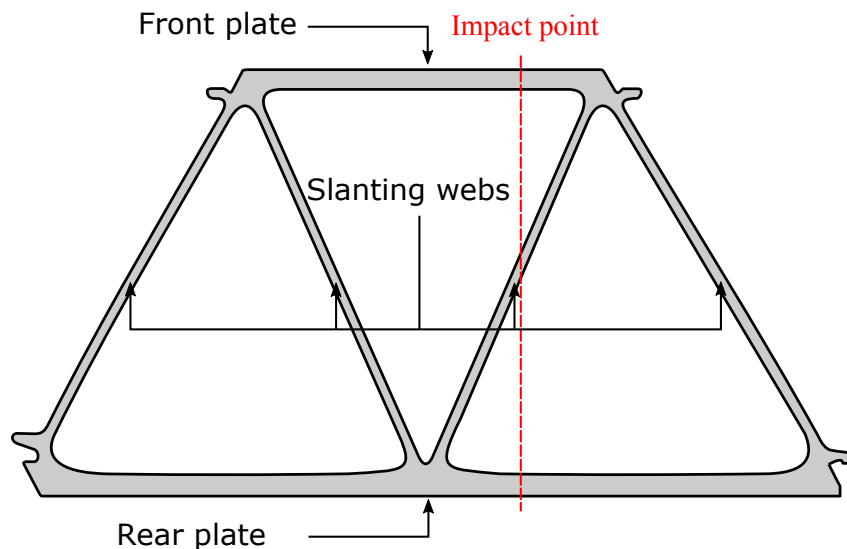


Figure 3.1: Outline of panel cross section and plate naming.

The panels were made by extrusion, which is a process where the panel start out as a aluminium log (billet). The billet is forced to flow through a smaller die opening by a ram as shown in Figure 3.2. Material in the center of the billet will essentially undergo pure

elongation due to the change in cross section. While the material near the container walls undergoes extensive shear deformation due to friction from the billet-container and die [47]. The mechanical properties of extruded aluminium alloys are highly dependent of the ram speed, deformation rate and extrusion temperature [48]. The chemical composition of the AA6005-T6 panels is shown in Table 3.1, where the main additives are magnesium and silicon.

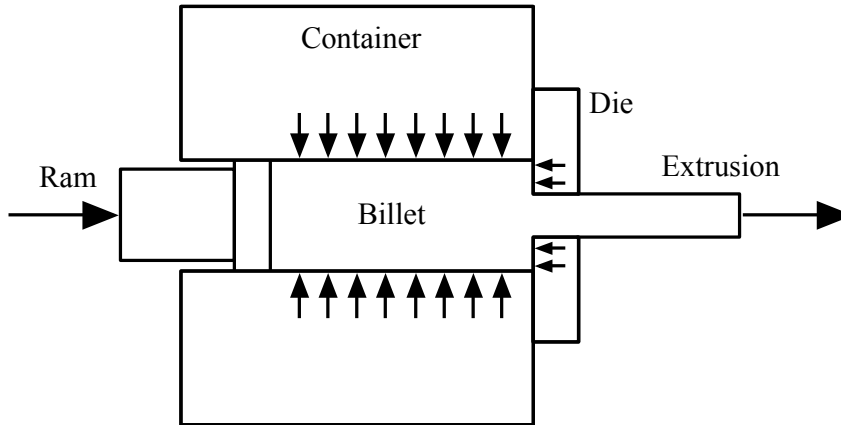


Figure 3.2: Concept of extrusion [47].

Table 3.1: Chemical composition of aluminium alloy 6005 [49].

Silicon (Si)	Magnesium (Mg)	Manganese + Chromium (Mn + Cr)	Others*	Aluminium (Al)
0.50-0.90 %	0.40-0.70 %	0.12-0.50 %	0.0-1.75%	Balance

* Including manganese, iron, copper, chromium, zinc and titanium

The front plate, rear plate and slanting webs from different panels were measured in the thickness direction in the impact trajectory to check for variation in thickness. The results are shown in Table 3.2.

Table 3.2: Measurements of panel plate thicknesses in the impact trajectory.

	Web*	Front**	Rear**
Mean value	3.08	6.62	5.82
Standard deviation	0.06	0.04	0.06

* from four measurements.

** from five measurements.

3.2 Granular Media

Three different fractions of sand have been investigated as granular filling material in this study. The median grain sizes are 0.15 mm, 0.55 mm and 0.95 mm, and they are in the following referred to as B15, B55 and B95, respectively. All the three types of fractions are quartz sand excavated from Baskarp, Sweden. The chemical components and grading curves are given in Table 3.3-3.5 (Appendix A) and Figure 3.3 respectively. As can be seen, the bulk constituent of the sand is silica (silicon dioxide, or SiO_2). Its chemical inertness and considerable hardness makes this to one of the most common minerals resistant to weathering [50].

According to the International Scale ISO 14688-1, the sand used in this experiment are classified in the range from fine to coarse sand [51]. Comparison between grain morphology, regarding size and appearance of the three sand fractions can be seen in Figure 3.3b, 3.3d and 3.3f. As most beach sands, these three sand fractions would be characterized as very poorly graded soils, with coefficient of uniformity (C_u) ranging from 1.46-2.42 and a coefficient of curvature (C_c) ranging from 0.95-1.08 [52]. The B95 fraction is the the most well graded in terms of these calculations. The C_u and C_c parameters are defined as

$$C_u = \frac{D_{60}}{D_{10}} \quad C_c = \frac{D_{30}^2}{D_{10}D_{60}} \quad (3.1)$$

where D_{10} , D_{30} and D_{60} are the grain size diameter where 10 %, 30 % and 60 % passes the sieve respectively.

Table 3.3: Chemical components in B15.

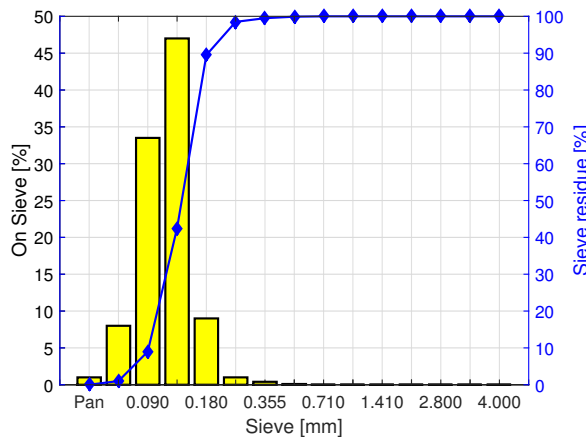
	SiO_2	Al_2O_3	Fe_2O_3	CaO	MgO	Na_2O	K_2O
Fraction [%]	90.1	5.3	0.57	0.42	0.11	1.20	2.06
Uncertainty [%]	± 0.5	± 0.3	± 0.02	± 0.01	± 0.01	± 0.03	± 0.04

Table 3.4: Chemical components in B55.

	SiO_2	Al_2O_3	Fe_2O_3	CaO	MgO	Na_2O	K_2O
Fraction [%]	77.1	12.5	1.42	1.03	0.34	3.04	4.19
Uncertainty [%]	± 0.5	± 0.5	± 0.05	± 0.02	± 0.01	± 0.06	± 0.08

Table 3.5: Chemical components in B95.

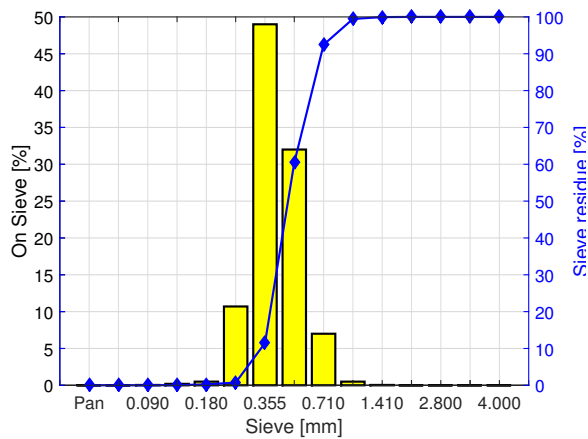
	SiO_2	Al_2O_3	Fe_2O_3	CaO	MgO	Na_2O	K_2O
Fraction [%]	88.5	6.3	0.50	0.50	0.10	1.39	2.61
Uncertainty [%]	± 0.5	± 0.3	± 0.02	± 0.01	± 0.01	± 0.03	± 0.05



(a) Sieve analysis of B15



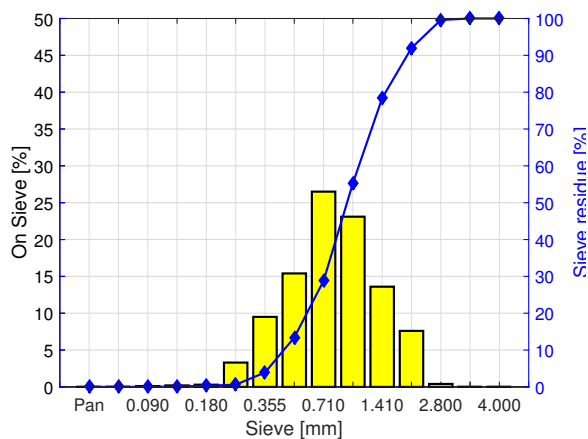
(b) Typical sample of B15



(c) Sieve analysis of B55



(d) Typical sample of B55



(e) Sieve analysis of B95



(f) Typical sample of B95

Figure 3.3: (a,c,e) show gradation tests from Appendix A of the sand fractions (Yellow bars (On sieve), blue grading curve (Residual)) and (b,d,f) display sample photos of each sand fraction.

Packing Density

Loose and compact sand density is measured by filling a 1 liter cylinder (Figure 3.4). For loose density the sand is only filled inside the cylinder with no compaction. To measure compact density the sand was compacted by tapping the sides of the container with a rubber hammer before the top was smoothed. Both loose and compact density were measured three times, with the average used in the numerical analysis. The density for all three fractions of sand became 11.5-13.0 % heavier. The density of solid sand was taken to be 2.6-2.7 kg/m³ from the data sheet, giving a volume fraction ϕ of 0.61-0.65 for dense sand, and 0.54-0.59 for loose sand, where the volume fraction is defined as total mass density divided by the solid density of sand. The measurements are in good agreement with similar types of quartz sand, like Ottawa sand with dense mass density of 1750 kg/m³ [53], and Quikrete#1961 sand with density as poured of 1550 kg/m³ and compact density of 1730 kg/m³ [54].



Figure 3.4: 1 liter container used to measure loose and compact sand density.

Table 3.6: Measured loose and compressed density for the sand fractions used.

Fraction	Weight (kg/m ³)	Consolidation	Average (kg/m ³)	Weight gain (%)
B15	1433.8	Loose	1431.0	13.9
	1431.9			
	1427.2			
	1635.2	Compact	1629.2	
	1620.6			
	1631.9			
B55	1501.5	Loose	1514.9	11.9
	1522.3			
	1520.8			
	1694.0	Compact	1694.5	
	1699.6			
	1689.8			
B95	1555.0	Loose	1552.9	11.5
	1563.5			
	1551.2			
	1732.2	Compact	1731.3	
	1717.5			
	1744.2			

Water Content Measures

The moisture content of the three different sand fractions was found to be between 0.30-0.42 %. These values were found by taking a sample of 500 grams, drying it, and weighing it afterwards. Saturation degree is a ratio number describing how much of the total void volume in a material that is filled with liquid. Saturation degrees were calculated using Equation 3.2 and found to lie between 1.49-1.76 % for dense sand and 1.12-1.30 % for loose sand. The total calculation is shown in Appendix B, and are in good agreement with typical values for standard Ottawa sand [55].

$$u = \frac{m_{wet} - m_{dry}}{m_{dry}} \quad S_w = \frac{V_w}{V_v} \quad (3.2)$$

where u is moisture content, m_{wet} is wet mass and m_{dry} is dry mass. S_w is the degree of saturation, V_w is liquid volume and V_v is total volume of voids [55].

Table 3.7: Calculated moisture content and degree of saturation for the three different sand fractions used.

	B15		B55		B95	
	dense	Loose	dense	Loose	dense	Loose
Wet measured (g)	500.1	500.1	500.0	500.0	500.0	500.0
Dry measured (g)	498.0	498.0	498.4	498.4	498.5	498.5
Moisture content	0.42 %	0.42 %	0.32 %	0.32 %	0.30 %	0.30 %
Degree of saturation	1.76 %	1.30 %	1.50 %	1.13 %	1.49 %	1.12 %

Chapter 4

Ballistic Experiments: AA6005-T6 Panels

In this chapter ballistic experiments on empty and sand-filled panels are presented. The objective was to establish the ballistic limit curves and capture any differences in ballistic performance between empty and sand-filled panels, and in-between the different sand fractions (Figure 3.3). A total of 49 tests were performed on the aluminium panels in the nominal ordnance velocity range using a powder gun.

4.1 Experimental Work

All the ballistic impact experiments on AA6005-T6 panels were conducted in a 16 m³ impact chamber (Figure 4.1) at SIMLab, NTNU. A smooth-bored Mauser gun with a barrel length of 1 m was fixed inside the chamber (Figure 4.2a) and used to fire 7.62 mm APM2 bullets. All experiments were filmed with Phantom V1610 high-speed cameras (Figure 4.2b).

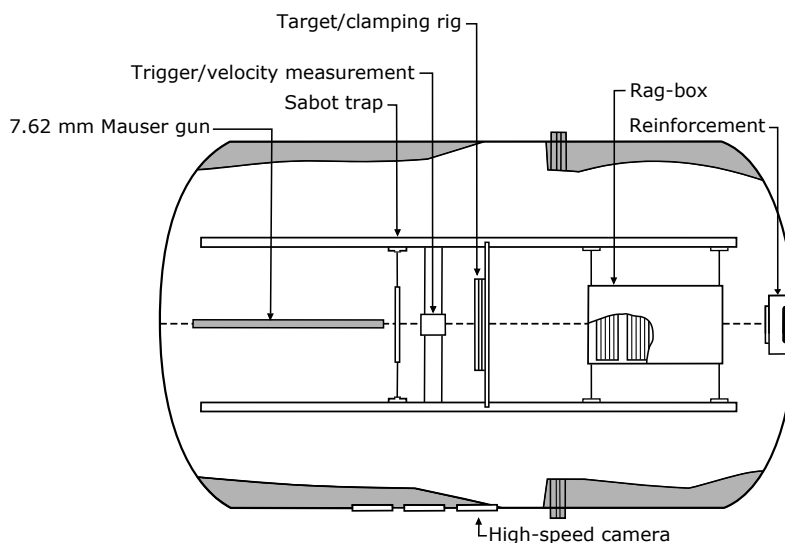
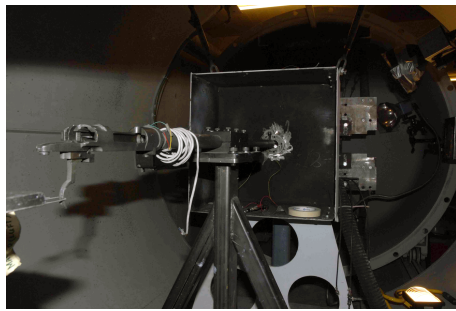
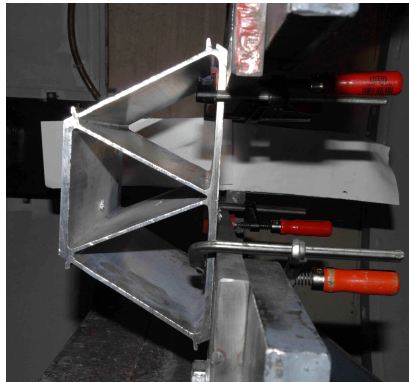


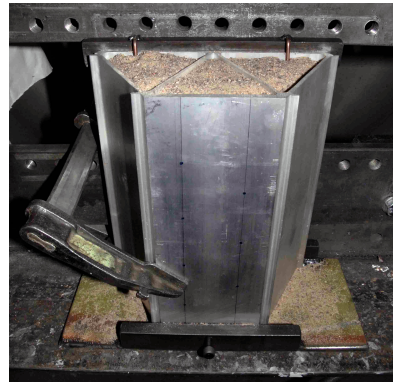
Figure 4.1: Schematic of experimental set-up.

(a) 7.62 mm \times 63 Mauser

(b) Phantom V1610 high speed cameras



(c) Boundary condition for shot 1-3



(d) Boundary condition for shot 4-49

Figure 4.2: Set-up experimental work.

The boundary condition visualized for shot 1-3 (Figure 4.2c) was used in order to capture the whole perforation process of empty panels. The remaining tests were carried out using the boundary condition in Figure 4.2d. The former was filmed with one camera operating at 60 000 fps and a recording resolution of 1024×256 pixels, while the latter with two cameras at 80 000 fps and 512×304 pixels.

The 7.62 mm APM2 bullet is shown in Figure 4.3 and consists of four parts: lead tip, steel core, brass sabot and brass jacket. The steel core has an ogival nose shape and is made of hardened tool steel with a Rockwell C hardness factor of 63 [5]. A brass sabot and jacket are used to cover the steel core for corrosion resistance during long periods of storage [56]. The lead tip is added to improve stabilization during flight and in the initial stage of penetration [5]. The geometry and mass properties of every part are summarized in Table 4.1.

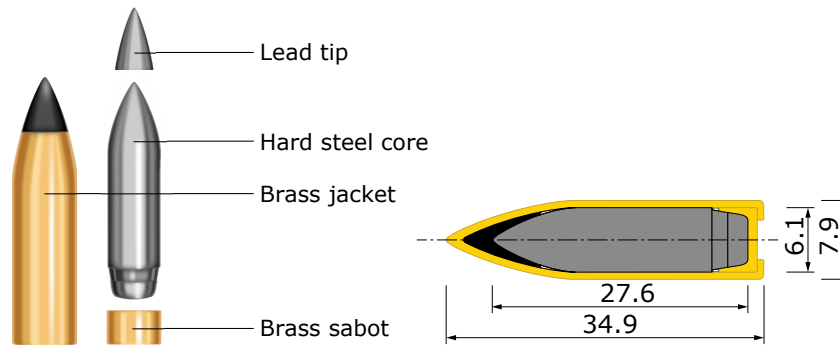


Figure 4.3: 7.62 mm \times 63 APM2 ammunition, redrawn per Børvik et al. [1].

Table 4.1: Geometry and mass properties of 7.62 mm \times 63 APM2 ammunition [57].

Brass jacket			Steel core			Lead cap			Brass sabot		
l	d	m	l	d	m	l	d	m	l	d	m
(mm)	(mm)	(g)	(mm)	(mm)	(g)	(mm)	(mm)	(g)	(mm)	(mm)	(g)
34.9	7.9	4.4	27.6	6.1	5.0	9.3	5.1	0.7	4.0	6.2	0.4

The bullets were fired from the Mauser by a magnetic trigger with the objective to establish the ballistic limit curves and ballistic limit velocity. Different velocities were achieved by changing the amount of powder, giving initial velocities between 450 m/s and 900 m/s. The target was cut in lengths of 40 cm and fixed to the clamping rig inside the impact chamber. A cross section of the panel can be seen in Figure 4.4. Deformation was limited to a small area around the impact trajectory, such that multiple shots could be taken in each panel. The target panels have been studied with an impact point about 27.5 mm from the center of the panel, so that the bullet impacted with an oblique angle in the middle of the slanting web. In a realistic view, the possibility to hit along a slanting web is large, though this may not be the region giving least resistance to ballistic impact. The same impact point was considered by Børvik et al. [2, 46].

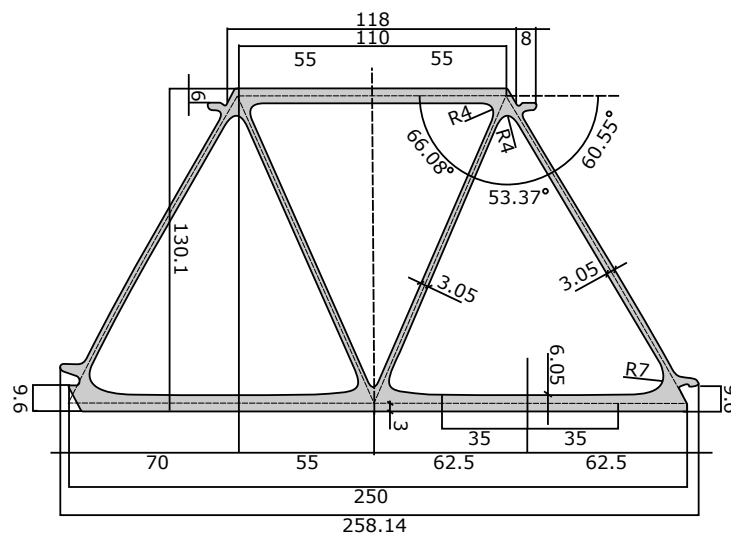


Figure 4.4: Extruded AA6005-T6 aluminium panel, redrawn per Børvik et al. [57].

In practical use with continuously mounted profiles, the shape and mounting would cause a double slanting web at the connection points. Thinking about material costs and transportation weight of the system, this could be considered as redundant, so the profile's geometry may be better optimized for this specific use. Also discussed in Børvik et al. [2].

The ballistic testing for sand-filled panels was preceded by pouring sand in the cavities of the panels, with a plate mounted at the bottom to ensure that the sand remained in place. The sand inside the panel was then compressed by knocking the panel with a rubber hammer. More sand was added as the sand got rearranged and compressed. This process was repeated until the panel was completely filled, such that the packing densities were approximately the same in all tests. The tests sequences for the sand-filled panels were performed from top to down with the first shot at the top and the last shot at the bottom. Only five shots were fired at each panels to ensure sufficient distance between the tests.

4.2 Experimental Results

The initial and residual velocities were calculated by measuring the time and distance between two positions before and after impact. This was done by determining the length of each pixel from the high-speed video images, resulting in the horizontal velocity. The results from the ballistic experiments can be viewed in Table 4.2. Bullet parts after testing are shown in Figure 4.5.

Table 4.2: Experimental results

Filling	Test	Gunpowder (g)	v_i (m/s)	v_r (m/s)	Comment
	1	Full	896.0	730.5	-
	2	38.0	701.5	516.5	-
	3	37.0	617.9	408.7	Oblique exit
	4	36.0	618.9	386.8	-
	5	35.0	620.6	371.4	Projectile split in two
Empty	6	32.0	581.4	386.3	-
	7	30.0	534.9	292.6	-
	8	27.0	448.8	0.0	Turned inside panel
	9	28.0	450.1	0.0	-
	10	29.0	486.9	185.1	-
	11	-*	797.9	649.1	Oblique exit

Continues on next page

Table 4.2 – continued from previous page

Filling	Test	Gunpowder (g)	v_i (m/s)	v_r (m/s)	Comment
B95	1	Full	910.5	485.4	-
	2	38.0	693.6	217.9	-
	3	37.0	641.7	0.0	-
	4	*	823.5	397.4	-
	5	41.0	734.3	0.0	Turned inside panel
	6	41.5	685.4	0.0	-
	7	41.5	734.3	203.2	Oblique exit
	8	42.0	745.7	324.9	-
	9	37.0	690.6	89.1	Oblique exit
	10	37.0	654.6	0.0	-
	11	42.0	767.5	291.8	-
	12	50.0	900.8	377.9	-
B55	1	Full	900.2	459.5	-
	2	38.0	720.2	277.4	-
	3	37.0	662.2	160.3	-
	4	36.0	682.3	148.3	-
	5	35.0	643.6	0.0	-
	6	*	821.0	399.3	-
	7	36.0	648.6	0.0	-
	8	42.0	745.9	248.7	-
	9	49.0	884.8	311.4	Oblique exit
	10	48.5	874.8	276.1	Oblique exit
B15	1	Full	905.4	374.8	Projectile split in three
	2	38.0	707.9	246.8	-
	3	36.0	671.1	0.0	-
	4	*	826.1	383.8	-
	5	36.0	662.4	75.3	-
	6	Full	892.6	324.0	-
	7	Full	887.5	392.9	-
	8	*	831.2	364.3	-
	9	35.5	641.1	0.0	-
	10	42.0	754.9	239.9	-
	11	Full	896.8	336.2	Oblique exit
	12	Full	872.8	384.4	-
	13	53.0**	939.1	330.9	Oblique exit
	14	43.0	758.3	169.4	-
	15	37.5	654.6	0.0	-
	16	45.0	755.0	167.4	-

* Pre-made bullet $v_i \approx 800$ m/s, **Different gunpowder



Figure 4.5: Bullet cores and jackets after the testing. Original bullet at the top.

4.2.1 AA6005-T6 Panels without Sand

The eleven shots fired at the empty panels gave predictable results, i.e. the results adhere well to the Recht-Ipson Equation 2.1. Entry and exit holes for the ten first shots can be seen in Figure 4.6. This shows that the perforation of the front plate is similar for all shots, even though some of the shots had small pitch angles and probably also yaw angles, as seen in Figure 4.7. Oscillations are observed in the aluminium panel during and after the penetration process, especially in the slanting web. The slanting web has a big effect on the bullets trajectory with respect to the final oblique, especially for low initial velocities. This is clearly seen from the scatter of the exit hole positions in Figure 4.6b. The reason for this may be that the web thickness combined with the angle affects the bullet enough to be appreciably rotated. This is an opposite observation to what is observed for the 20 mm projectile used in Børvik et al. [46]. They observe small oblique angles as the projectile perforates the slanting web. The varying behaviour may be due to the projectiles different masses and geometries.

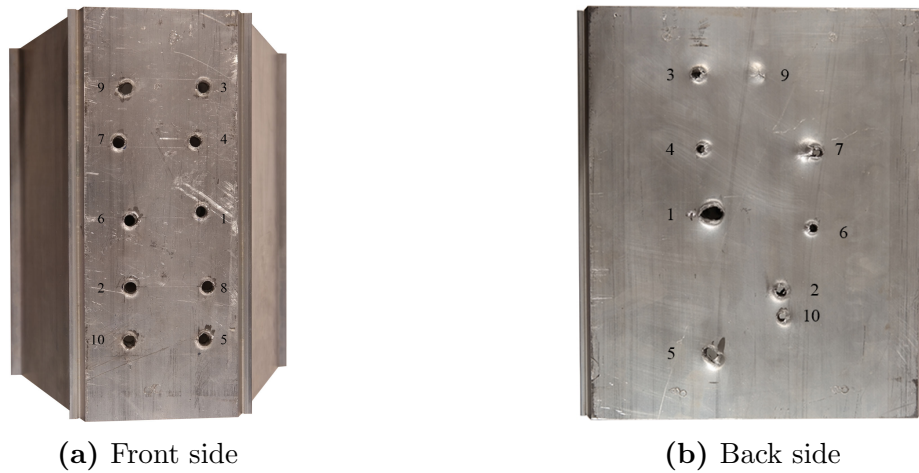


Figure 4.6: Empty AA6005-T6 panels impacted by 7.62 mm APM2 bullets, front and back side.

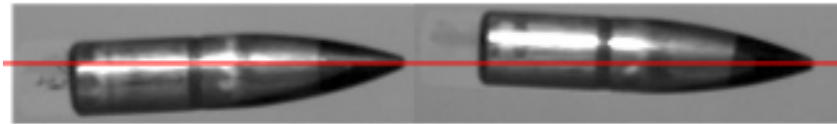


Figure 4.7: Bullet with lopsided angle before impact. Left shot No. 9 and right shot No. 10, both from empty panel testing.

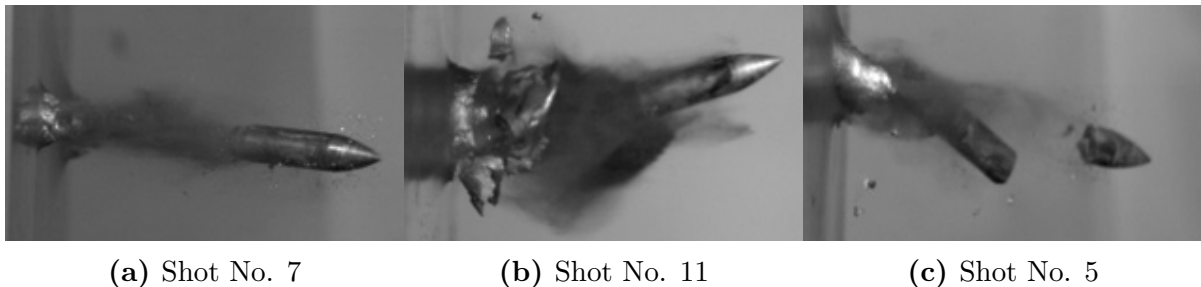
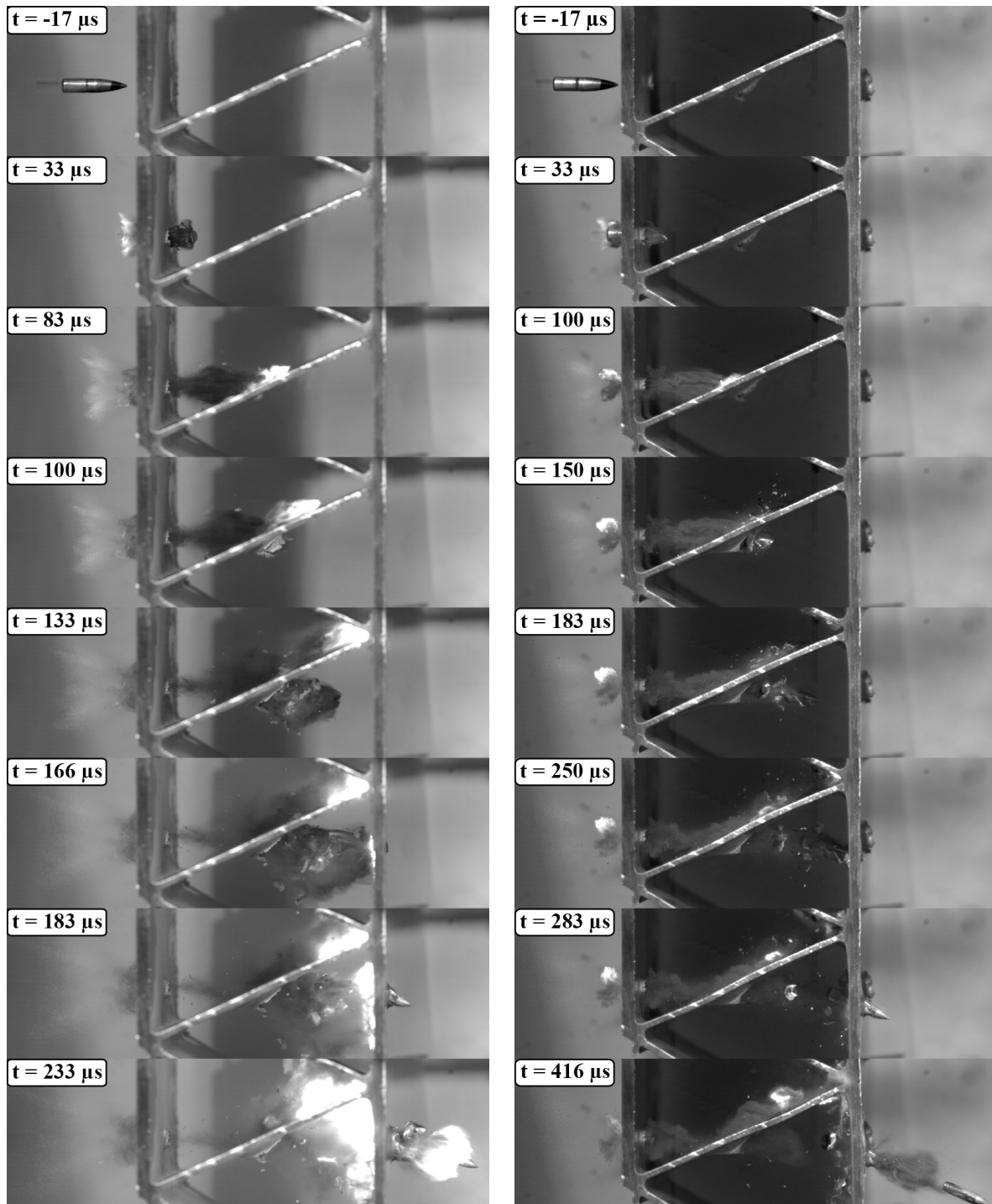


Figure 4.8: Bullet after impact; (a) the most common, where the rear plate fails predominantly by ductile hole growth, (b) fragmentation of the rear plate and an oblique exit of the steel core, and (c) steel core split in two during the perforation process.

Time-lapses from the high-speed camera for shot number one and three can be seen in Figure 4.9. An interesting observation is that the bullet changed oblique angle in the opposite direction of the slanting web in the first three tests, and conceivably also in the other tests. Note also that the jacket is peeled off during the perforation of the rear plate. Due to camera angle and wideness of the panels, it was difficult to photograph both the entry and exit of the bullet simultaneously. The top photo in the time-lapses was therefore selected to show the whole bullet. This is one picture before the bullet hit the panel, thereby giving a time of $-17 \mu\text{s}$.

By studying Figure 4.6 and 4.9 one can see that the main failure mode in the front and rear plate is ductile hole growth in combination with some petaling. While the slanting web mainly suffers from fragmentation (Figure 4.9). In shot No. 1 and 11 the rear plate also suffers from fragmentation. Shot No. 8 rotated inside the panel after impacting the web and embedded in the neighbouring web. The full trajectory is illustrated in Figure 4.10.



(a) Shot 1, $v_i = 892$ m/s and $v_r = 730.5$ m/s (b) Shot 3, $v_i = 617.9$ m/s and $v_r = 408.7$ m/s

Figure 4.9: Shot No. 1 and 3 without Sand.

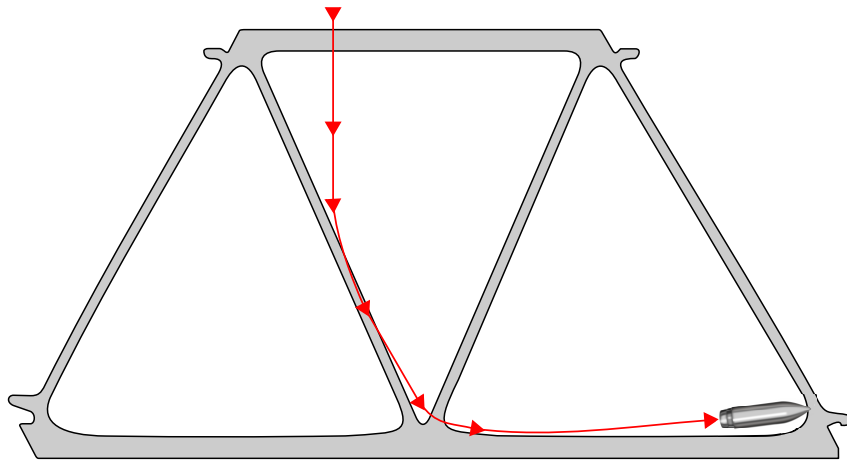


Figure 4.10: Illustration of trajectory for shot No. 8.

4.2.2 AA6005-T6 Panels with Sand

The panels were filled with sand B95, B55 and B15 shown in Figure 3.3 and supported as shown in Figure 4.2d. A total of 38 shots were fired on the aluminium panels filled with sand: 12 tests on B95, 10 tests on B55 and 16 tests on B15. The five first shots on every fraction are shown in Figure 4.11.

Shot No. 5 in B95 turned inside the panel as in shot No. 8 for empty panel testing. The bullet trajectory is illustrated in Figure 4.10. Note that the jacket was peeled off during perforation of the web when sand is filled in the panel cavities, contrary to the empty panels where the jacket was stripped off by the rear plate.



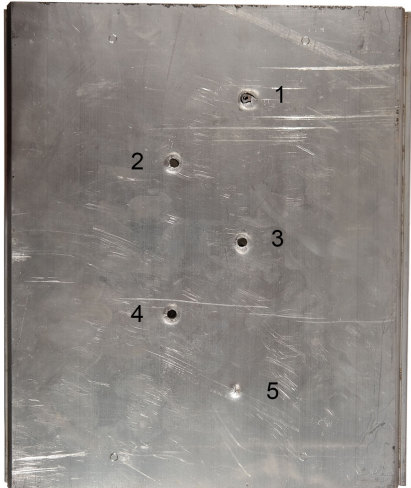
(a) B95 front side



(b) B95 back side



(c) B55 front side



(d) B55 back side



(e) B15 front side



(f) B15 back side

Figure 4.11: Entry and exit holes of AA6005-T6 panels filled with sand impacted by 7.62 mm APM2 bullets.

Figure 4.12 shows a time-lapse of shot No. 2 performed on B15 sand. The front plate failed in the same manner as without sand, while no fragmentation was seen in the rear plate for sand-filled panels. The sand seems to support the slanting web and reduce the amount of fragmentation in this area. Overall small differences are seen between the different fractions of sand.

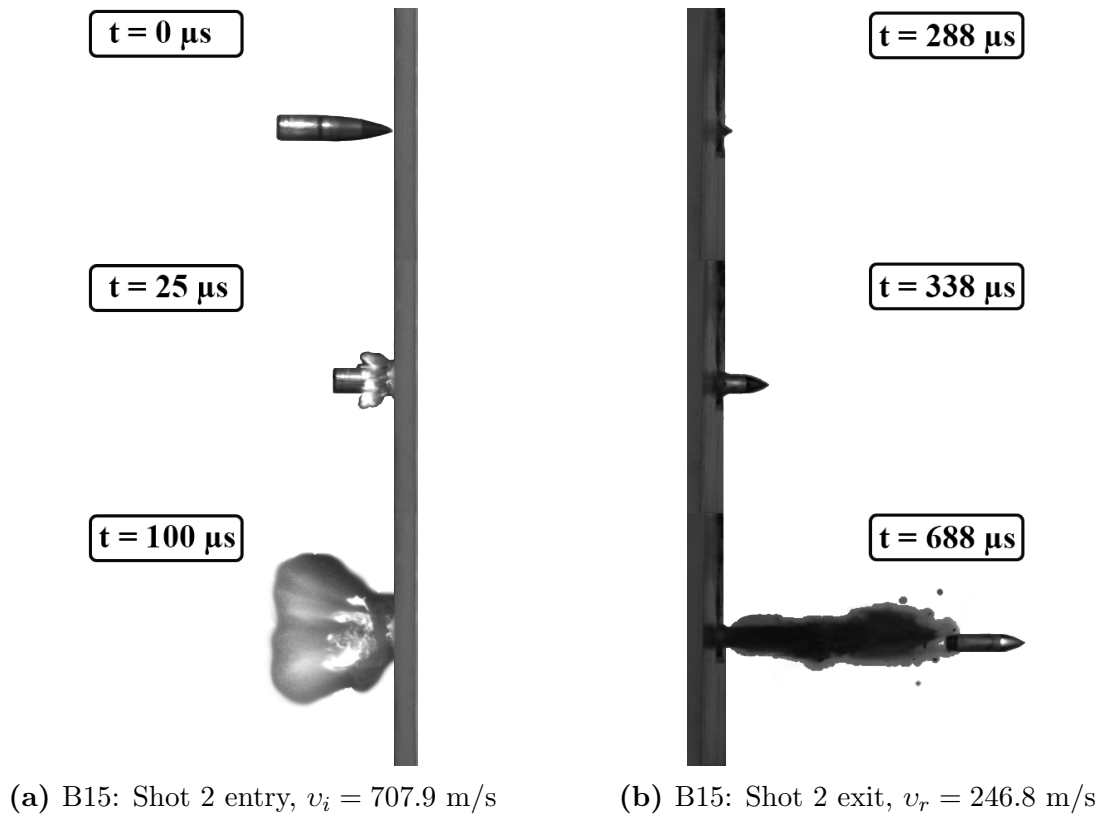
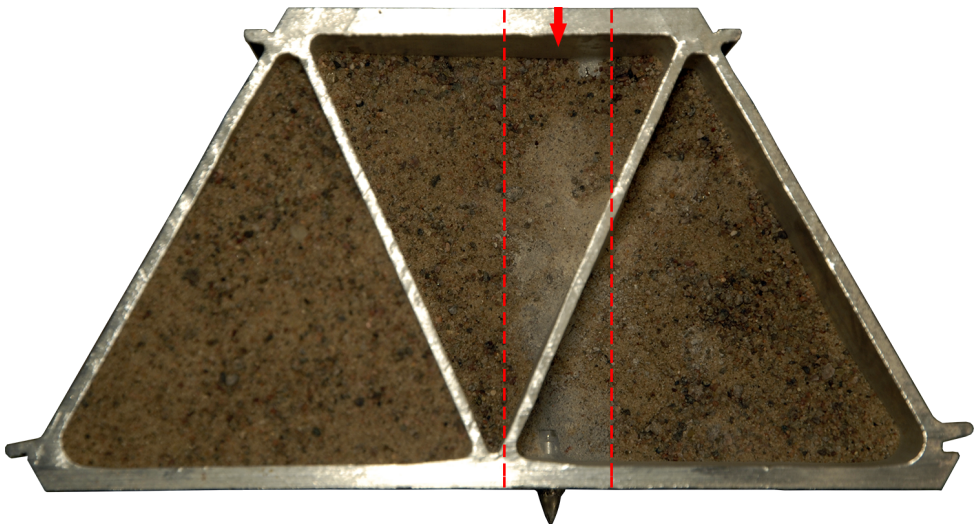


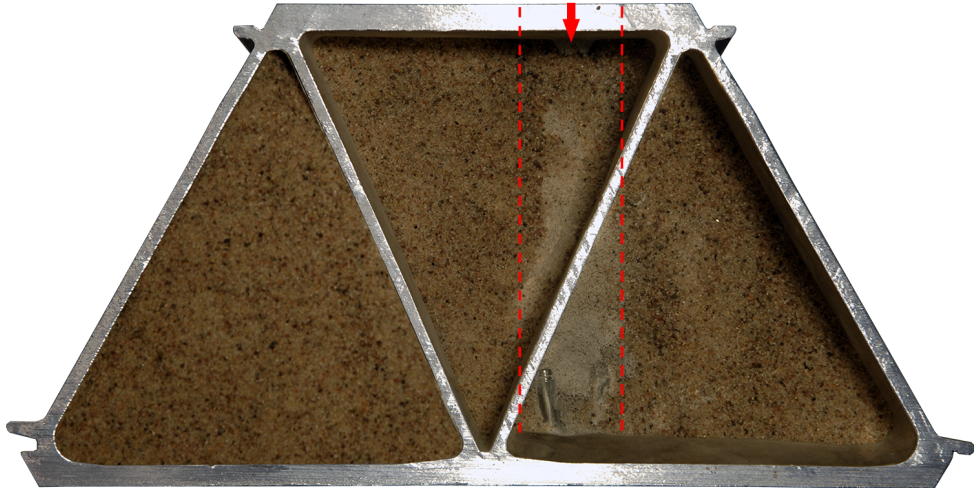
Figure 4.12: Shot No. 2 with B15 sand.

Comminution of Sand (The White Trail)

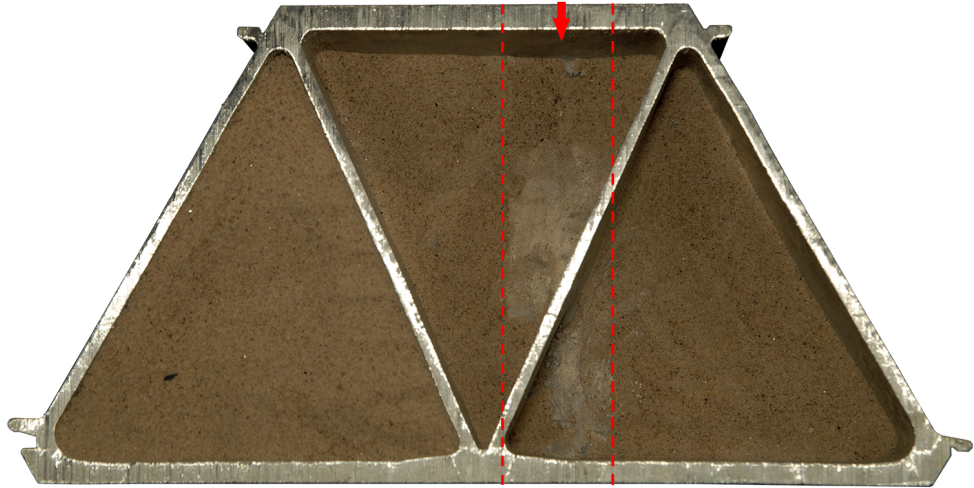
Evidence of fracture in the sand is clearly found in the projectile path. By carefully removing the overlaying sand, the bullet's trajectory is revealed together with a layer of fractured sand. This layer can be seen for every sand fraction in Figure 4.13. The fractured sand was found both in loose state and in very compact clumps of fine powder. Both consistency and color made it feel and look like potato starch. The base material of quartz is in fact colorless and transparent but because of surface contamination from other materials the sand has a tan color. Therefore this bright white color is found when the quartz gets fractured [54]. The white trail from the projectile path has also been observed by others [53, 5, 54, 58]. It seems to be a common effect in sand penetration at a velocity above about 100 m/s. Sand and projectile before and after impact are displayed in Figure 4.14. Here the fractured sand in the white trail is compared with unused sand.



(a) B95



(b) B55



(c) B15

Figure 4.13: The white trail of fractured sand in the projectile path. The pictures should be considered in colour for details.



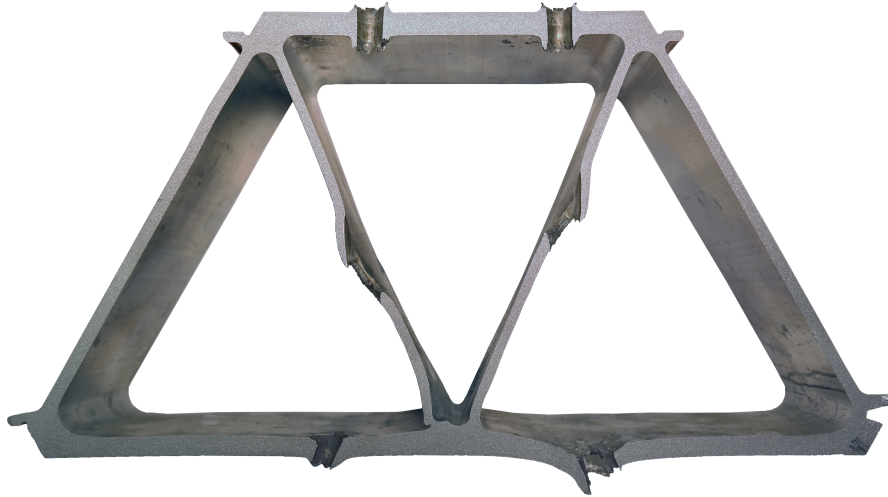
Figure 4.14: Sand and projectile before and after impact, presented for B95.

4.2.3 Cross Sections

Cross sections for both empty and sand-filled panels are shown in Figure 4.15. One can clearly see the thickening around the bullet hole in the front and rear plate for both cases, characteristic for ductile hole growth. The slanting web fails somewhat differently when the cavities in the panel are filled with sand. Less fragmentation and less sliding are seen during penetration.

The reduction in fragmentation may be because of the sand supporting the web and the change in jacket response, which is peeled off during the perforation of the rear plate for empty panels and in the slanting web for sand-filled panels, see Figure 4.16. In some shots fragments from the brass jacket hits the connection between the web and rear plate, initiating the fracture seen in this area. For two shots with initial velocity below the ballistic limit, the bullet did not perforate the slanting web, only slid and rotated inside the panel. These sliding marks are shown in Figure 4.17 for shot No. 5 with B95 sand. Note the cracking of the back side.

An interesting observation is that the bullet hole orientation in the rear plate is rotated in opposite directions for empty panels and sand-filled panels. The reason for this can be that the sand is stabilizing both the bullet and web during penetration, while for empty panels the bullet is free to rotate.



- (a) Cross section from AA6005-T6 panel without sand perforated by a 7.62 mm APM2 bullet. Left: Shot 4 $v_i=618.9$ m/s, $v_r=386.3$ m/s. Right: Shot 7 $v_i=534.9$ m/s, $v_r=292.6$ m/s.



- (b) Cross section from AA6005-T6 panel filled with B95 sand perforated by a 7.62 mm APM2 bullet. Shot 1 $v_i=910.5$ m/s, $v_r=485.4$ m/s.

Figure 4.15: Cross sections of empty and sand-filled panels.

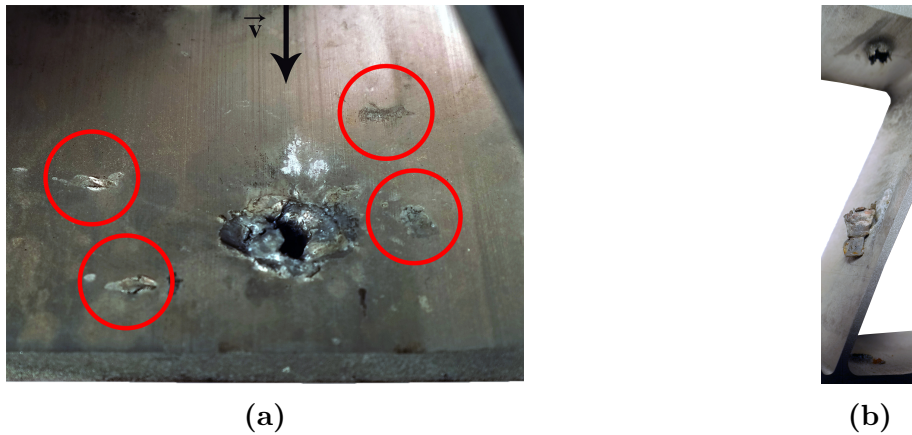


Figure 4.16: Jacket response, (a) fragment marks from the slanting web (marked with red circles) and jacket marks around the entry hole in the rear plate from empty panel, (b) jacket stopped in the web for sand-filled panels.

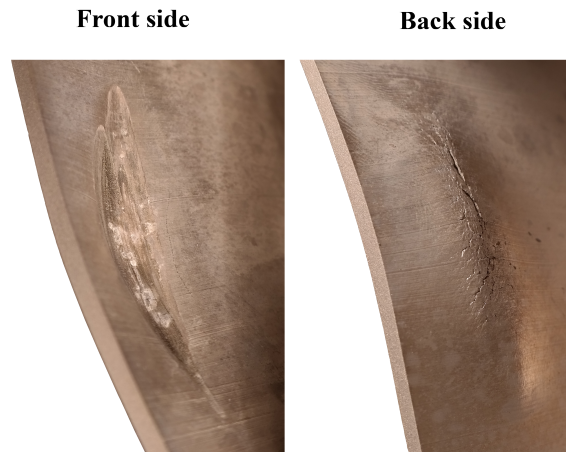


Figure 4.17: Sliding marks on web, front and back side, from shot No. 5 with B95 sand.

4.2.4 Ballistic Limit Velocities

Experimental data from Table 4.2 are plotted as a scatter in Fig 4.18. The analytical model originally proposed by Recht and Ipson (Section 2.5) is used to create the trend lines through the data points. The parameters in this model, a , p and v_{bl} were found by minimizing the sum of squares between the model and experimental data. The curve establishment was done with two constraints. Firstly, v_{bl} could not be higher than the lowest initial velocity (v_i) penetrating the panel. Secondly, all data points with zero residual velocity (v_r) are discarded from the calculation. The parameters used to get the different curves can be seen in Table 4.3.

Even though only a limited number of experiments were performed, the ballistic limit velocity can be established in a satisfying manner. From Figure 4.18 the difference between empty and sand filled panels regarding ballistic performance is clearly seen. By filling the cavities in the aluminium panel the ballistic performance is improved by at least 32.5 %. The differences between each sand fraction, B15, B55 and B95 are rather small.

Table 4.3: Ballistic limit velocity of empty and sand-filled AA6005-T6 panels impacted by 7.62 mm APM2 bullets.

Type	a	p	v_{bl} (m/s)	Difference (%)
Empty	0.98	1.86	436.7	-
B95	0.49	5.51	690.6	36.8
B55	0.47	3.43	646.9	32.5
B15	0.52	2.73	661.0	33.9

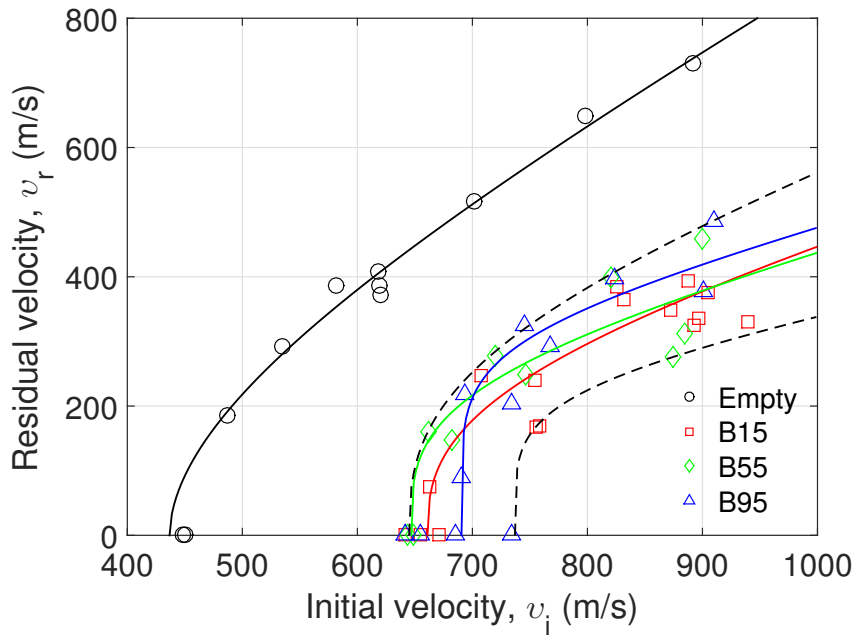


Figure 4.18: Initial versus residual velocity for empty and sand filled panels impacted by 7.62 mm AP bullets.

Børvik et al. [2] conducted experiments on the same AA6005-T6 aluminium panels with sand 0-2 mm ($d_m=0.65$ mm), gravel 2-8 mm (median of 4.8 mm), crushed stone 8-16 mm ($d_m=11.4$ mm) and crushed rock 16-22 mm ($d_m=19$ mm). Experimental results in terms of ballistic limit for 7.62 mm APM2 bullets are plotted against median grain size in Figure 4.19. Crushed stone ($d_m=11.4$ mm) and crushed rock ($d_m=19$ mm) do not perforate the panel at muzzle velocity, thus the ballistic limit velocity is greater than 900 m/s for these cases. Børvik et al. [2] concludes that the protective panel will perform best if the filling material has a diameter equal to or larger than the bullet's diameter, and with a grain size of at least 8-22 mm.

There is a clear gap in ballistic limit velocity between the sand with median grain size of 0.65 mm from Børvik et al. [2] and the sand fractions used in this thesis. This may be due to different gradations in the sand fractions, since more well graded sands have been found to give better resistance to penetration [59]. The sands tested in this thesis are poorly graded, $C_u=1.5-2.4$, while the sand tested in Børvik et al. [2] is more well graded, $C_u \approx 4.3$ [5].

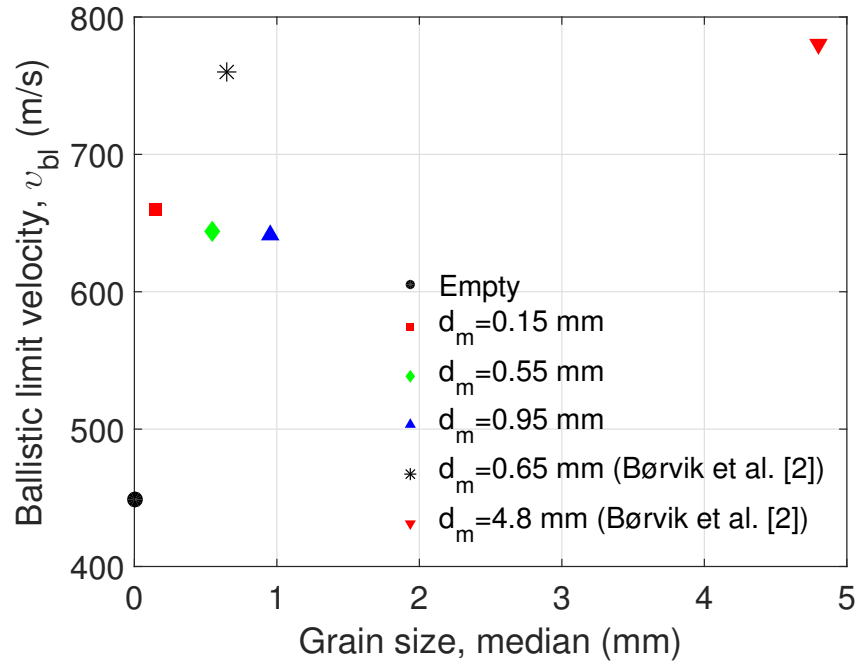


Figure 4.19: Ballistic limit velocity versus grain size for different sand types, additional data from Børvik et al. [2].

Chapter 5

Component Experiments

In this chapter experimental work on sand is presented. Sand was tested in the low velocity domain and subordnance domain. An Instron drop-tower rig was used for velocities of 2 m/s, 5 m/s and 10 m/s, while a gas-gun provided velocities of 280 m/s. These experiments were carried out to establish material constants for the sand model implemented in IMPETUS Afea Solver.

5.1 Compressed Gas-Gun (280 m/s)

5.1.1 Set-up Design

One of the challenges with using a granular material like sand is to establish the material properties, especially when high strain rates are considered. As discussed in Chapter 2, common testing methods to achieve HSR behaviour are uniaxial compression tests, triaxial compression tests, Split Hopkinson Pressure Bar tests and plane wave shock tests. These testing methods are found to give different results regarding stiffness, strength, confining pressure etc.

A special test set-up was designed on the basis of several numerical simulations. This set-up would need to give high enough strain-rates to be comparable with the ballistic tests in Chapter 4. The hypothesis was that such a test set-up could give just as good, or even more reasonable results for this intended use than traditional testing methods. Producing the high strain rate would anyway be difficult with these methods. With an alternative test method the need of a costly testing procedure was avoided in addition to lots of time saved regarding analysis of the results and making them applicable for the use in this thesis.

The numerical pre-design simulations were performed with the IMPETUS Afea Solver. The sand particles were placed in a cylindrical cloud with circular plates on both ends in the impact direction, see Figure 5.1. The plates were modelled as rigid to ensure the confining effect on the sand in the impact direction. The projectile was modelled as a

rigid sphere of steel with a density of 7800 kg/m^3 . Holes with diameters of 40 mm were placed in both plates in the projectile path, allowing sand grains to escape as they would in a physical test. Cubic elements were used around the plate holes and in the projectile to allow a smoother surface. The dry sand model implemented in IMPETUS Afea Solver was used, with the default parameters given in Table 5.1.

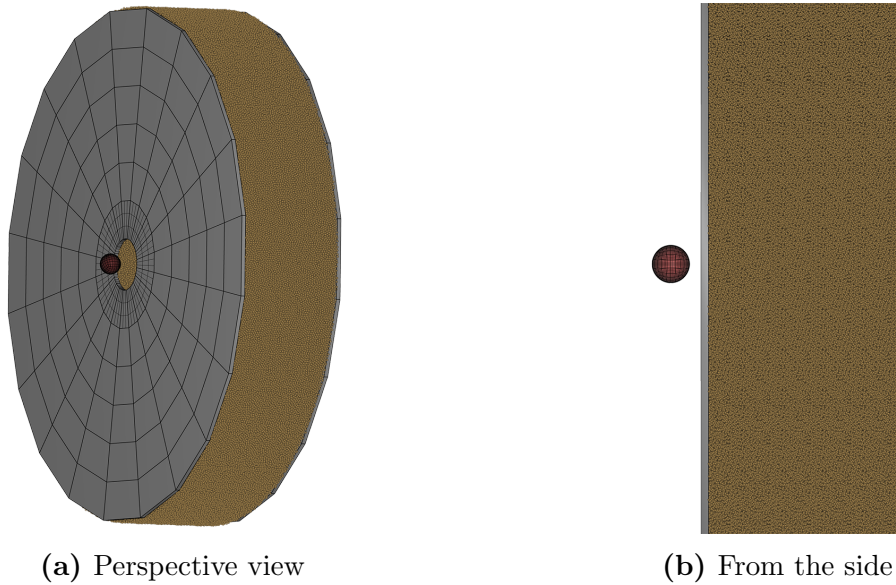


Figure 5.1: Numerical model sand container pre-design, with sand thickness of 50 mm and diameter 250 mm.

Table 5.1: Default parameters for dry sand in IMPETUS Afea Solver.

Soil packing scheme	Soil density kg/m^3	Contact stiffness N/m	Damping coefficient	Soil-soil friction	Soil-structure friction
1000	1620	4.0×10^8	0.0	0.1	0.0

A variety of projectile sizes, sand thicknesses, and impact velocities were analyzed to find the best suited design dimensions for the experimental testing. The results were evaluated first and foremost on the residual velocity: it had to be considerable lower than the initial velocity to be able to capture any effects from the sand. But not so low that the risk of projectile embedment would take place. In addition simplicity was an important aspect in the design phase. The reason was to avoid high costs and time consuming production, since a limited amount of time could be spent on these tests. The results of these simulations with varying sand thickness, projectile diameter and initial velocity are shown in Figure 5.2.

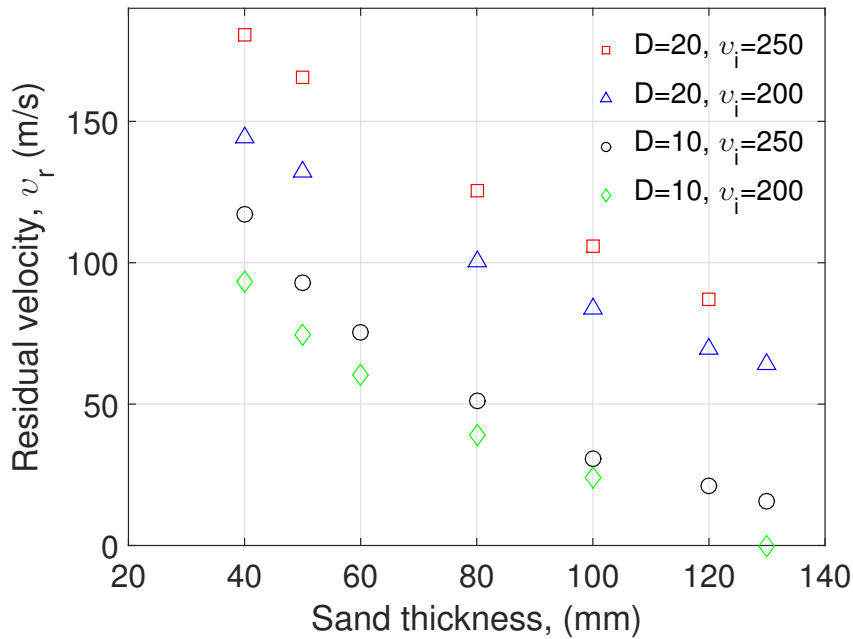


Figure 5.2: Sand thickness versus residual velocity, D =Projectile diameter (mm) and v_i =initial velocity (m/s).

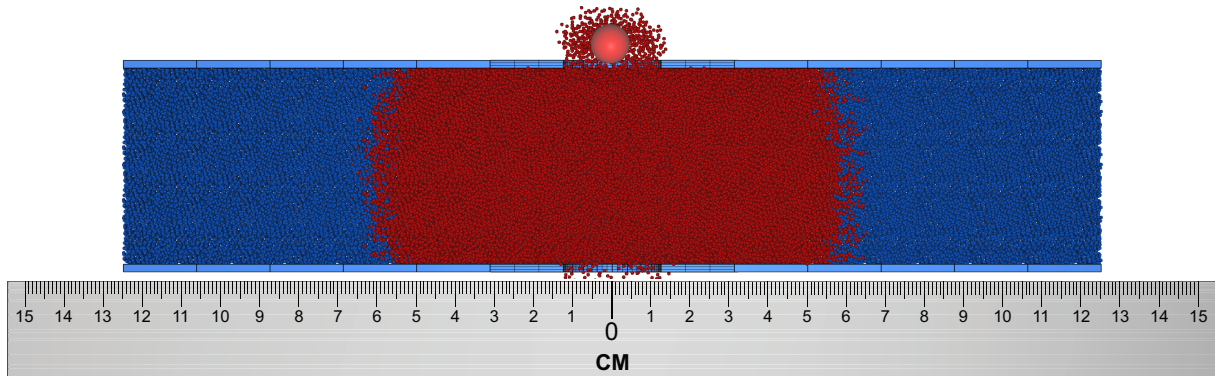
The analyses showed that the increased mass from changing the projectile diameter to 20 mm, lead as expected to an increased residual velocity. The sand thickness would therefore need to be increased, in order to get the same velocity reduction as for a projectile with diameter of 10 mm. It was also convenient that the sand container became relatively thin, to ensure easier handling and less sand consumption in the experimental testing. A sphere with a diameter of 10 mm, a sand thickness of 50 mm and an initial velocity of 250 m/s were therefore adopted to ensure a good drop in velocity as the projectile travels through the sand container.

New simulations with varying plate hole diameter and number of particles making up the sand cloud were then conducted. This was done to capture any effects the two parameters would have on the residual velocity. As expected a reduction of the hole diameter reduces the residual velocity. Probably because of less escaping possibilities for the sand particles adjacent to the hole, thus more resistance. When changing from a hole diameter of 60 mm to 25 mm, a reduction in residual velocity of 4.1 % is observed (Table 5.2). To be able to hit both the entry and the exit hole in the experimental tests, a hole diameter of 2.5 times the projectile diameter was selected. The number of particles was found to have a major effect on the residual velocity. This number is determining for the particle diameter. By varying the particle diameter from 2.82 mm to 0.78 mm (125 000 to 6 000 000 particles) the residual velocity changes from 82.5 m/s to 108.5 m/s, a reduction of 24 %. This is further discussed in Chapter 8.

Table 5.2: Effect of hole diameter on the residual velocity.

Diameter (mm)	v_i (m/s)	v_r (m/s)	Reduction (%)
60	250	93.6	-
40	250	92.8	0.9
25	250	89.8	4.1

Finally the sand box height and width had to be specified. The goal was to ensure that the velocity field of the sand particles did not reach the boundaries before the projectile had left the sand container. No effects from the boundaries were desired in the penetration process, so the sand containers height and width had to be larger than the spread in velocity field. The velocity field is shown just as the projectile leaves the sand box in Figure 5.3. The particles marked red have a velocity greater than 0 m/s. The velocity field spreads approximately 65 mm in every direction.

**Figure 5.3:** Velocity field as the projectile leaves the cylinder with sand thickness 50 mm.

The sand container's height and width were therefore selected to be 250 mm. This ensures that the velocity field does not exceed the dimensions of the box. In this way the boundary condition effects did not affect the residual velocity. The sand container design is shown in Figure 5.4 and drawings can be found in Appendix C. By a mistake the sand container was constructed with a height of 200 mm. In Chapter 6 it is shown that this error had no effect on the results.

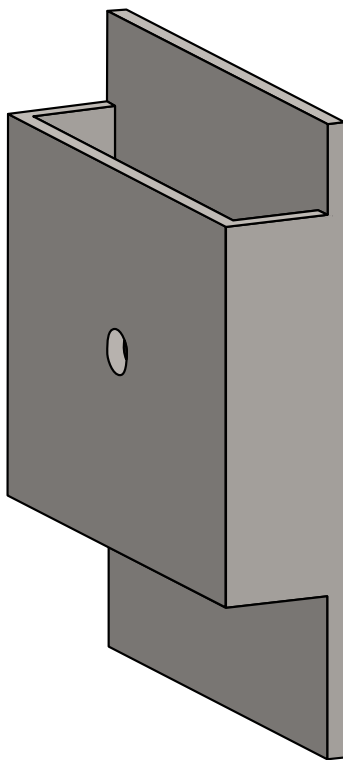


Figure 5.4: Final design of the sand container, $b \times h \times t = 250 \times 250(200) \times 50$ mm.

5.1.2 Experimental Set-up

The steel sphere projectile with a diameter of 10 mm was fired in the same impact chamber as the 7.62 APM2 bullets in Chapter 4, but the smooth bored Mauser was removed and a compressed gas-gun was used to fire the projectile. A schematic overview and pictures of the test set-up are shown in Figure 5.5 and 5.6. The experimental set-up consists of the impact chamber, two pressure chambers and the barrel. The experiments were filmed with the Phantom V1610 high-speed camera, operating at 60 000 fps and a recording resolution of 1280×208 pixels (Figure 5.6c). A trigger was used to activate the blitz and the high-speed camera (Figure 5.6d).

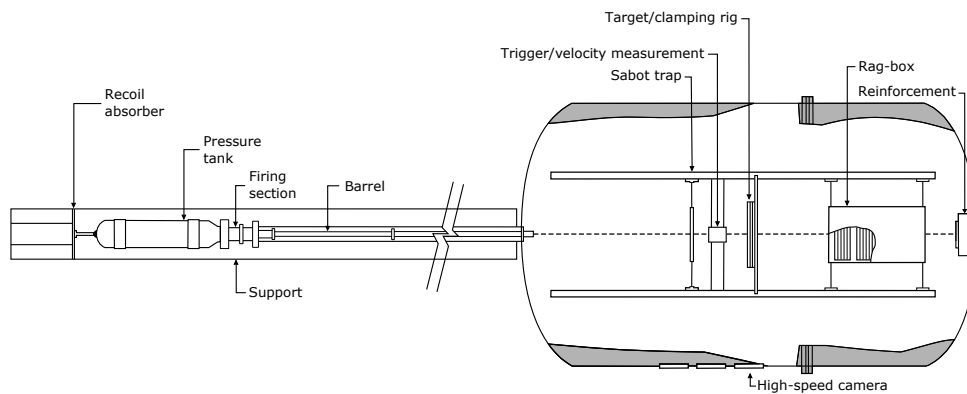
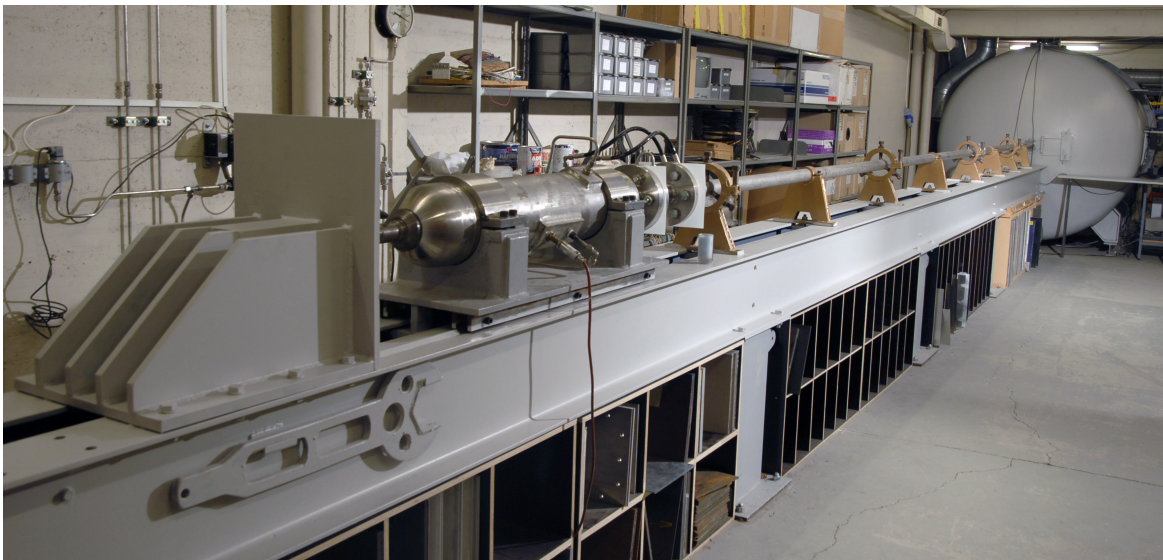
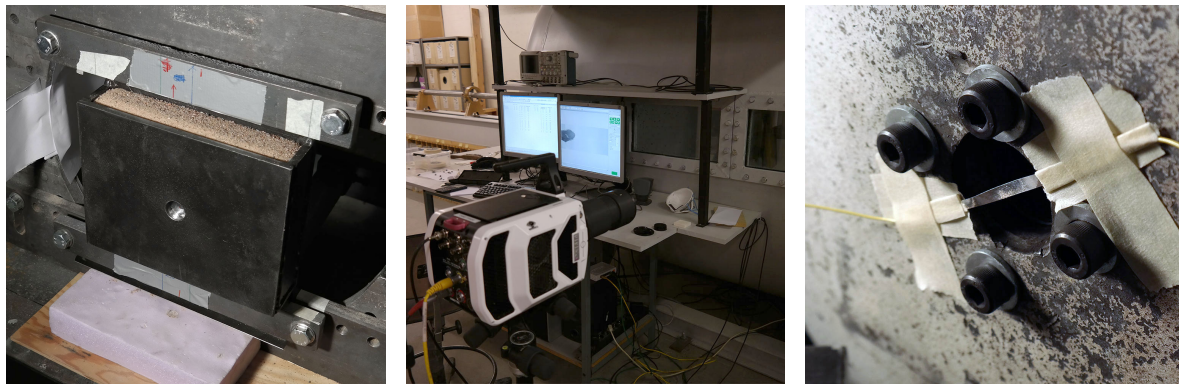


Figure 5.5: Sketch of experimental set-up.



(a) Compressed gas-gun

Figure 5.6: Continues on next page



(b) Boundary condition (c) High-speed camera (d) Camera and blitz trigger

Figure 5.6: Sand calibration gas-gun test set-up: ($v_i \approx 280$ m/s).

The firing mechanism is shown in Figure 5.7. It is a simple system where air is pumped into pressure chamber 1 and 2 (P_1 and P_2 in Figure 5.7). Mylar membranes designed to withstand a certain pressure-level are used to separate the two pressure chambers from each other and the barrel. When half the value of a desired firing pressure is reached, chamber 2 is closed before chamber 1 is filled to firing pressure. The projectile is fired by depressurizing chamber 2, overloading the mylar membranes and accelerating the projectile. In this study mylar membranes capable of delivering a firing pressure of 10 bar was used, accelerating the projectile to approximately 280 m/s.

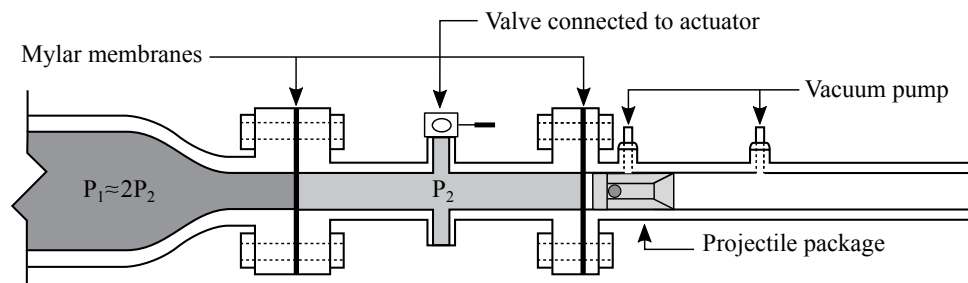


Figure 5.7: Detailed sketch of firing system for the gas-gun.

A ball-bearing ball with a diameter of 10 mm was selected as projectile. The ball is made of steel and has a Rockwell C hardness factor of 60 and a measured weight of 4.08 g. The diameter of the projectile is small compared to the 50 mm barrel diameter. To ensure that the sphere is accelerated in a proper manner and located in the center of the barrel, giving a well defined impact point, a sabot was used. This device is shown in Figure 5.8, which is a nine piece sabot with five pieces of hard plastic and four extruded polystyrene pieces. The ball is located against the hard foot piece in the center of the sabot. The sabot is removed in a sabot trap after firing, preventing the sabot from entering the camera view and the target area.

The holes in the sand container were covered with aluminium foil to prevent the sand from flowing out of the container. B95 sand were used as filling material inside the container and compressed to a dense arrangement as described in Section 4.2.2. In order to be

confident of having a fresh sample of sand at impact, the container was refilled before each shot.

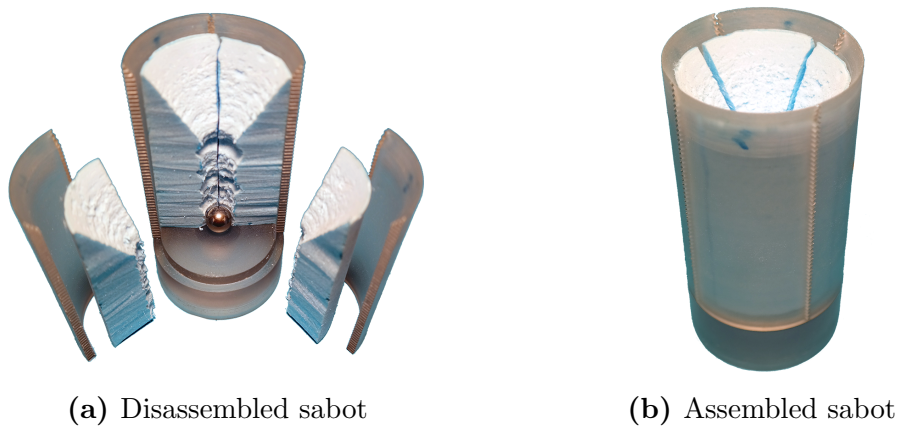


Figure 5.8: A sabot is used to center the projectile and ensure good acceleration of the projectile.

5.1.3 Results

Initial and residual velocity from the experiments can be seen in Table 5.3. These velocities are calculated from the high-speed video images, with the method described in Section 4.2.

Table 5.3: Results from compressed gas-gun material tests on B95 sand.

Test No.	Pressure (Bar)	v_i (m/s)	v_r (m/s)	Average (St.dev.) v_i (m/s)	Average (St.dev.) v_r (m/s)
1	10	277.6	57.9		
2	10	277.9	59.1	278.2 (0.8)	60.6 (3.8)
3	10	279.1	65.0		

In shot No. 1 the residual velocity is established by assuming that the projectile has the same velocity as the front part of the sand cloud, since the projectile is covered by sand and not visible. The camera angle was changed to capture the projectile as it exits the sand cloud. In shot No. 2 and 3 one can see the bullet in the front of the sand cloud, thus confirming the assumption in shot No. 1. The high-speed video images from all tests are shown in Figure 5.10. The projectile before and after the experiments is shown in Figure 5.9. One can see that the projectile surface facing the sand has been worn by the interaction with the sand. The damage is small, indicating that minimal amount of energy has been dissipated by fragmentation of the projectile, while the major dissipation seems to stem from the sand interaction.

The experiments shows consistent initial and residual velocities and will further be the basis for establishing the parameters in the rheological sand model needed in the numerical simulations.

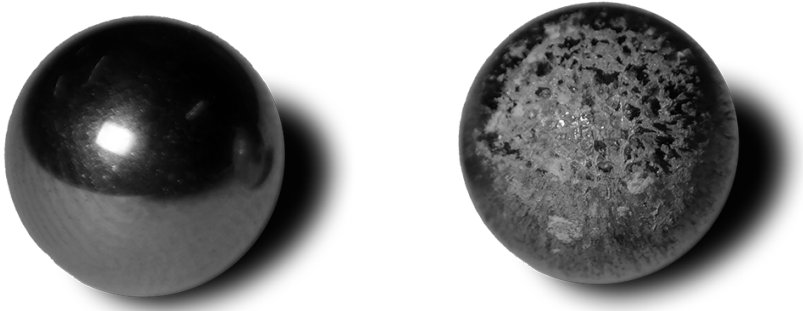
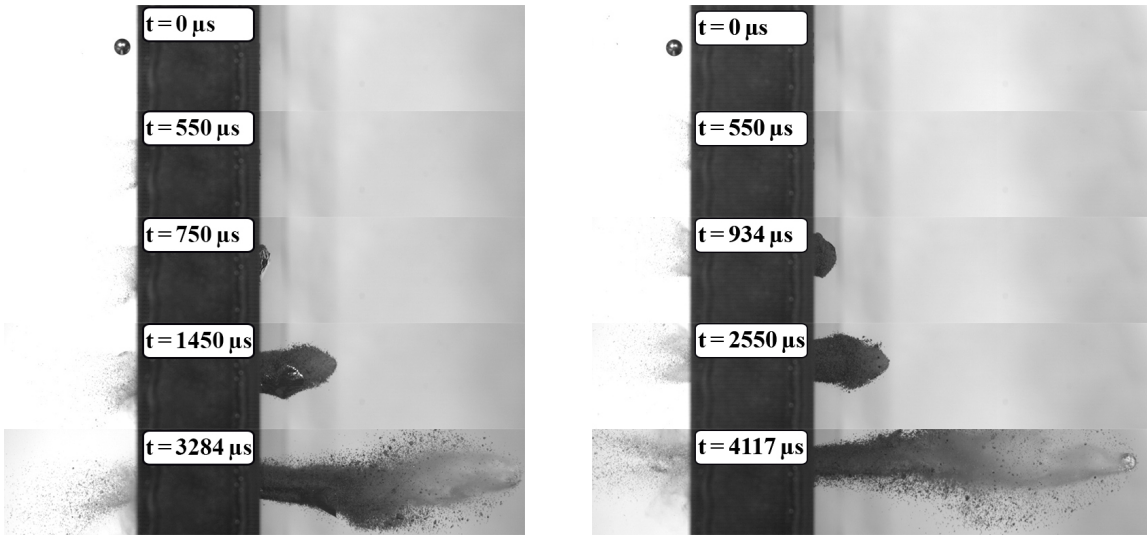
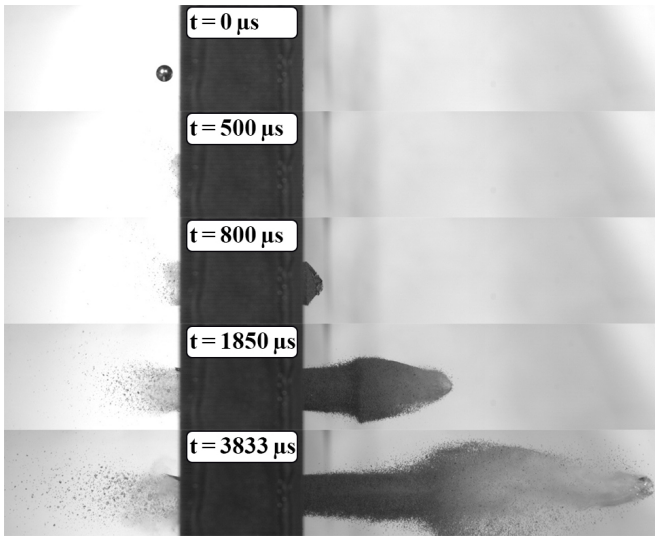


Figure 5.9: Projectile before and after sand perforation.



(a) Shot No. 1, $v_i = 277.6$ m/s and $v_r = 57.9$ m/s (b) Shot No. 2, $v_i = 277.9$ m/s and $v_r = 59.1$ m/s



(c) Shot No. 3, $v_i = 279.1$ m/s and $v_r = 65.0$ m/s

Figure 5.10: Snap-shots of sand calibration experiments.

5.2 Drop-Tower (2-10 m/s)

The test rig used in the low velocity impact tests is shown in Figure 5.11. The machine is an Instron CEAST 9350 dropped-objects-rig capable of delivering a maximum kinetic energy of 1800 J [60].

A hemispherical impactor was used with a diameter of 20 mm and without any additional mass (Figure 5.12b). This gave a total impacting mass of 5.0445 kg. Three different velocities were tested; 2 m/s, 5 m/s, and 10 m/s. An overview of the performed tests is shown in Table 5.4. The B95 sand was filled in a circular tube, which had a diameter of 12.3 cm and a height of 35.0 cm. The bottom hole of the tube was closed with a foot and the assembly was raised by underlying chipboards (Figure 5.12c and 5.12d).

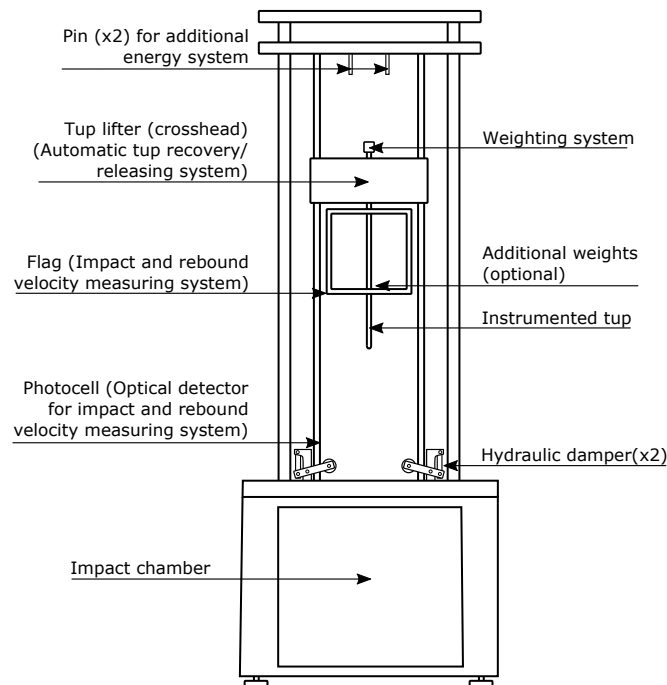
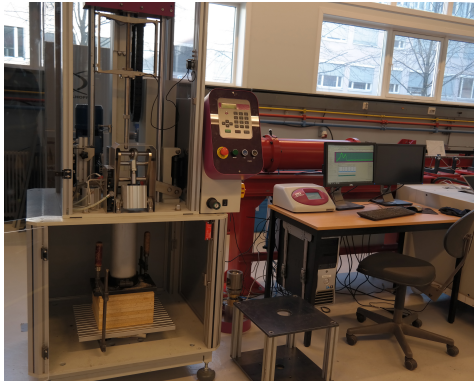
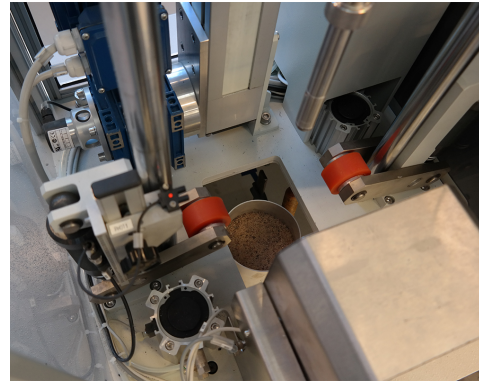


Figure 5.11: Illustration of the Instron CEAST 9350 rig.



(a) Test machine



(b) Penetrator, dampers and optical velocity measuring device



(c) Boundary condition



(d) Footing and tube filled with sand

Figure 5.12: Instron CEAST 9350 dropped-objects-rig test set-up.**Table 5.4:** Drop-tower calibration experiments, ($v_i=2$ m/s - 10 m/s).

Test No.	Drop height* (mm)	v_i (m/s)	Comment
1	204	1.67	-
2	204	1.68	-
3	204	1.68	-
4	204	1.66	-
5	1277	4.77	Hit dampers
6	1277	4.72	Hit dampers
7	1277	4.77	Hit dampers
8	1277	4.73	-
9	5099	9.82	Hit dampers
10	5099	9.78	Hit dampers
11	5099	9.86	Hit dampers
12	5099	9.80	Hit dampers

*Calculated drop height to achieve the selected speed.

5.2.1 Data Processing

The rig's load cell measured time and force with a sampling time of 0.01 ms. Initial velocity, v_i , was measured optically by the rig. Holmen et al. [60] discovered that the force measurement contains a bias. This bias was accounted for by calibrating the load cell from the first four tests where the impactor stopped before hitting the dampers. This was done by ensuring that the load cell measured the total weight when it had stopped in the sand. Acceleration was calculated by Newton's second law. Then the acceleration was numerically integrated to establish the velocity increment. The current velocity was then found by subtracting this incremental velocity from the previous velocity:

$$v_{n+1} = v_n - \left(\frac{F_{n+1} + F_n}{2m_p} - g \right) \Delta t \quad (5.1)$$

where v_{n+1} is the current velocity, v_n is the previous velocity, F_{n+1} is the current force and F_n is the previous force. m_p is the projectile mass, g is the gravitational acceleration and Δt is the sampling time. Displacement was found by integrating the velocities numerically in the same manner as for the velocity.

5.2.2 Experimental Results

Force versus displacement and velocity versus displacement curves are established for all velocities in Figure 5.13. Different initial velocities are created by adjusting the drop height, while an additional energy system are used to supply energy when the drop height is not adequate. During testing pure drop height was used to create an initial velocity of 2 m/s, while the additional energy system was used to push the penetrator in order to reach initial velocities of 5 m/s and 10 m/s. The displacement is limited by the experimental set-up, because the dampers will absorb the energy after reaching a displacement of 110 mm. This removes the load from the load cell, making the data invalid. All data after this point are excluded. The force-displacement curves are plotted with all the fluctuating force measurements, thus the noisy curves. The average of the velocity versus displacement curves for the different velocities are presented in Figure 5.14. The peaks and bottoms of the force, or likewise the inflection points for the velocity-curve, indicates a change to reduced or increased deceleration.

The tests performed with an impact velocity of 2 m/s did stop by themselves, so no effect from dampers is seen. The force-displacement curves are characterized with a gradual increase in resistance from the time of impact (Figure 5.13). This period is followed by a short reduction, before a marked abrupt rise and fall at the terminal portion of penetration. The last peak have also been observed before for both low and high impact velocity regimes [7]. As illustrated by Backman 1976 this behaviour is typical for soils, and unlike many other materials like metals and masonry [33] (Figure 2.7). The cause of this peak could be related to the transition from inertial resistance to frictional resistance as described in Chapter 2.8.2 about velocity deceleration. After the last peak, deceleration is related to a quasi-elastic rebound of soil according to Omidvar et al. [7]. The experiments

with a velocity of 5 m/s seems to hit the dampers at the terminal portion of penetration. Test No. 8 appears to be a little ahead in the process, so the last peak is measured until arrest, while the rest are stopped by the dampers just before the resistance transition peak. The curves from the 10 m/s experiments shows the gradually increasing resistance and deceleration until the main peak, where the phase of decreasing deceleration is further indicated just before the dampers are initialized.

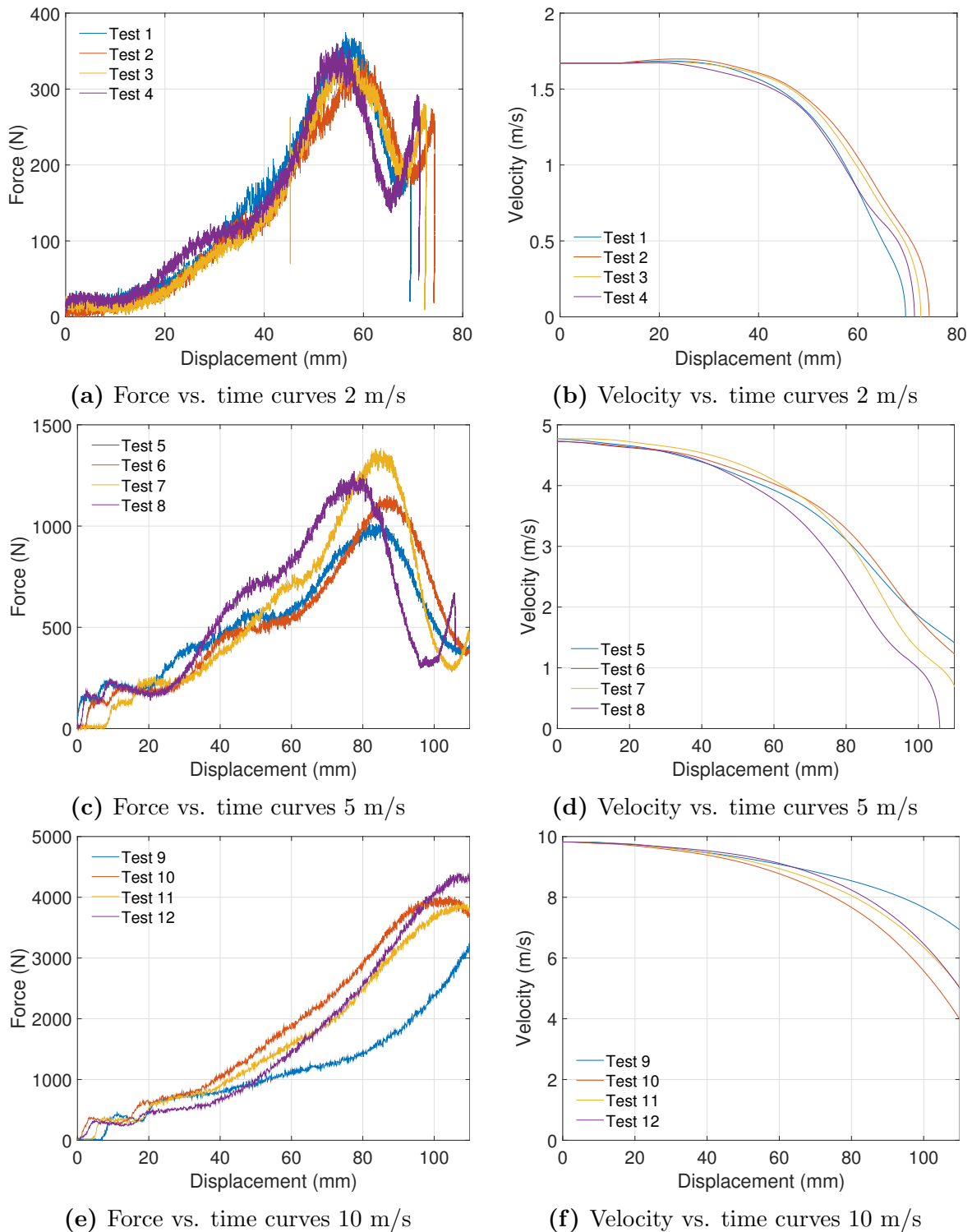


Figure 5.13: Plots showing the displacement behaviour for drop-tower tests.

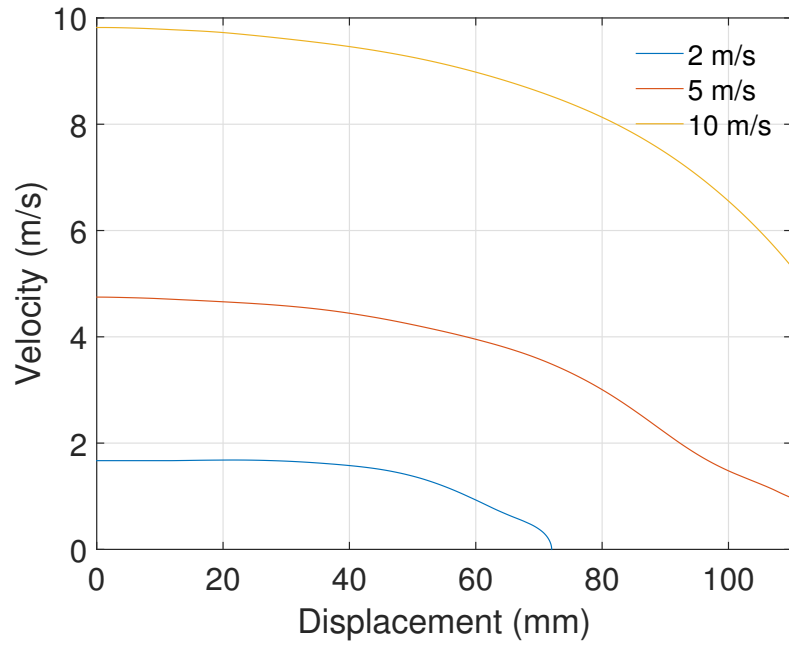


Figure 5.14: Average of each velocity from drop-tower tests.

Chapter 6

Calibration of Material Constants

In this chapter material models will be calibrated for the aluminium panel, the bullet parts and the granular material. Material parameters for the aluminium and bullet parts are taken from the literature. The parameters in the rheological model for sand will be calibrated from the component tests performed in Chapter 5.

6.1 Aluminium

Material constants for the AA6005-T6 aluminium panels are well documented in Børvik et al. [46]. In this paper the modified version of the Johnson-Cook constitutive relation and fracture model are used. In IMPETUS Afea Solver the modified Johnson-Cook fracture model is not yet included. Material constants for the fracture criterion had to be converted from a modified Johnson-Cook model to a standard Johnson-Cook model. It was decided to also convert the strain rate hardening parameter in the constitutive relation for the structural materials. This was done by minimizing the sum of squares between the MJC and the JC models.

In the constitutive relation, the second bracket of Equation 2.3 had to be replaced by the converted version in Equation 2.5 in order to get standard JC ($[1 + \dot{\epsilon}_{eq}^*]^C \rightarrow [1 + C \ln \dot{\epsilon}_{eq}^*]$). For the fracture criteria a similar operation was performed, second bracket in the MJC fracture criterion was converted into the second bracket in JC fracture criterion ($[1 + \dot{\epsilon}_{eq}^*]^{D_4} \rightarrow [1 + D_4 \ln \dot{\epsilon}_{eq}^*]$). New constants and best fits are shown on Figure 6.1 and Table 6.1.

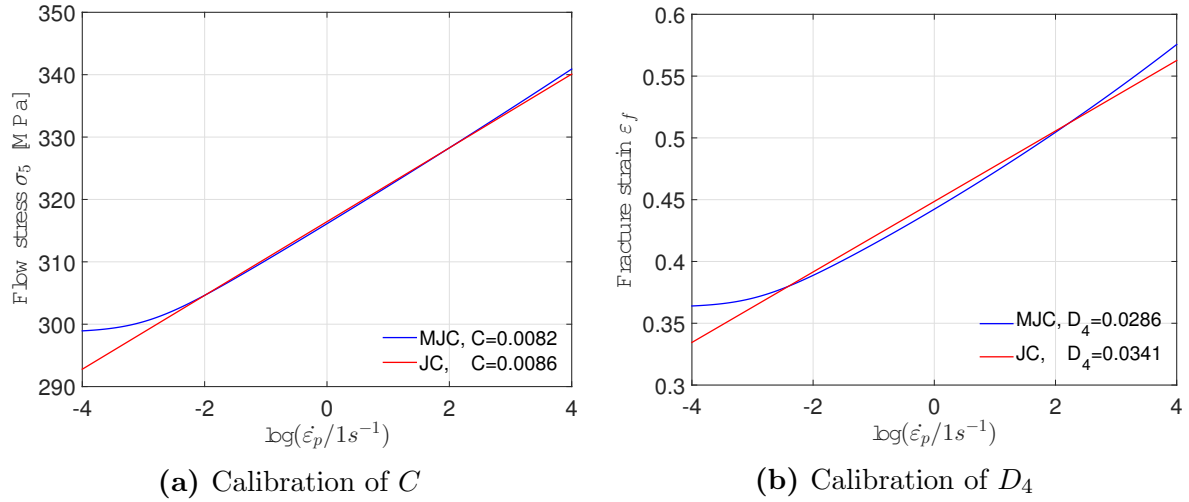


Figure 6.1: Calibration of material constants for the aluminium panel, converting from modified Johnson-Cook (MJC) to Johnson-Cook (JC).

6.2 Bullet Parts

As for the aluminium panel the literature gives material constants for a modified version of the Johnson-Cook constitutive relation for the bullet parts [61]. Therefore the same change of material models is performed for the brass jacket and lead tip, ($[1 + \dot{\epsilon}_{eq}^*]^C \rightarrow [1 + C \ln \dot{\epsilon}_{eq}^*]$). The results with material constants are given in Figure 6.2 and Table 6.1.

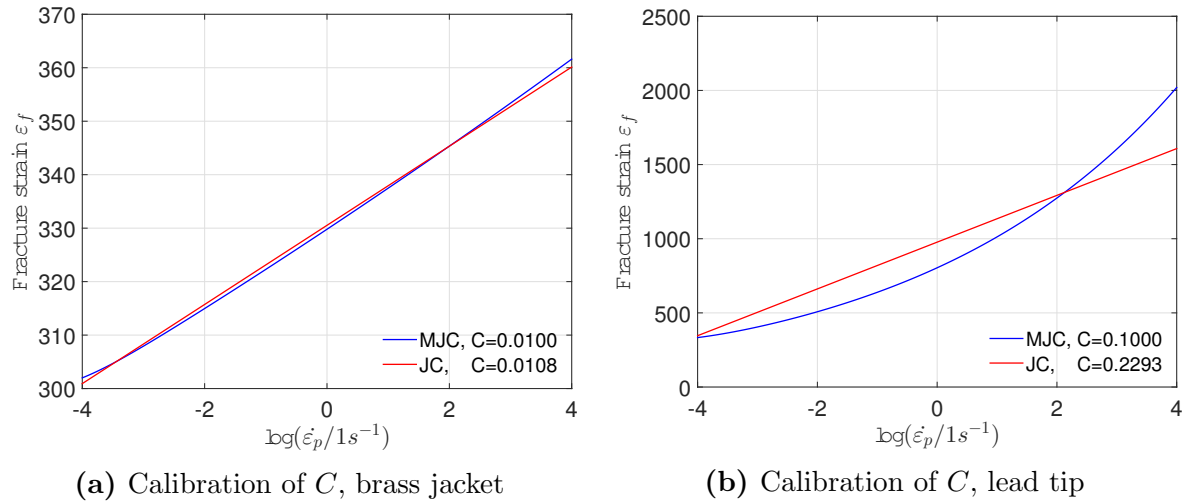


Figure 6.2: Calibration of material constants for brass jacket and lead tip, converting from modified Johnson-Cook (MJC) to Johnson-Cook (JC).

Parameters used in numerical simulations

Johnson-Cook material model and Cockcroft-Latham fracture criterion

Table 6.1: Material parameters for AA6005-T6 aluminium panel and bullet parts that will be used in the numerical investigation [46, 61].

Material/Part	General material constants				Yield A (MPa)	Strain hard.		Strain rate hard.		Temp. softening		CL W_{cr} (MPa)			
	ρ (kg/m ³)	ν	E (GPa)	C_p (J/kgK)		χ	α (K ⁻¹)	B (MPa)	n	$\dot{\epsilon}_0$ (s ⁻¹)	C (MJC) (MPa)		C (JC) (MPa)	T_r (K)	T_m (K)
AA6005-T6 panel	2700	0.3	70	910	0.9	2.3×10^{-5}	134	0.514	1.0×10^{-3}	0.0082	0.0086	293	893	0.703	-
Lead cap	10660	0.42	10	124	0.9	2.9×10^{-5}	300	1	5.0×10^{-5}	0.1	0.2293	293	760	1	175
Brass jacket	8520	0.31	115	385	0.9	1.9×10^{-5}	505	0.42	5.0×10^{-5}	0.01	0.0108	293	1189	1.68	914

Johnson-Cook fracture criteria

Table 6.2: Johnson-Cook fracture parameters AA6005-T6 aluminium panel.

Material/Part	JC				
	D_1	D_2	D_3	$D_4(MJC)$	D_5
AA6005-T6 panel	0.06	0.497	-1.551	0.0286	0.03412
					6.8

Parameters used in the sand model

Table 6.3: Sand parameters used in IMPETUS Afea Solver.

Sand grain diameter (m)	Soil packing scheme	Soil density (kg/m ³)	Contact stiffness (N/m)	Damping coefficient	Soil-soil friction	Soil-Structure friction
0.001	1000	1731.3	4.0×10^8	0.00	0.25	0.30
0.002	1000	1731.3	4.0×10^8	0.00	0.18	0.20

6.3 Sand

The calibration of material constants to the discrete particle-based module in IMPETUS Afea Solver is worked out by reproducing the experimental results from the component tests numerically. The numerical simulations are adapted to the experimental tests from the compressed gas-gun and drop-tower by tuning the parameters in the rheological sand model. One of the main objectives was to check whether a given set of parameters in the rheological model were able to adapt the sand behaviour under different velocity regimes.

The simulations were primarily conducted with the aim to mimic the test results from the sand with a median of 0.95 mm. As seen before the number of particles has a significant importance when modeling sand. Børvik et al. [5] argued that the particle size should be of the same order or somewhat larger than the median to the real sand. The parameters in the rheological model were therefore calibrated with a particle diameter of $d_s=1.0$ mm. In addition, a diameter of $d_s=2.0$ mm was tested to check for differences in numerical results.

6.3.1 Compressed Gas-Gun: Numerical Investigation

Firstly the gas-gun experiments were modelled as shown in Figure 6.3. The sand container and projectile were modelled rigid with a density of 7800 kg/m^3 and meshed using higher-order elements to allow a smooth surface. The sand was modelled using 2 750 000 particles, giving a particle diameter of $d_s=1.006$ mm. Translation of the sand container was prevented in every direction.

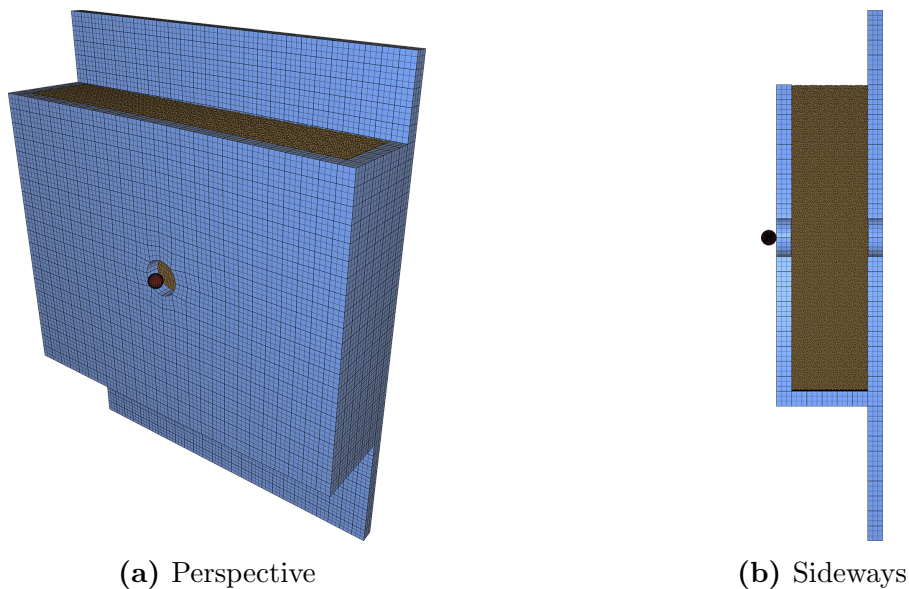


Figure 6.3: Numerical model of gas-gun tests with sand particle diameter of 1 mm.

Boundary Check

To check whether the outer boundaries have any effect on the residual velocity, the whole sand container was modelled (Figure 6.3). The boundary check was executed by applying the standard dry sand model in IMPETUS Afea Solver together with an impact velocity of 250 m/s. The velocity field from the simulations is shown in Figure 6.4. One can see that the circular distributed velocity field does not reach the outer boundaries during the perforation process.

As stated the sand-box where constructed with wrong dimension in the height, because of a mistake in the technical drawing. However, the constructed height of 200 mm did not influence the numerical results, because of initially over-dimensioning the box in the planning phase.

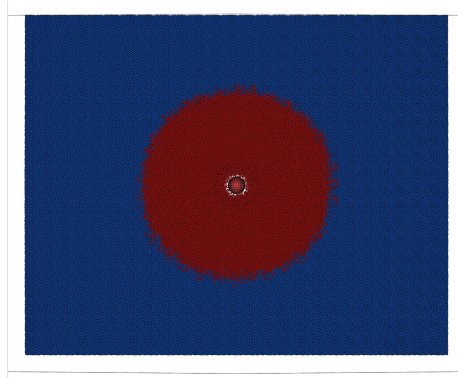


Figure 6.4: Velocity field as the projectile leaves the sand container, every part with a velocity greater than 0 m/s is marked red.

Simplification of Numerical Model

Simulations with different boundary conditions were conducted; one with the boundary conditions shown in Figure 6.3 (sand container) and the other with the boundary conditions shown in Figure 5.1 (sand cylinder). Identical input parameters were used in both models to capture any differences due to geometry. A small difference in residual velocity was revealed (Table 6.4). This may be because of small differences in particle size or particle stacking. To save computational time the calibration of material parameters was conducted using the sand cylinder model.

Table 6.4: Difference in residual velocity due to the boundary conditions.

Boundary Conditions	No. of particles	Particle diameter mm	v_r m/s	Difference %
Sand container	2 750 000	1.006	102.6	-
Sand cylinder	2 750 000	1.038	101.5	-1.07

The energy balances for the sand container and sand cylinder analysis are presented in Figure 6.5. The energy balance gain was less than 1.0%, which is within the selected limit of 5% (Section 2.7). It is seen that the energy balance is nearly identical for the two different boundary conditions. The projectile's kinetic energy is mainly transferred through dissipation by interaction of sand grains and acceleration of sand particles. Sand particles and their energy are removed when they are fluxing out of a specified area.

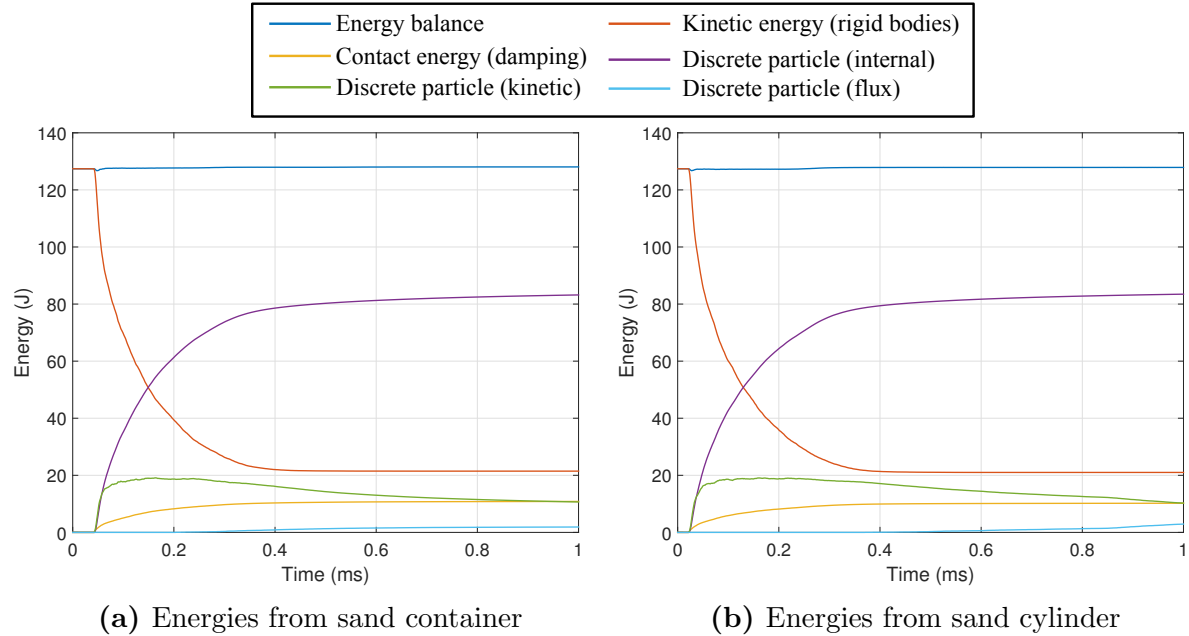


Figure 6.5: Energy balance from sand container and sand cylinder analysis, with $v_i=250$ m/s and dry sand model in IMPETUS Afea Solver.

Parameters in the Rheological Model

Through several numerical simulations, the soil-soil friction and soil-structure friction were calibrated for particle diameters of 1.0 mm and 2.0 mm. Initial velocity in all simulations was set to the average of the three experimental tests, $v_i=278.2$ m/s. The friction parameters were varied with the objective to hit the average of the residual velocity from the same tests, $v_r=60.6$ m/s. The best fit for each particle diameter is given in Table 6.5. A larger particle diameter means that the projectile has to accelerate a greater part of the total sand mass. To account for this, the soil-soil friction and soil-structure friction are reduced.

Table 6.5: Calibration of parameters in sand model.

	Particle size (mm)	Soil-soil friction	Soil-structure friction	v_r (m/s)	Difference (%)
Experiment (avg.)	-	-	-	60.6	-
Numerical	1.006	0.25	0.30	60.75	0.24
Numerical	2.000	0.18	0.20	60.58	-0.04

A comparison between the high-speed video images from a gas-gun experiment and the numerical analysis is shown in Figure 6.6. Excellent qualitative agreement is obtained, which shows the strength of the discrete particle module. Note that the pictures are adjusted such that the sand thickness of 50 mm is in the same scale for both the experimental and numerical representation.

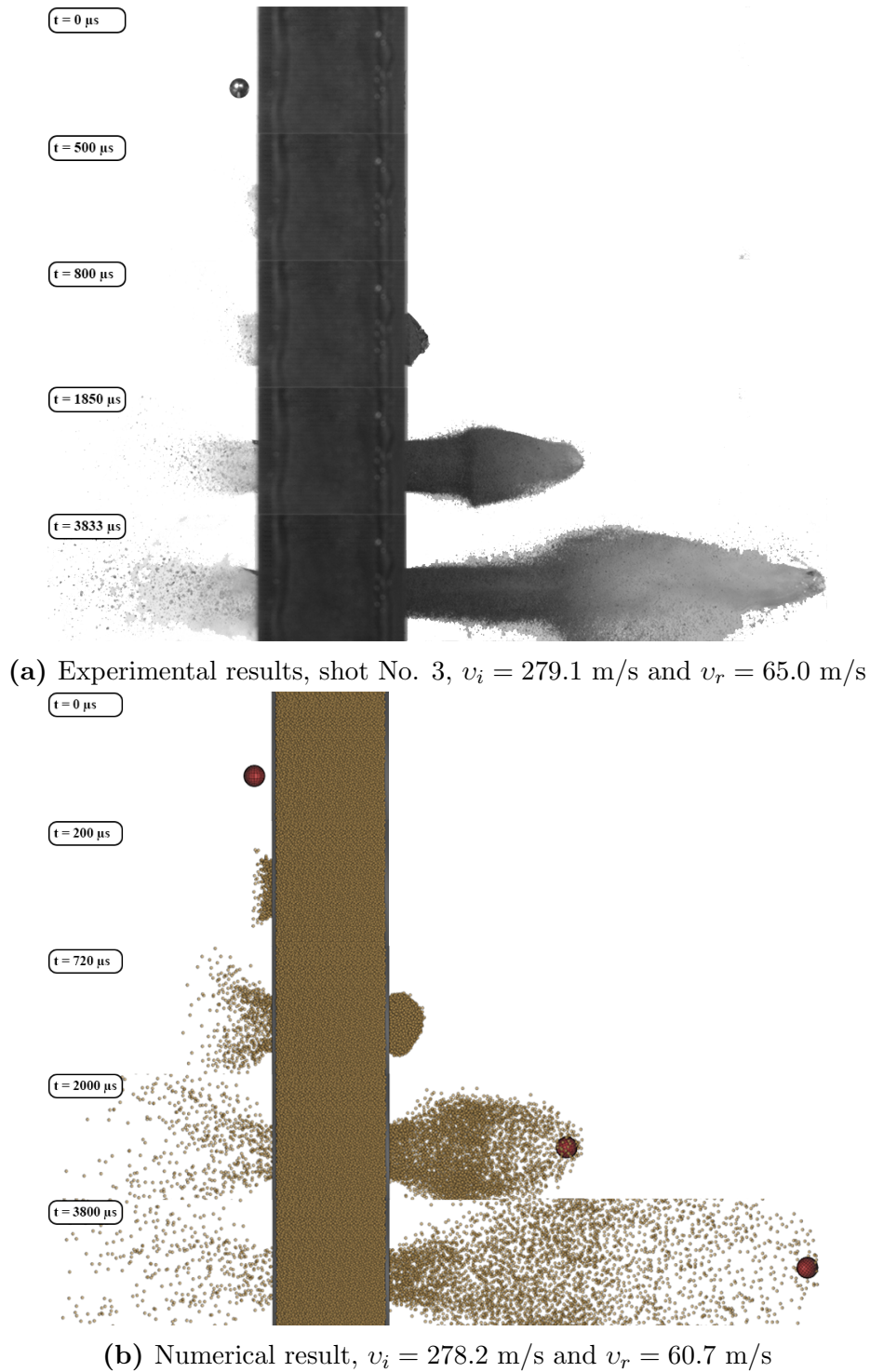


Figure 6.6: Comparison between (a) experimental result and (b) numerical output.

6.3.2 Drop-Tower: Numerical Investigation

The drop-tower component tests from Section 5.2 were reproduced numerically with the IMPETUS Afea Solver. The cylinder and footing containing the sand were modelled together with the impactor. In order to reduce the number of elements needed in the model, the impactor was modelled as hollow with a wall thickness of 2 mm. All structural parts were assumed rigid with a density equivalent to a mass of 5.0445 kg for the impactor, which was the given mass from the test machine. Impact velocities of 2 m/s, 5 m/s and 10 m/s were investigated. Gravity was also introduced since impact was driven in the gravity direction at fairly low velocities. The final model is presented in Figure 6.7.

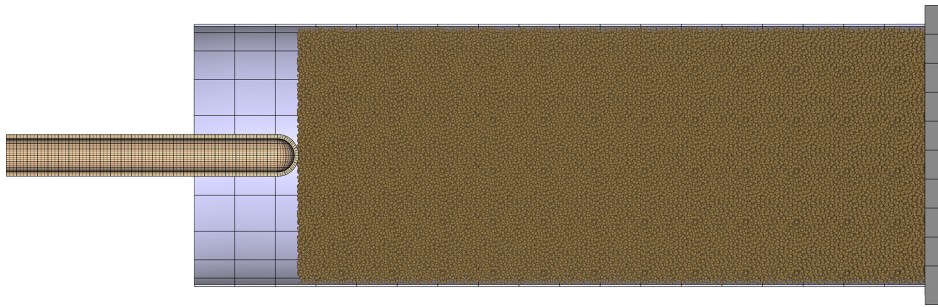


Figure 6.7: Numerical model of drop-tower component test with a sand particle diameter of 1 mm.

In contrast to the high velocity tests, these experiments in the low-velocity regime required a long time duration in the numerical simulations. The analysis with initial velocity of 2 m/s had a total simulation time of 301 hours from the time the impactor touched the sand to the termination time of 0.2 s, with the result of almost stopping.

It quickly turned out that the resistance in the sand at these velocities was hard to recreate with the calibrated parameters. The deceleration of the impactor was minimal as the penetration proceeded through the sand. An initial velocity of 10 m/s gave only a reduction to 9.97 m/s at a displacement of 110 mm, which in the experimental testing was shown to be from 4 m/s to 7 m/s. Simulations carried out without gravity included gave insignificant change in deceleration. A further view of the velocity field from the numerical analysis can be studied in Figure 6.8.

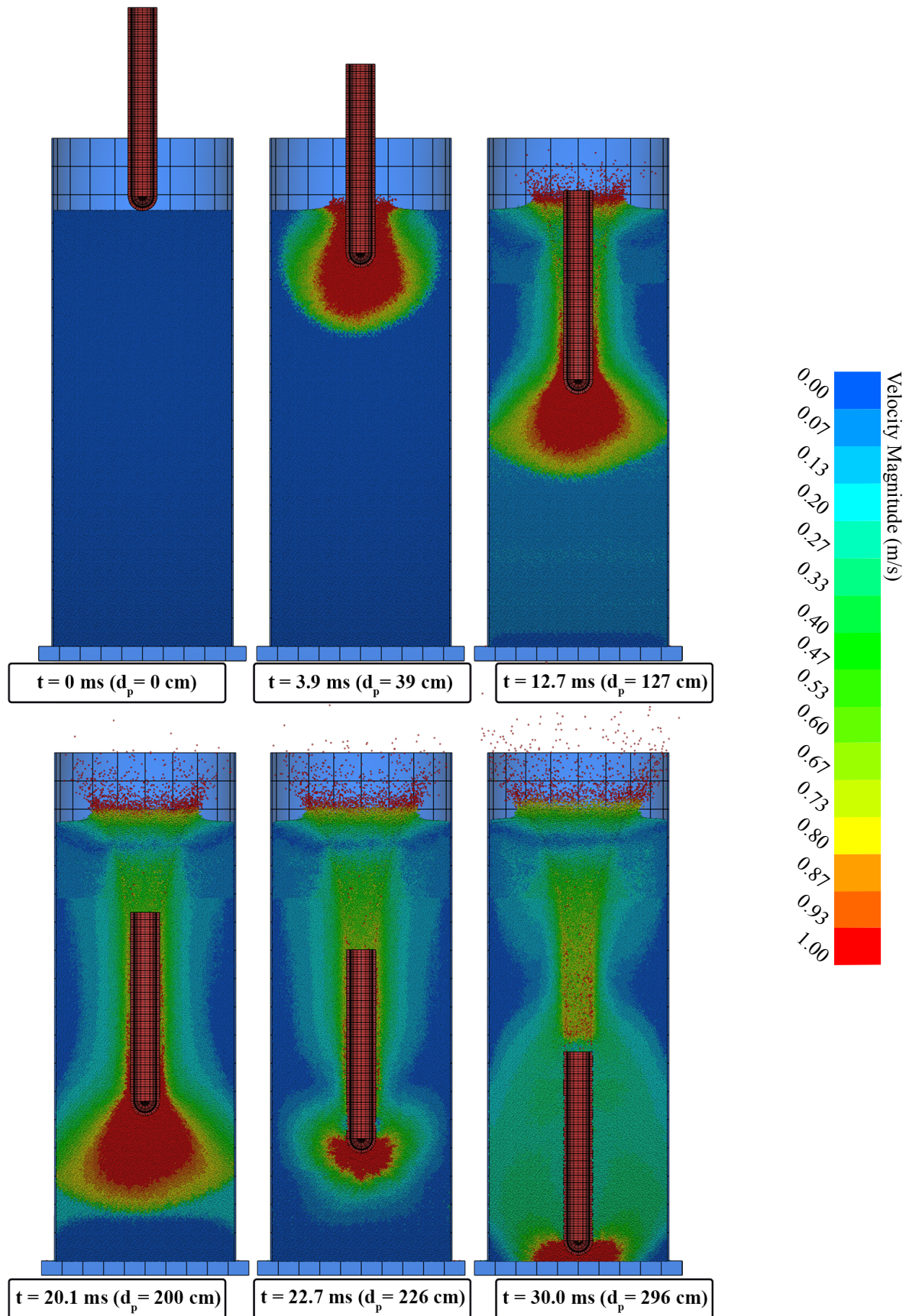


Figure 6.8: Drop-tower time-lapse, showing the velocity field for simulation with $v_i=10$ m/s.

The main observations from the penetration process are: The sand particles are immediately set in motion as the impactor hits the sand field. The particles are pushed into a denser arrangement in front of the impactor, producing very little resistance, which is evident from the force-displacement curve in Figure 6.9b. As the particles are pushed down by the impactor, a fully compacted region of sand at the bottom builds up. This area is seen from the velocity field in frame 3-4 in Figure 6.8, marked with the dark blue color, hence 0 m/s in velocity. This region of compacted particles keeps increasing in extent, giving the increasing resistance effect seen from approximately 200 mm penetration depth (Figure 6.9b). However, this resistance is not enough to stop the impactor from reaching the bottom plate (Figure 6.9).

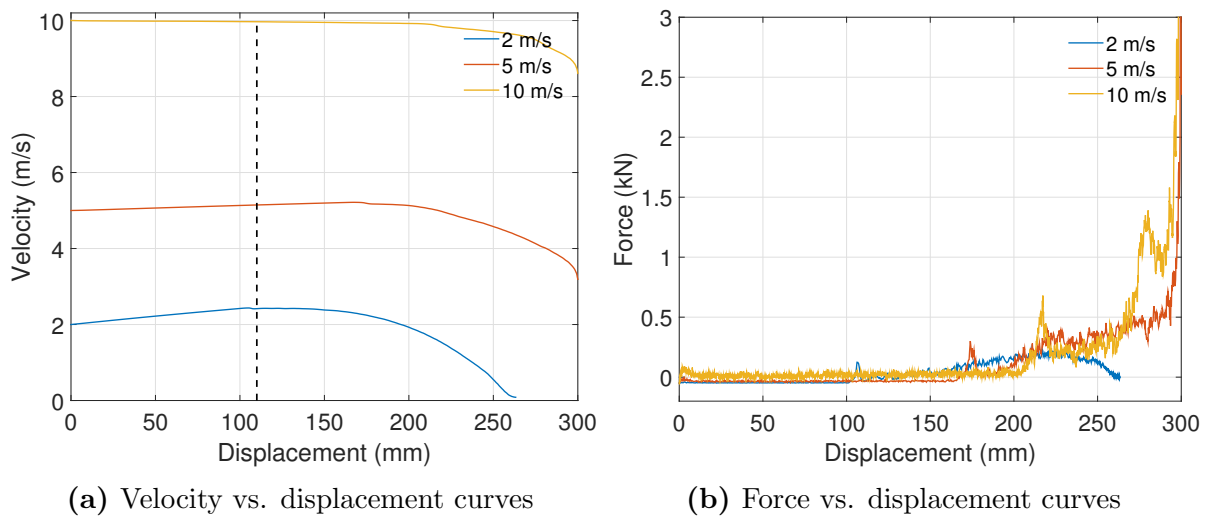


Figure 6.9: Results from impactor simulations.

A large number of values regarding the soil-soil friction and soil-structure friction were tested, in addition to a range of particle numbers from 250 000 ($d_s=2.54$ mm) to 4 000 000 ($d_s=1.00$ mm). The effect of particle size is shown to give less resistance, the smaller particles, something that is further discussed in Chapter 8.3. None of the parameters regarding the soil seemed to give any noticeable reduction in velocity in the numerical simulations. In addition, simulations with a top plate causing a closed cylinder were also tested in order to check the effect of splashing sand, but no particular change was found.

The resistance of the particles was further checked by changing the geometry of the impactor. First a sphere impactor showed to the right in Figure 6.10 with a diameter of 40 mm and the same mass was tested to check if the projectile size had any effect on the resistance in the particle model. The velocity reduction at a penetration depth of 110 mm for the sphere projectile changed one order in magnitude closer than the original impactor. This would probably be far from well-adapted when thinking about an experimental test with the same geometry. Lastly, an initial velocity of 100 m/s was put on both the sphere and original impactor for comparison in velocity regimes. In terms of percentage the reduction was approximately the same for initial velocities of 10 m/s and 100 m/s, as seen in Table 6.6.

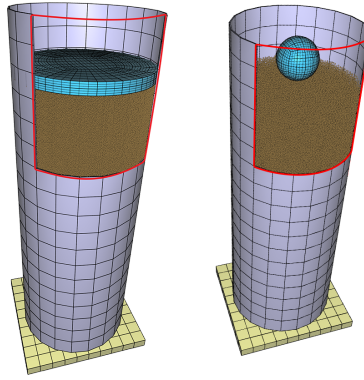


Figure 6.10: Perspective view of the model with sphere impactor (right) and the circular plate (left).

Table 6.6: Results from different drop-tower simulations. Showing v_r at a penetration depth of 110 mm (the displacement where the experiments hit the dampers) and 300 mm (the bottom of the sand cylinder). In addition calculated difference from initial velocities for each step.

	Impactor				Sphere impactor	
	2	5	10	100	10	100
v_i (m/s)						
v_r at 110 mm (m/s)	2.42	5.15	9.97	98.63	9.36	92.62
Difference (%)	20.89	2.93	-0.32	-1.37	-6.39	-7.38
v_r at 300 mm (m/s)	0.09*	3.20	8.60	94.18		65.38
Difference (%)	-95.7*	-36.02	-13.95	-5.82		-34.62

From a displacement of 26.3 cm.

These observations lead to another numerical analysis where the compression of the sand particles stayed in focus. The same model was adopted, but a circular plate covering whole the sand field replaced the impactor. The model is shown to the left in Figure 6.10. The plate was only in contact with the particles, so no friction to the pipe walls was present. Initial velocities of 2 m/s, 5 m/s and 10 m/s were investigated to check the resistance effect from the sand particles. This resembles a confined compression test where the pressure is a function of the initial velocity. The velocity-displacement and force-displacement curves shown in Figure 6.11 shows that all three different velocities stop at roughly the same depth. This clearly shows that resistance from the particles is minimal at these low velocities until they are affected by boundaries. The velocity field from the simulation with initial velocity of 2 m/s verifies this (Figure 6.12).

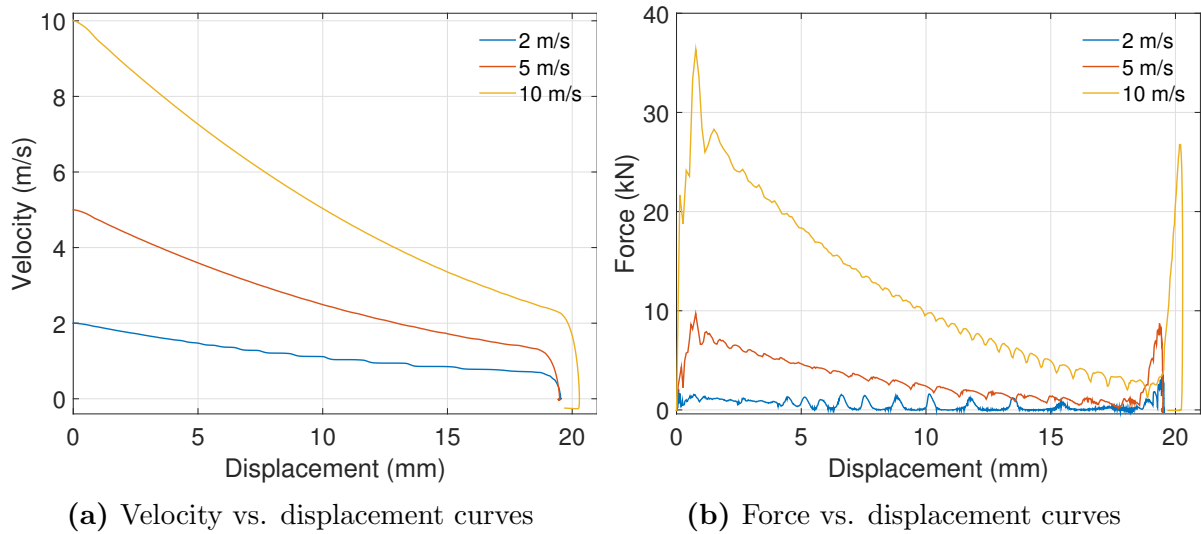


Figure 6.11: Results from circular plate simulations.

6.3.3 Discussion

The preceding simulations were performed to calibrate the parameters of the discrete particle module in IMPETUS Afea Solver. The tuned-in simulations from the gas-gun showed excellent representation of the conducted experiments, both qualitatively and quantitatively. When converting these parameters to the low-velocity regime in the drop-tower component experiments, minimal resistance from the particles is generated regardless of re-tuning the particle module parameters. At such low velocities the particles just flow in front of, or aside from the impactor without providing any resistance. These results may be evidence to that the model does not manage to represent the strain-rate sensitivity. The sand parameter tuning from the gas-gun simulations is used as calibration for the numerical part about the sand-filled panels.

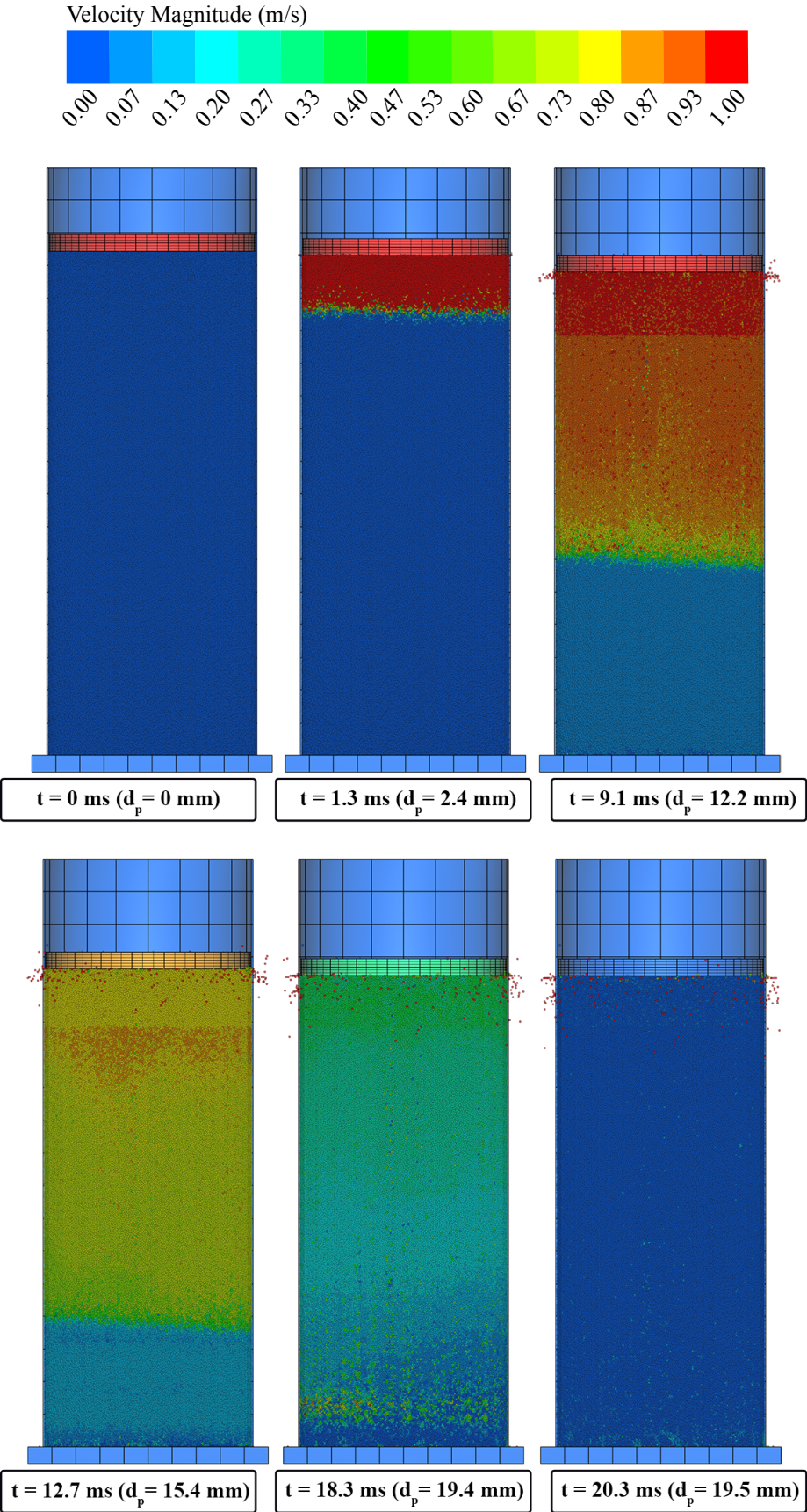


Figure 6.12: Pressure plate time-lapse, showing the velocity field for simulation with $v_i=2$ m/s.

Chapter 7

Numerical Simulations

In this chapter numerical base models for empty and sand-filled aluminium panels are established, and the numerical results are presented. The influence of angle of attack and the plate thickness are also studied in this chapter. A more thorough parameter study is later presented in Chapter 8. The finite element code IMPETUS Afea Solver was used in all numerical simulations which were executed on a computer with specifications given in Table 7.1.

Table 7.1: Computer specifications.

Component	Description	Quantity
Memory(RAM)	SM Hynix 4 GB DDR3-1866MHz	4
CPU	Intel Xeon E5 Quad-Core, 3.70 GHz 10 MB cache	1
GPU	Nvidia GPU Tesla Kepler K20C, 5 GB GDDR5 w/2496 cores	2
Motherboard	PNY Quadro NVS 300 512 MB DDR3	1

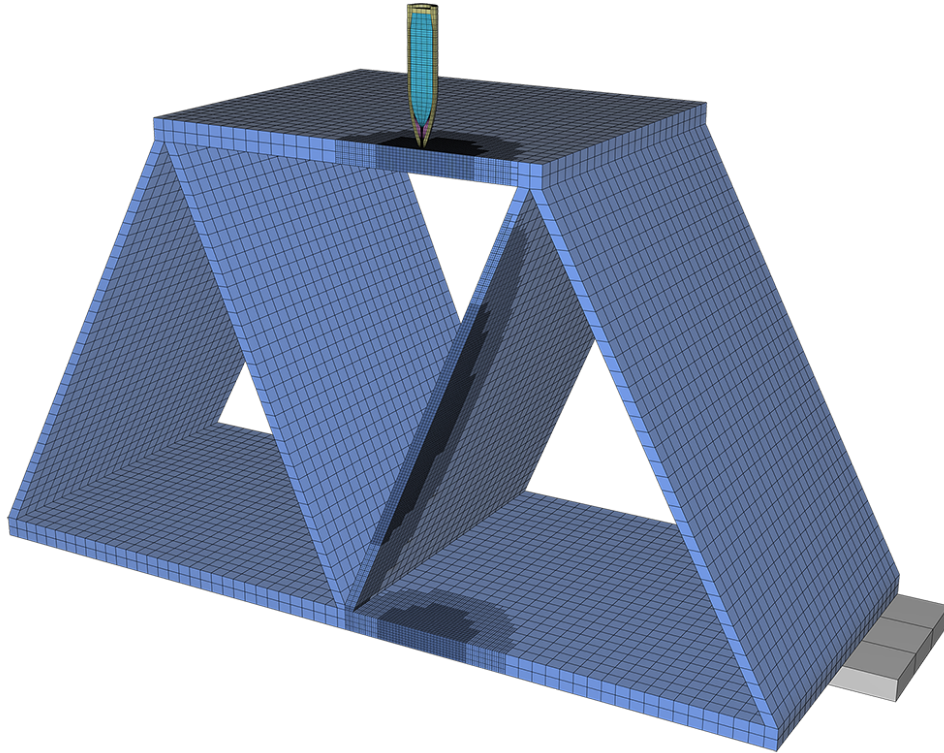
7.1 Empty AA6005-T6 Aluminium Panel

7.1.1 Numerical Base Model

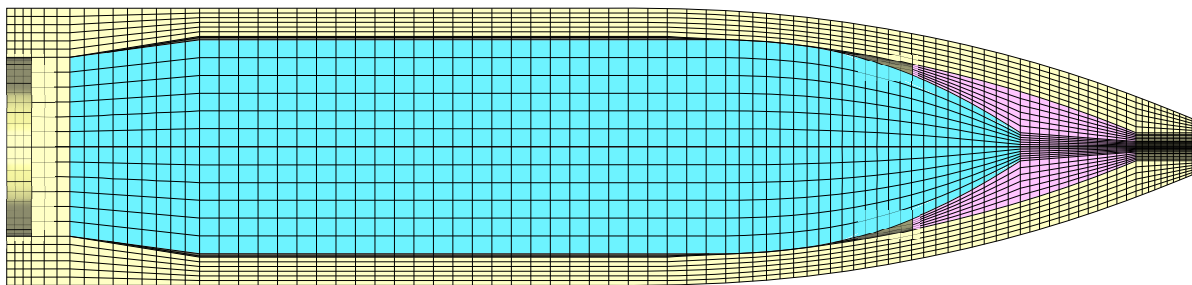
The base model for empty panels includes an aluminium panel and the full bullet. The panel was modelled with a length of 200 mm, front and rear plates with a thickness of 6 mm and four slanting webs with a thickness of 3 mm. It was decided to create the model without the use of symmetry lines. This is most important in the simulation of the sand-filled panels where the particles are placed in anisotropic unit cells such that the projectile path may turn in any direction. The model is shown in Figure 7.1.

The aluminium panel, lead tip and brass jacket materials were modelled using the Johnson-Cook constitutive relation. The material is idealized to have isotropic material properties. Fracture was modelled with different criteria; for the panels a Johnson-Cook failure criterion was used, while a criterion proposed by Cockcroft-Latham was employed for the lead

tip and brass jacket (Section 2.6.1). High-speed video images from experiments showed little or no damage in the APM2 steel core, thus the steel core was modelled as rigid. Material constants for the constitutive relation and fracture criterion can be found in Table 6.1 and 6.2.



(a) Numerical base model with mesh, cut in half for visualization



(b) Mesh used for the APM2 bullet

Figure 7.1: Numerical model (a) shows aluminium panel cut in half. Note the refined impact zone and boundary plate. In (b) a magnified view of the bullet mesh provided by our supervisors.

The panel was meshed using an approximate element size of $4 \times 4 \times 3$ mm, while the elements in the impact area were refined in two steps. The first step refined elements to $2 \times 2 \times 1.5$ mm within a 25 mm radius from the impact point. The second refinement was for elements within a radius of 15 mm giving an element size of $1 \times 1 \times 0.75$ mm in the area undergoing large deformations. Linear 8-node elements were used in the peripheral parts of the panel, while the whole bullet and all panel elements inside the first refinement were

modelled with higher-order 64-node cubic elements. Boundary conditions were applied by modelling two supporting plates at the panel's rear face. These plates were assumed rigid and constrained in every direction, preventing the panel from moving in the impact direction. A penalty based contact algorithm with a penalty number of 1.0×10^{15} [62] and a Coulomb friction coefficient of 0.01 were used to model contact.

Element damage is treated in different ways:

AA6005-T6 aluminium panel:

1. The erode 0-flag removes the deviatoric stresses in integration points once the JC failure criterion are reached, $D \geq 1$.
2. In the JC material model the yield strength drops to zero when the melting temperature is reached (893 °C for the AA6005-T6 panel).
3. Elements are removed from the analysis when their time step drops below a user defined critical time step in the IMPETUS Afea Solver. In this thesis chosen to $\Delta t_{cr} = 2$ ns.

Lead tip and brass jacket:

1. The erode 1-flag removes the deviatoric stresses in integration points once the CL failure criterion is reached, $D \geq 1$. When 16 of 64 integration points for the 64-node cubic hexahedron element reach failure, all stresses in the element are removed for the whole element.
2. In the JC material model the yield strength drops to zero when the melting temperature is reached (760 °C for the lead tip and 1189 °C for the brass jacket).
3. Elements are removed from the analysis when their time step drops below a user defined critical time step in the IMPETUS Afea Solver. In this thesis chosen to $\Delta t_{cr} = 2$ ns.

The high-speed video images from the experiments revealed that the projectile occasionally impacted the panel with an oblique angle. Analyses with an oblique impact angle were therefore conducted to see if any major effect on the residual velocity could be found. The oblique angle, α , was set to ± 3 degrees, with the angle definition in Figure 7.2. In addition simulations with different front and rear plate thicknesses were conducted to capture any differences in bullet trajectory and residual velocity.

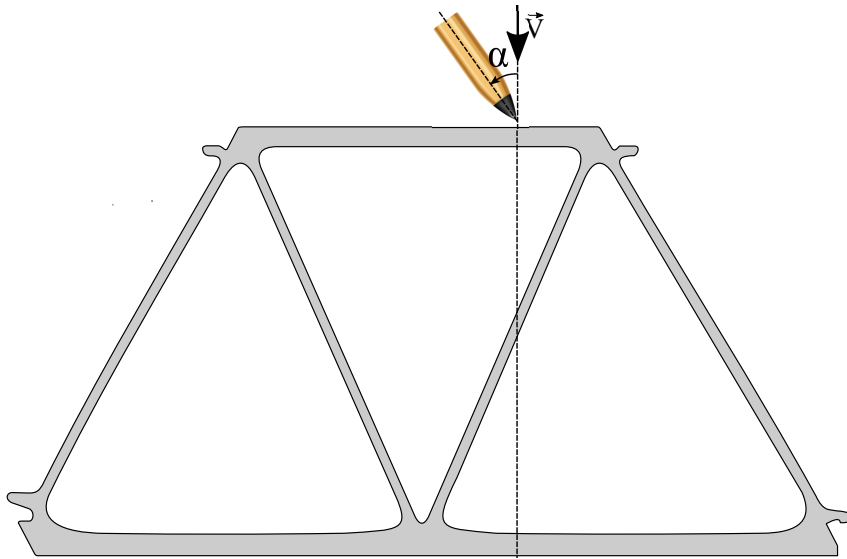


Figure 7.2: Definition of bullet oblique angle onto target.

7.1.2 Numerical Results

Numerical simulations with different initial velocities have been performed to establish the ballistic limit curve numerically. Time-lapses from base model simulations with initial velocities of 900 m/s and 450 m/s are shown in Figure 7.3. No fragmentation is seen from the front plate, but some elements in the impact zone are eroded due to their critical time step, which drops below the specified value of 2 ns. After a free-flying phase the projectile impacts the slanting web, accelerating the first elements leading to fragmentation in the web. This is also seen in the experimental work (Figure 4.9). The web has an effect on the projectile's trajectory, especially when the initial velocity is low. With an initial velocity around or below the ballistic limit, the bullet turns 90 degrees inside the panel. This was also observed in the ballistic experiments in shot No. 8 for the empty panel. Perforation of the rear plate proceeds in very much the same manner as for the front plate, with the exception of bullet impact angle. IMPETUS Afea does not capture the jacket peeling process exactly. In all simulations the jacket perforates all three plates in the panel, although some elements in the jacket are eroded. The lead tip is usually eroded early in the perforation process.

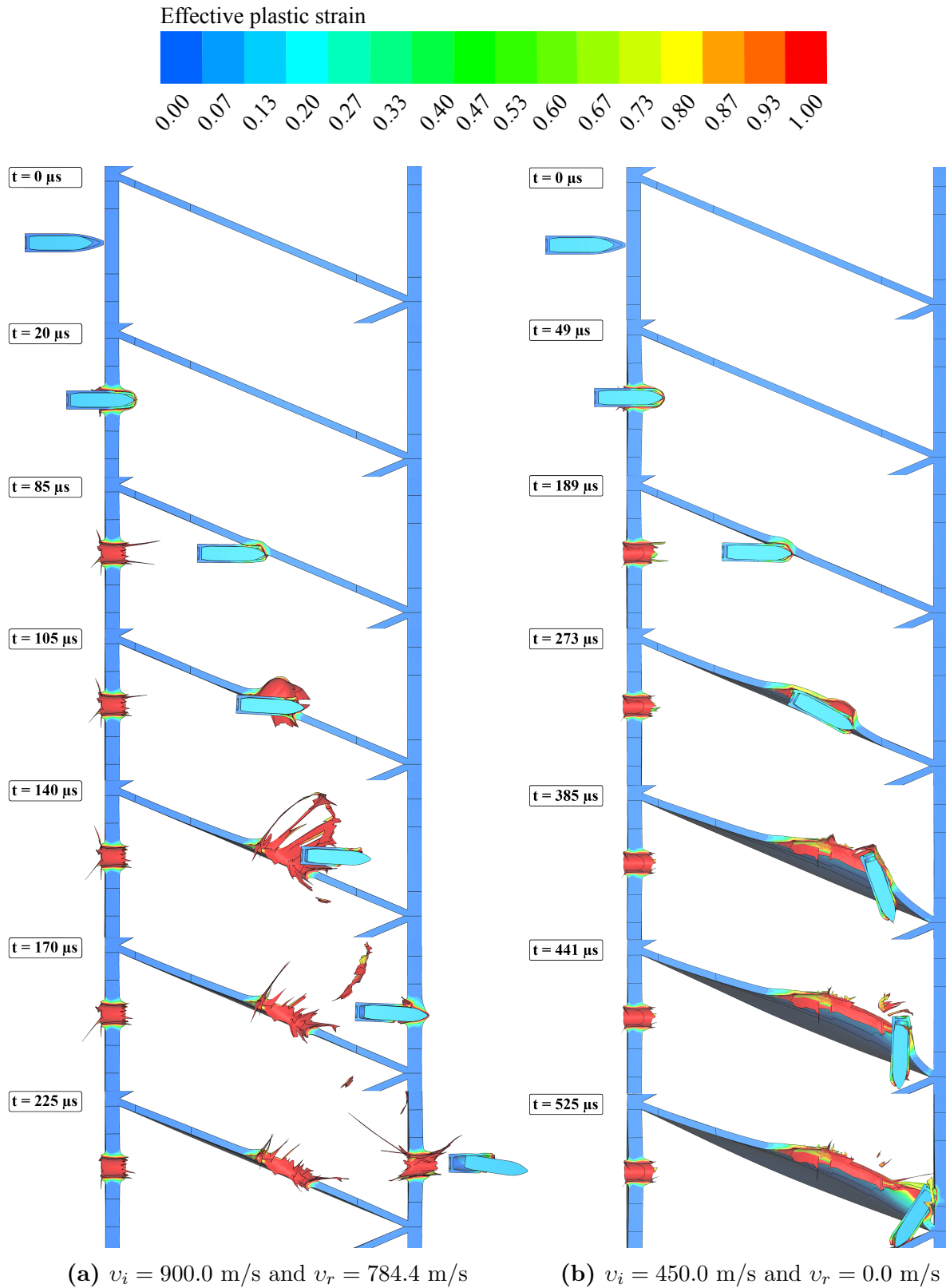


Figure 7.3: Time-lapses showing the evaluation of effective plastic strain for the base model without sand.

The Recht-Ipson model is used to estimate ballistic limit velocities and trend lines from the numerical data. The Recht-Ipson parameters used to establish the ballistic limit curves shown in Figure 7.4 are displayed in Table 7.2 together with deviations from the experimental results and the base model. The base model ($\alpha = 0$) is conservative for initial velocities greater than 550 m/s, but in the end overestimates the ballistic limit by 10.8 %.

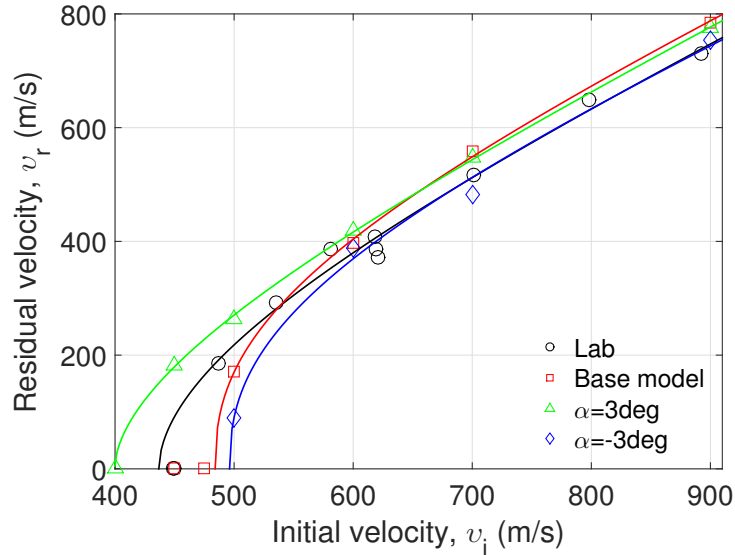


Figure 7.4: Ballistic curves from experiments, numerical base model and different initial oblique angles.

Table 7.2: Recht-Ipson parameters for experiments and numerical investigated scenarios of empty panels.

Scenario	a	p	v_{bl} (m/s)	Deviation from experiment (%)	Deviation from base model (%)
Experiment	0.98	1.86	436.7	-	-9.8
Base model	0.97	2.46	484.1	10.8	-
$\alpha = +3deg.$	1.00	1.80	399.6	-8.5	-17.4
$\alpha = -3deg.$	0.92	2.45	496.2	13.6	2.5
Thick front plate	0.94	2.85	499.7	14.4	3.2
Thick rear plate	0.95	2.37	449.1	2.8	-7.2

A closer inspection of the penetration process is done for elements near the bullet path marked in Figure 7.5. Damage and temperature values from the two elements are compared with each other in Figure 7.6. Element 30 706 reached the JC fracture criterion and failure occurred in the element, while the other element never reached this criterion. Temperature is higher closer to the impact point.

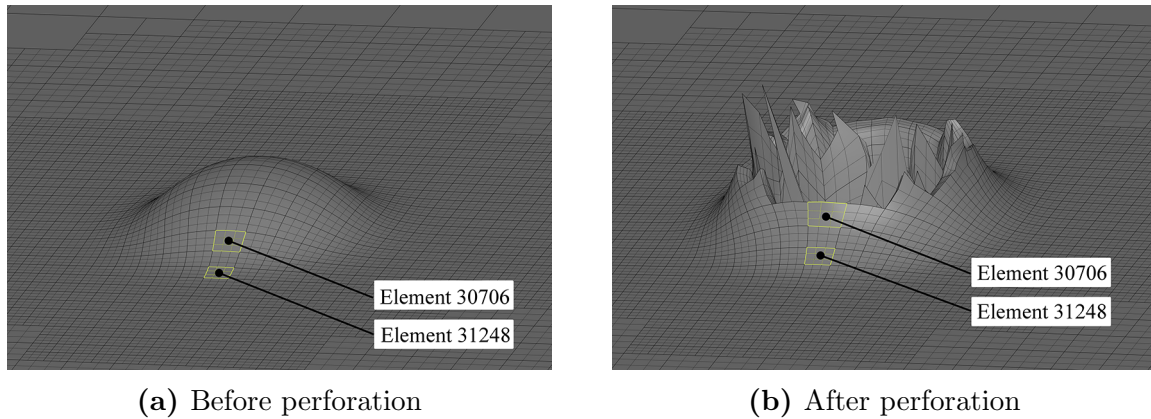


Figure 7.5: Picture of the two selected elements before and after perforation, $v_i=900$ m/s and $v_r=784.4$ m/s.

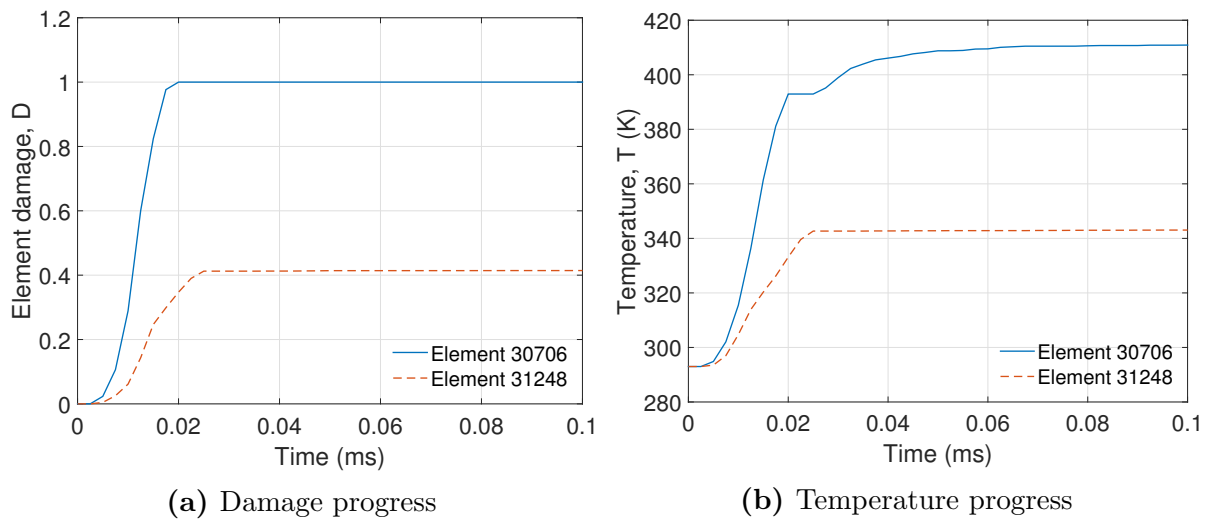


Figure 7.6: Evaluation of damage and temperature in the selected elements.

Oblique Impact Angles

The slanting web has a big effect on the bullet's trajectory and subsequently the angle with which the bullet impacts the rear plate. An overview of the bullet rotation versus displacement is shown in Figure 7.7 for initial velocities of 900 m/s, 700 m/s and 500 m/s. The web's increasing effect on the bullets further trajectory is seen clearly. To counteract this effect the bullet was given an initial angle of $\alpha = +3^\circ$. This causes the bullet to hit the rear plate with less obliquity, resulting in an increased residual velocity. The ballistic curve becomes conservative for all initial velocities, with a underestimation of the ballistic limit velocity by -8.5% from the ballistic experiments. A decrease of 17.4% is also observed from base model. The bullet was also tilted in the opposite direction by three degrees ($\alpha = -3^\circ$). As expected the ballistic limit velocity increased, but only by 2.5% compared with the base model. This increased the deviation from the experimental results to 13.6% .

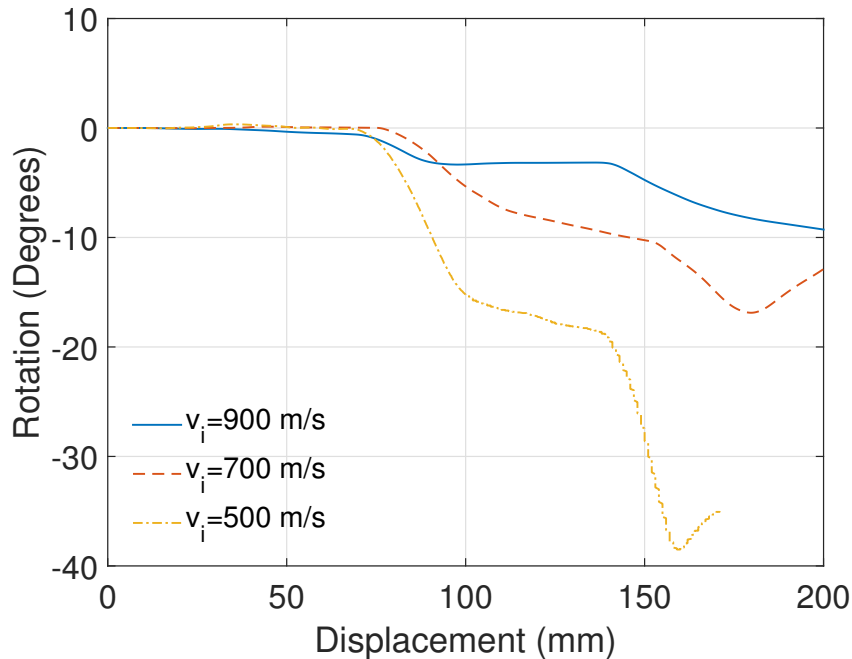


Figure 7.7: Rotation of the bullet as the bullet moves through the panel.

The difference in ballistic limit velocity between the two opposite angled bullets appears to originate from the interactions with the slanting web and the following perforation of the rear plate. When impacting the slanting web with a larger oblique, the perforation process becomes more cumbersome due to increased effective plate thickness. This may be the reason for the difference in residual velocity for the model at high initial velocities. The slanting web will in addition initiate rotation especially for low impact velocities, which leads to a lower residual velocity. At lower initial velocities the slanting web will initiate additionally rotation of the bullet, which affects the larger oblique angles to a greater extent. Increased rotation results in a larger impact angle with the rear plate, leading to a lower residual velocity. This explains the gradually increasing gap at lower velocities between the two ballistic curves. The reason why the base model curve is located over both the two curves with initial oblique angle at high velocities, may be because the velocity vector that is defined normal to the front plate in all situations gives less resistance when zero oblique is introduced.

Front and Rear Plate Thickness Variation

Based on the measured plate thicknesses presented in Table 3.2, new panel meshes were made with varying front and rear plate thickness. The front and rear plate thickness were set to 6.5 mm and 5.5 mm and vice versa, called thick front and thick rear respectively. The results are shown in Figure 7.8. Even though the total plate thickness is the same in all simulations, considerable changes are seen in the residual velocity. This is due to the increased effect the web has on the bullet's trajectory for reduced velocities. Figure 7.9 clearly shows this phenomenon.

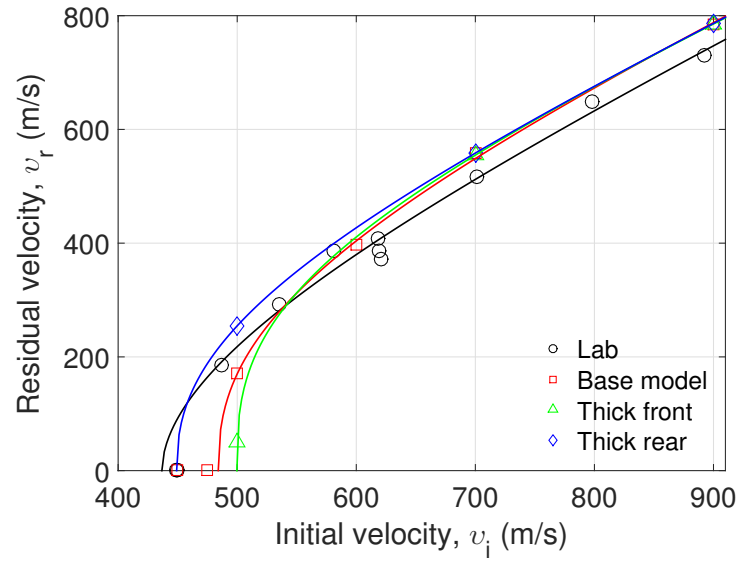


Figure 7.8: Ballistic limit curves for the plate thickness study.

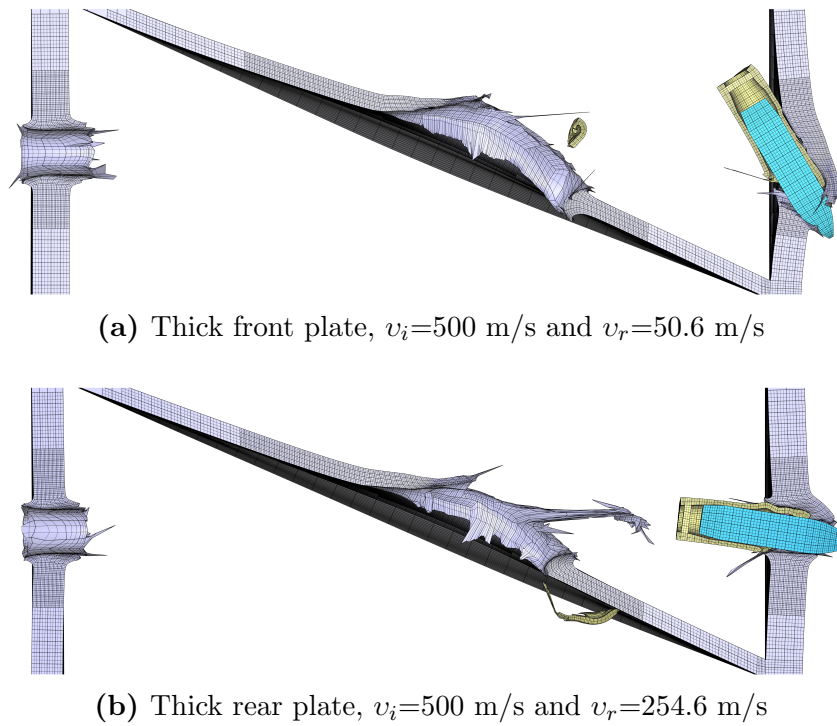


Figure 7.9: Numerical perforation process of the rear plate in plate thicknesses investigation.

Energy Balance Check

Energy balance for the base model can be seen in Figure 7.10. The two main contributors are the bullet's kinetic energy and the energy absorbed by plastic deformation in the panel. The energy balance gain was 1.5%, with a small jump seen as the bullet goes through the rear plate. As the tail of the bullet leaves the front plate, the kinetic energy in the deformable parts rises. The reason for this may be due to different velocities of the jacket and bullet core, and transfer of energy through frictional forces. The dashed line in Figure 7.10c is the average kinetic energy in the model. As seen this average is constant in the free flying phase.

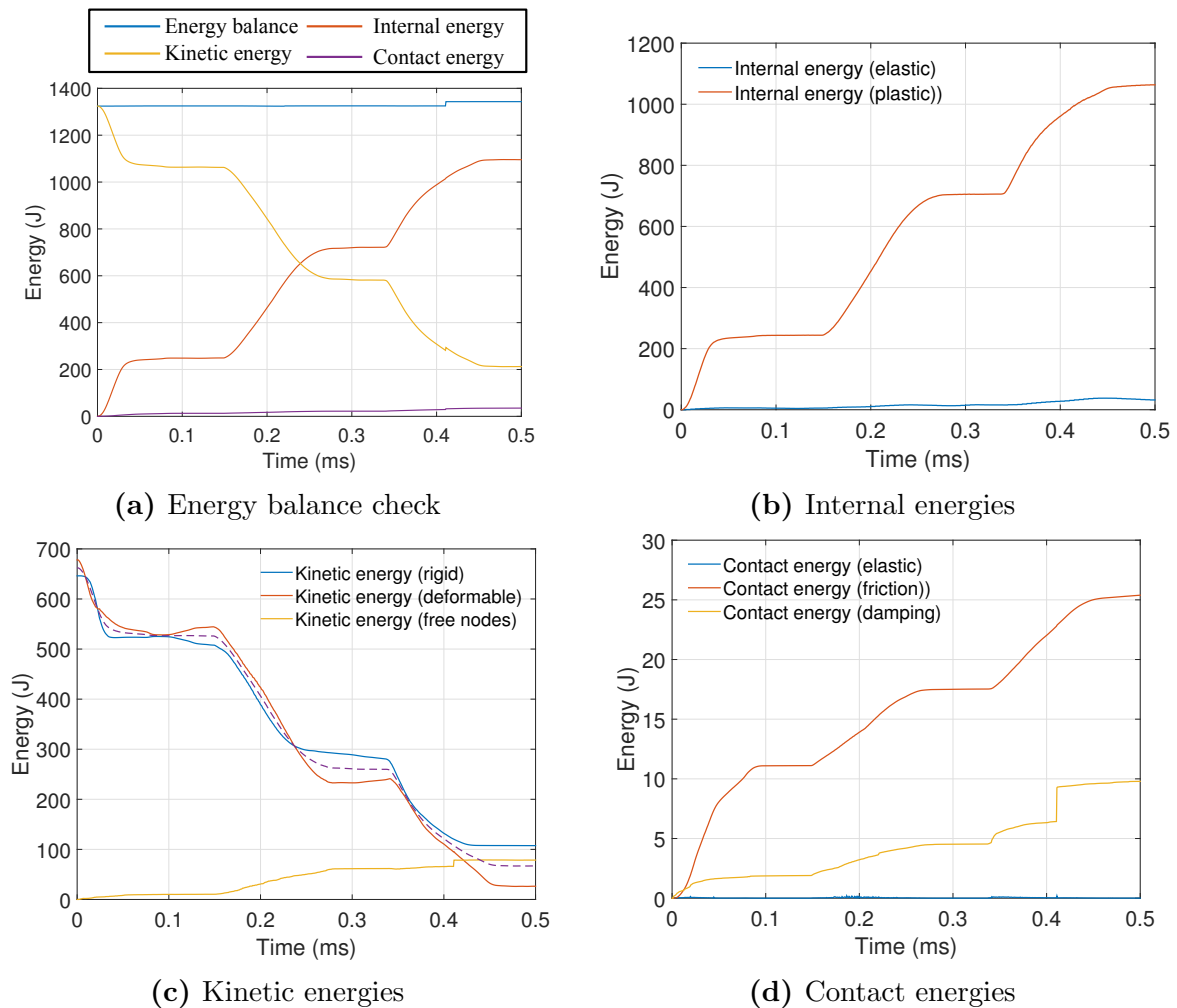


Figure 7.10: Energy balance check for the base model, $v_i = 500$ m/s and $v_r = 170.4$ m/s.

7.2 Sand Filled Aluminium Panel

7.2.1 Numerical Base Model

The aluminium panel and bullet parts were modelled as described in Section 7.1.1. The desired number of particles were placed inside the panel by the *PSOIL-card. As mentioned the particle size should be of the same order or somewhat larger than the median of the real sand to give predictive results [5]. The particle diameter was therefore set to 1.0 mm giving a required particle number of 5 000 000 to fill the aluminium panel. For comparison, simulations with particle diameter of 2.0 mm equivalent to 625 000 particles were also conducted. Calibrated parameters for each case are shown in Table 6.3. A visualization of the base model is shown in Figure 7.11.

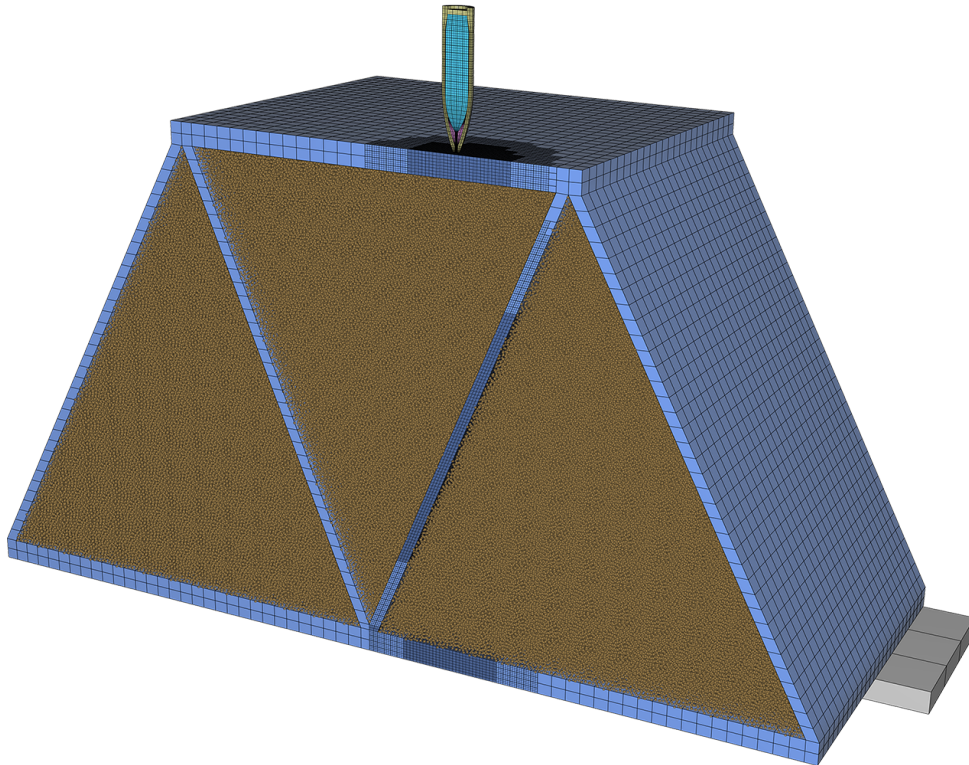


Figure 7.11: Base model AA6005-T6 aluminium panel filled with 5 000 000 sand particles, cut in half for visualization.

7.2.2 Energy Balance Check

The energy balance check for the simulation with initial velocity of 900 m/s and 5 000 000 particles is shown in Figure 7.12. A drop of 19.7 % is seen in the energy balance, which is more than the 5 % limit. More about this in Section 8.3. The main contributors are the kinetic energy of the bullet which gets transferred into plastic dissipation of the panel and discrete particle interactions, in terms of friction for this case.

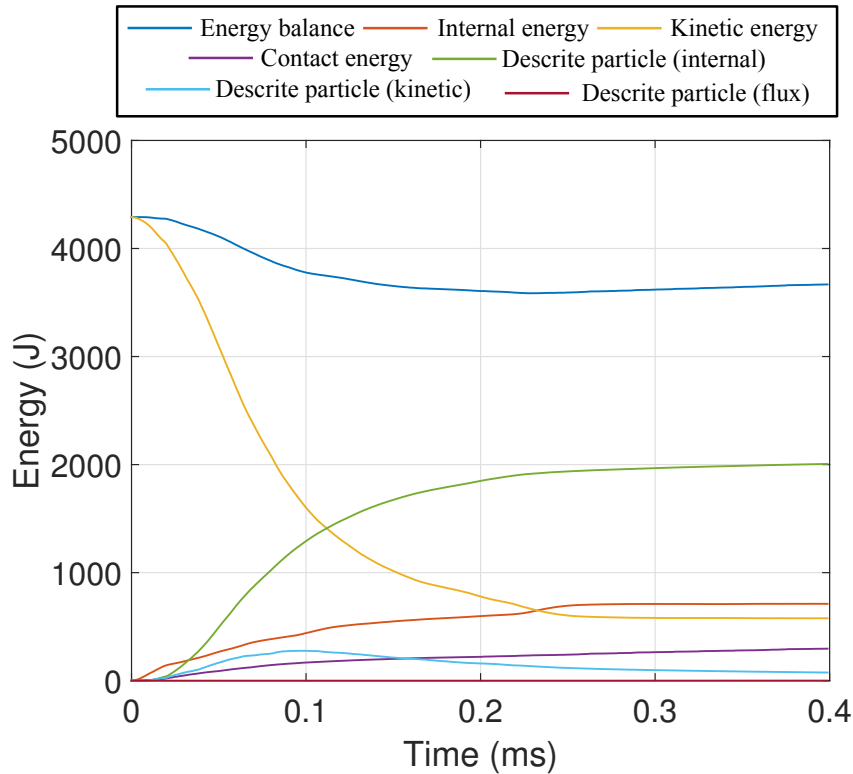


Figure 7.12: Energy balance check for sand-filled panels, $v_i = 900$ m/s.

7.2.3 Numerical Results

As for empty panels, the ballistic limit curve was established on the basis of several numerical simulations. In Figure 7.13 snapshots from simulations with initial velocities of 900 m/s and 650 m/s are shown. In this figure every part with velocity equal to, or above 30 m/s are marked red. The fragmentation seen in the slanting web for empty panels is absent when the empty cavities are filled with sand particles. Kinetic energy at impact of the slanting web is now transferred from the bullet, via the web and absorbed by underlying sand particles which are set in motion, preventing the fragmentation. Perforation of the front and rear plate are similar to what was observed for simulations without sand. The jacket is peeled of before perforation of the slanting web, just as it was in the experiments.

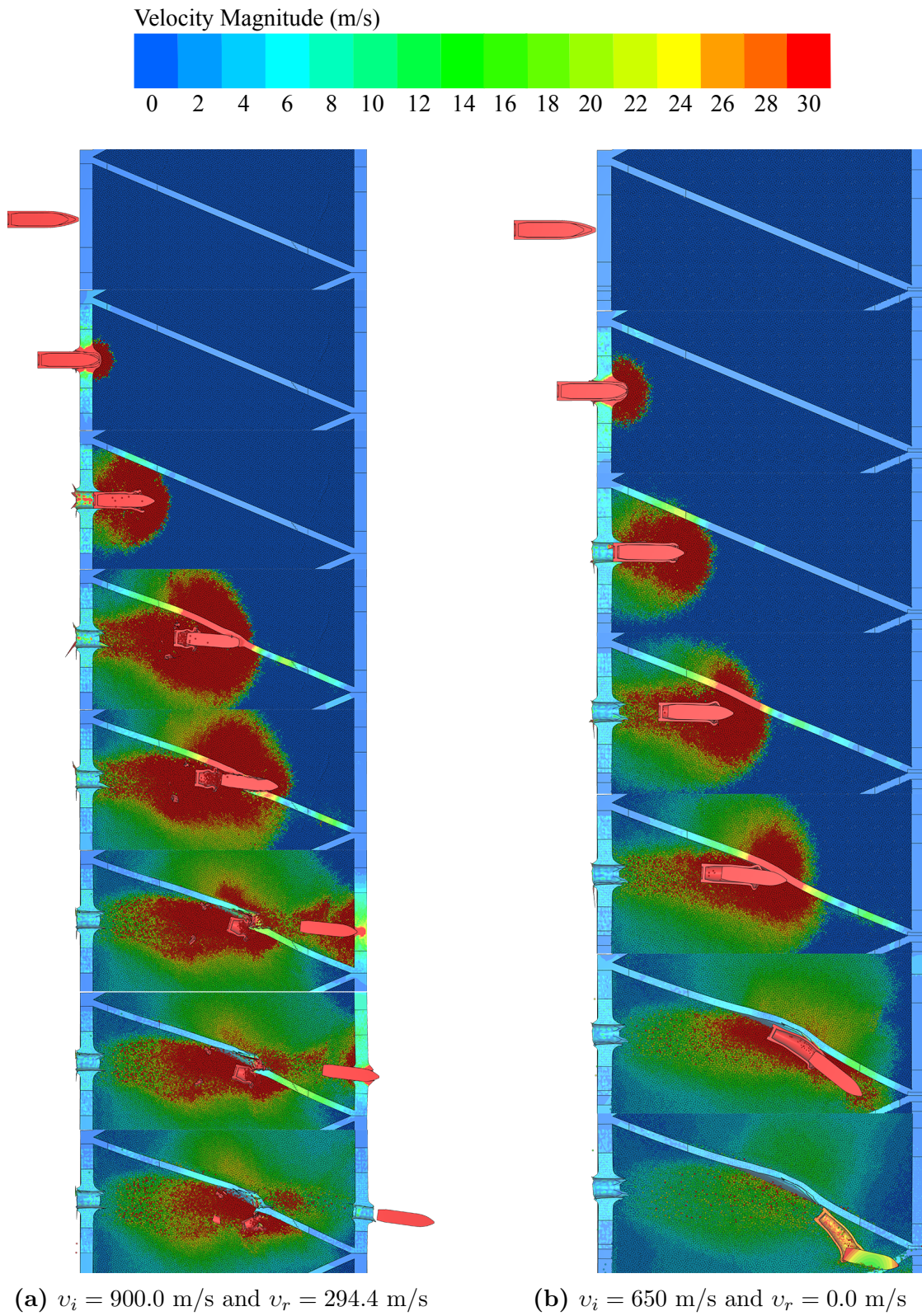


Figure 7.13: Time-lapses showing the velocity magnitude, where parts with velocities over 30 m/s are market red.

Table 7.3 shows the Recht-Ipson parameters used to establish the ballistic limit velocities. Scatter plots of the simulations and Recht-Ipson trend lines for the two calibrated parameter sets and simulations conducted with the standard dry sand model in IMPETUS Afea Solver can be seen in Figure 7.14. Parameters used in the different simulations are shown in Table 7.4. The best fit compared to the experiments is obtained with the parameters tuned against the gas-gun tests with a particle diameter of 1 mm. A deviation of 5 % is seen between the numerical simulations and the average of the ballistic limit velocities obtained experimentally for all fractions of sand. Even though the shape of the ballistic curve are poorly captured. All other tested combinations of material parameter regarding the sand gave conservative results.

Table 7.3: Recht-Ipson parameters for experiments and numerical investigated scenarios of sand-filled panels. Deviation is calculated from the average of the ballistic limit velocities of the sand-filled aluminium panels.

	a	p	v_{bl} (m/s)	Deviation from experiment (%)
Experiment (avg. v_{bl})			666.2	-
$d_s=1$ mm (calibrated)	1.12	1.13	700.0	5.1
$d_s=2$ mm (calibrated)	0.90	1.77	549.3	-17.1
$d_s=1$ mm (dry sand)	0.75	2.38	588.5	-17.7
$d_s=2$ mm (dry sand)	0.83	2.85	557.3	-16.3

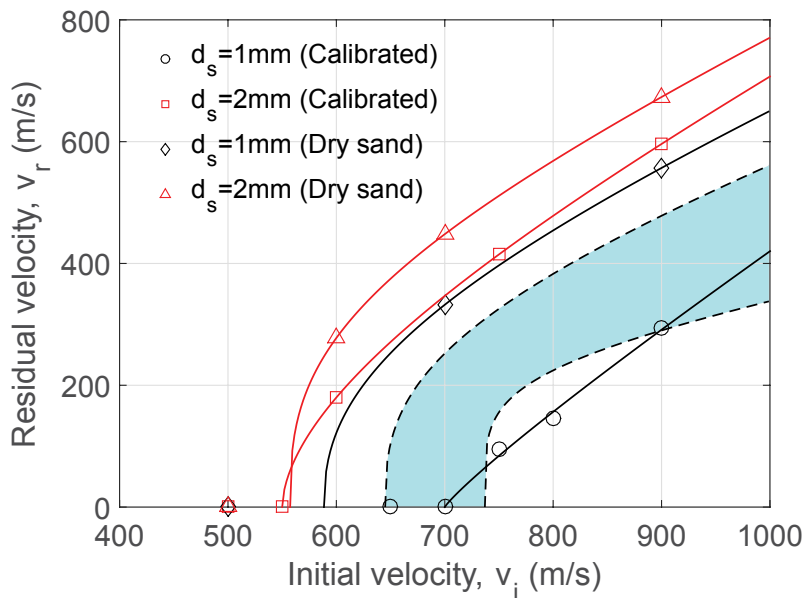


Figure 7.14: Numerical results from base model with sand particles. The blue shade within the dashed lines indicates the spread in experimental data.

Grain diameter (mm)	Soil packing scheme	Soil density (kg/m ³)	Contact stiffness (N/m)	Damping coefficient	Soil-soil friction	Soil-Structure friction
Calibrated $d_s=1$	1000	1731.3	4.0×10^8	0.00	0.25	0.30
Calibrated $d_s=2$	1000	1731.3	4.0×10^8	0.00	0.18	0.20
Dry sand $d_s=1$	1000	1731.3	4.0×10^8	0.00	0.10	0.00
Dry sand $d_s=2$	1000	1731.3	4.0×10^8	0.00	0.10	0.00

Table 7.4: Sand parameters used in the different simulations.

The linear-like relation between initial velocity and residual velocity can be because no strain rate sensitivity is included in the discrete particle module. This linear relationship is evident for high soil-soil friction and soil-structure friction, see $d_s=1$ mm (calibrated) in Figure 7.14. Major difference between the two calibrated parameter sets are obtained in the complete panel simulations. These parameter sets predicted almost the same residual velocity for the gas-gun simulations, but in the complete panel simulations, a difference of 21 % is obtained in ballistic limit velocity. This may be due to the altered geometry, sand thickness, increased effects of soil-soil friction or soil-structure friction parameter, etc. For example the thickness is changed from 50 mm in the gas-gun simulations to approximately 130 mm in the complete sand-filled panel simulations.

7.3 Comparisons

7.3.1 Numerical Output for Empty and Sand-filled Panels

Velocity versus displacement curves for one of the front nodes in the rigid core are shown for simulations of both empty and sand-filled panels in Figure 7.15. The curves are similar until the bullet has perforated the front plate. At this point, the resistance from the particles in the sand-filled model is initiated, further slowing down the bullet. The bullet in the empty panel simulation is on the other hand in free flight phase subjected to no resistance. This is the start of the clear difference in velocity reduction between empty and sand-filled panels. The perforation of the three plates making up the aluminium panels can be observed by the three distinct drops in velocity.

Typical computation times for empty panels varied from 12 h ($v_i=900$ m/s) and 35 h ($v_i=450$ m/s) depending on the termination time ranging from 250 μ s and 700 μ s respectively. For sand-filled panels containing 5 000 000 particles, the computation times became 53 h ($v_i=900$ m/s) and 82 h ($v_i=700$ m/s) for termination times of 400 μ s and 750 μ s respectively.

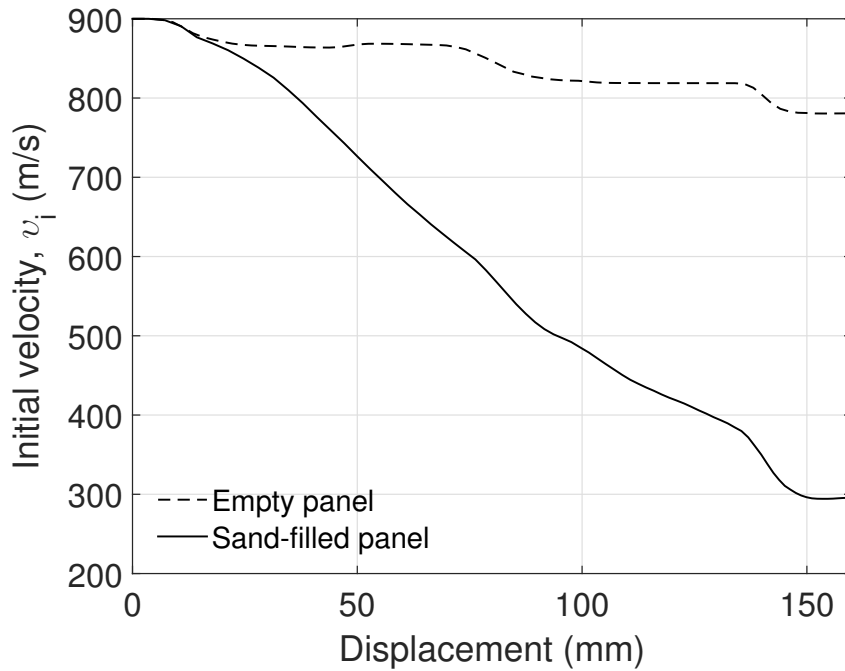


Figure 7.15: Velocity versus displacement for base model simulations, $v_i=900$ m/s

Another difference between simulations of empty and sand-filled panels is how the jacket behave during the penetration process. In empty panels the jacket is attached to the core through the penetration of the whole panel, while for sand-filled panels the jacket is peeled of before or during the penetration of the slanting web in all simulations including sand. Some examples of brass jacket response from different simulations are shown in Figure 7.16.

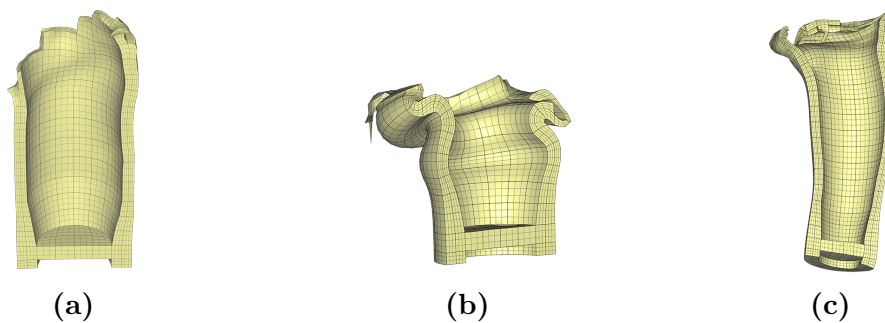
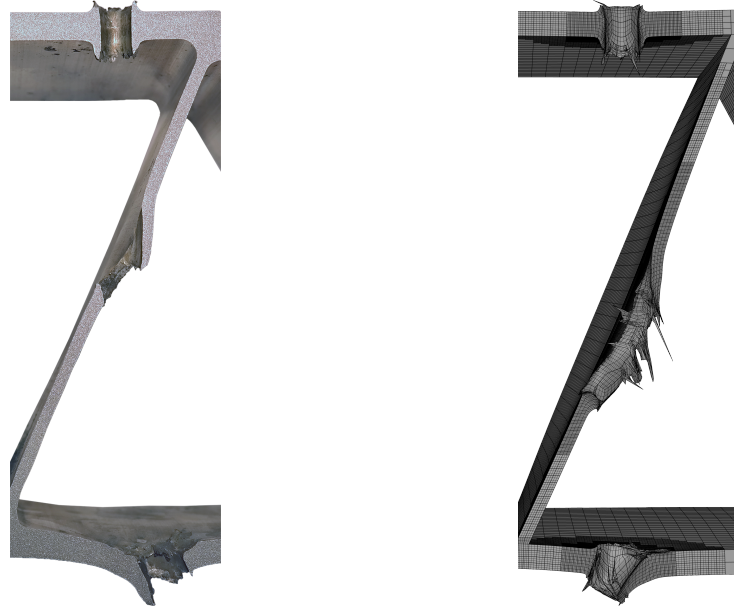


Figure 7.16: Jacket response, (a) $v_i=900$ m/s without sand, (b) $v_i=900$ m/s with sand, and (c) $v_i=650$ m/s with sand.

7.3.2 Experimental and Numerical Response

The impact response to the aluminium panel itself is well adopted in the numerical simulations. The ductile hole growth are captured in the perforation of the front and rear plate. More damage is seen in the slanting web from the numerical simulations than the experiments (Figure 7.3a). The bullet orientation after perforation of the slanting web is

opposite in the numerical simulations than for the experiments from empty panels. This can clearly be seen from the exit holes in the panel. In sand-filled panels this phase of the penetration is better captured in the numerical simulations. Less fragmentation is seen both experimentally and numerically from the slanting web, which is most likely because of the stabilizing effect from the sand particles.



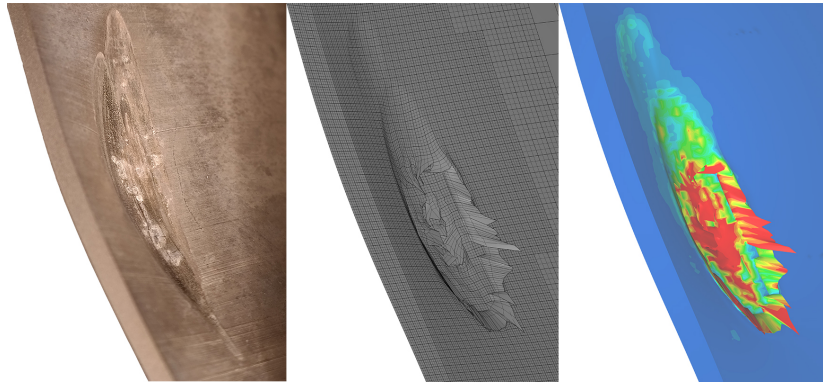
(a) Cross section from shot No. 7, $v_i = 534.9$ m/s and $v_r = 292.6$ m/s
 (b) Numerical cross section, $v_i = 500.0$ m/s and $v_r = 170.4$ m/s



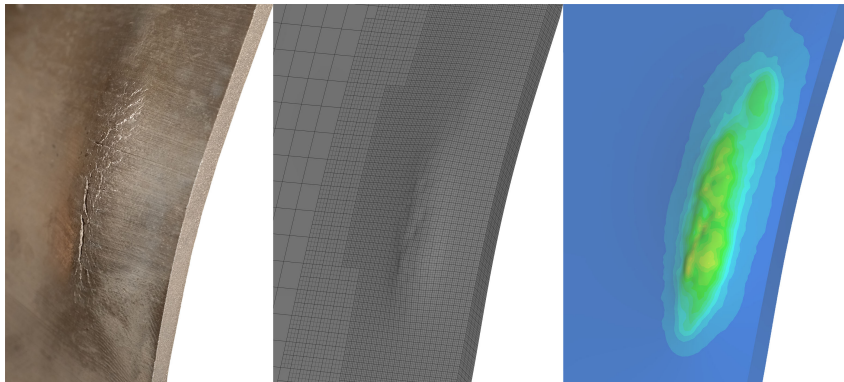
(c) Cross section from shot No. 1 for B95, $v_i = 910.5$ m/s and $v_r = 485.4$ m/s
 (d) Numerical cross section, $v_i = 900.0$ m/s and $v_r = 294.4$ m/s

Figure 7.17: Comparison of cross sections, experimental tests and numerical simulations. Empty panel is showed in the top pictures, while sand-filled panel can be seen on the bottom pictures.

In simulations below the ballistic limit velocity, the numerical response is normally such that the bullet ricochets in the slanting web. This phenomenon is also seen from the experiments, where a comparison to the simulations is seen in Figure 7.18. This figure shows the experimental results for an initial velocity of 734.3 m/s together with numerical output and damage evaluation for a numerical simulation with initial velocity of 650 m/s.



(a) Sliding marks in slanting web impact side



(b) Sliding marks in web back side

Figure 7.18: The left picture shows shot No. 5 with B95 sand. Numerical element response in the middle and element damage to the right. Red means that the elements failure criterion is reached.

Chapter 8

Sensitivity Studies

To get an understanding of the influence of the various parameters used in the numerical part of this thesis, a sensitivity study is presented in this chapter. Simplified models are used to save computational time. Three different parameter studies are presented. The first considers a straight plate representing the front and rear plate of the panel. The second examines the slanting web, while the third discusses the parameters of the discrete particle module in IMPETUS Afea Solver.

Standard model will in this chapter refer to the simplified model with parameters taken from the base models presented in Chapter 7. Direct experimental data is not available for comparison between numerical results in this section. Numerical results are therefore compared with the residual velocity and response from the standard model.

8.1 Straight Plate

To investigate the decisions taken regarding input data for the front and rear plate of the panel, a simplified model including a straight plate and the APM2 bullet was created. In most simulations only the steel core of the bullet was modelled to save computational time. The applied materials are described in Section 7.1.1. The symmetry of the problem was exploited and only half the plate and bullet were modelled. Boundary conditions were introduced on the left and right hand side of the plate with translation prevented in all directions. This was done to replicate the conditions where the plate is a part of the panel. The model is shown in Figure 8.1.

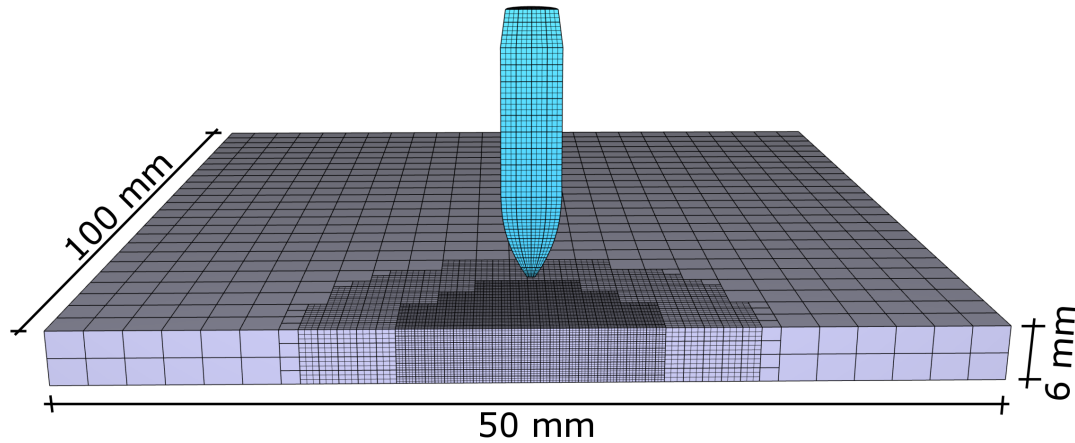


Figure 8.1: Simplified numerical model for the parameter study of the front and rear plate.

8.1.1 Rigid Steel Core versus Full Bullet

The difference in residual velocity between modelling the full bullet versus only the rigid steel core is investigated in this section.

Previous investigations have shown small difference between the two cases [18, 63]. The same tendency is seen in this study for initial velocities well above the ballistic limit velocity, but as the initial velocity decreases the difference in residual velocity becomes more distinct (Figure 8.2). The plate thickness and material properties are different in this thesis from the earlier performed investigations, and this is most likely the reason for the varying result.

When modelling the full bullet the projectile diameter increases, further leading to a rise in resistance as the projectile perforates the aluminium plate. The added mass from the brass jacket and lead tip is not able to overcome the increased resistance, resulting in a 21.0 % increase in ballistic limit when the full bullet is modelled (Table 8.1). Modelling the full bullet appears to make a difference for low velocities, thus the decision of including the full bullet seems correct when the whole panel is considered.

Evidently modelling the full bullet makes a difference for low velocities, thus the decision of including the full bullet seems correct when the whole panel is considered.

Table 8.1: Ballistic limit, rigid core versus full bullet.

	v_{bl} (m/s)	Difference (%)
Rigid core	221.2	-
Full bullet	267.6	21.0

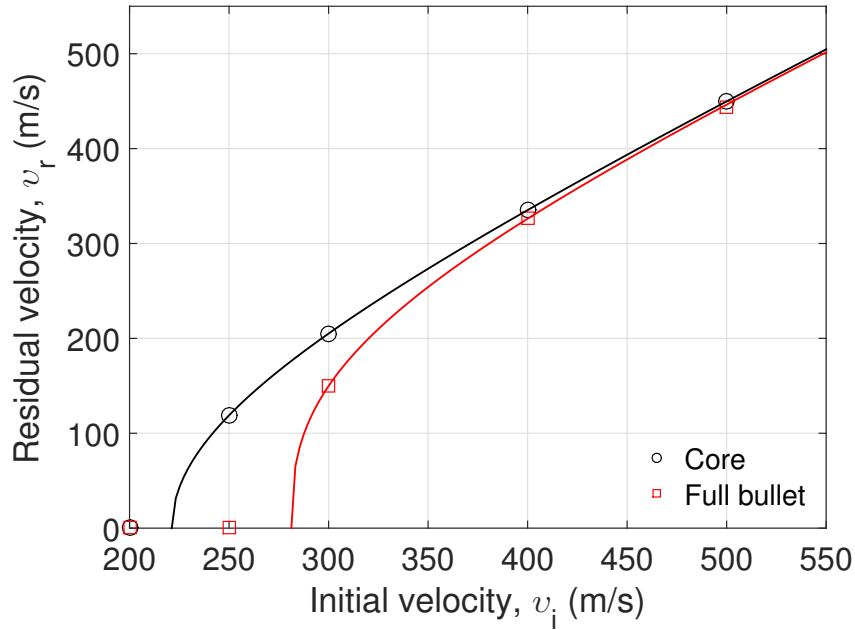


Figure 8.2: Ballistic limit curves for the simplified model with steel core and full bullet.

8.1.2 Element Erosion

Element erosion, Δt_{erode} , is a user defined value that controls when elements are eroded. If the element's time step drops below this value the element is eroded from the simulation. In the base models this parameter was selected to 2 ns. This value was chosen to limit the computational cost in the base model. In this simplified model a much lower Δt_{erode} can be selected without sacrificing the efficiency too much. An initial velocity, v_i , was set to 300 m/s and simulations with Δt_{erode} equal to 4 ns, 2 ns, 1 ns and 0.5 ns were conducted to capture any differences in the residual velocity. A lowered time erosion parameter allows each element to deform more before it is removed from the simulation. By allowing more deformation in each element the minimum length of an element are reduced, also decreasing the critical time step in the explicit numerical analysis. Consequently a lower time erode parameter will lead to longer calculation times. Results are shown in Table 8.2. The solution has not yet converged, but compared with the computational cost a time erode parameter of 2 ns seems to give satisfactory results.

Table 8.2: Effect of different time erosion values on the v_r , for straight plate with $v_i = 300$ m/s.

Factor from base model	Time erosion (ns)	v_r (m/s)	Computational time ¹ [h:m]	Difference from base model (%)
Higher [2x]	4	207.0	[0:46]	+1.07
Standard model	2	204.8	[1:01]	-
Lower [0.5x]	1	202.6	[1:57]	-1.07
Lower [0.25x]	0.5	202.0	[5:53]	-1.37

¹ Note that the computational time is affected by the workload on the server, so only the trends in computational time should be considered.

8.1.3 Mesh Sensitivity

The impact zone in the front and rear plates was modelled using elements with dimensions $w \times h \times t = 1 \times 1 \times 0.75$ mm, which gave 8 elements over the plate thickness. In order to investigate the effect of the element size on the perforation process three new meshes were made. The results are tabulated in Table 8.3. Small differences in the residual velocity between the standard model and the finer mesh ($0.5 \times 0.5 \times 0.5$) were seen. Not so insignificant is the seven-fold increase in computational cost. This implies that the base model gives sufficient accuracy when taking the computation time into account.

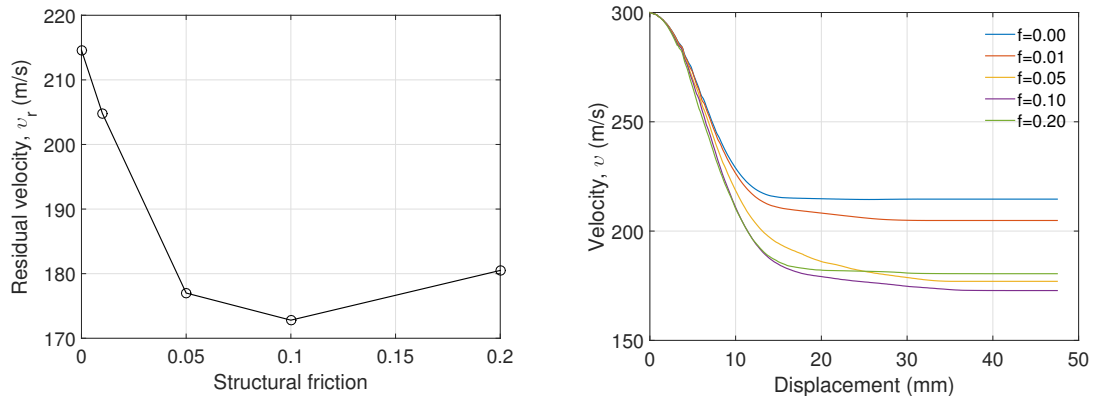
Table 8.3: Effect of different mesh sizes on the v_r for the straight plate, $v_i = 300$ m/s.

Dimensions ($w \times h \times t$) (mm)	Elements over thickness	v_r (m/s)	Computational time ¹ [h:m]	Difference from base model (%)
($2 \times 2 \times 2$)	3	191.4	[0:26]	-6.54
($1 \times 1 \times 1$)	6	203.8	[1:19]	-0.49
($1 \times 1 \times 0.75$) Standard	8	204.8	[1:01]	-
($0.5 \times 0.5 \times 0.5$)	12	203.7	[7:14]	-0.54

¹ Note that the computational time is affected by the workload on the server, so only the trends in computational time should be considered.

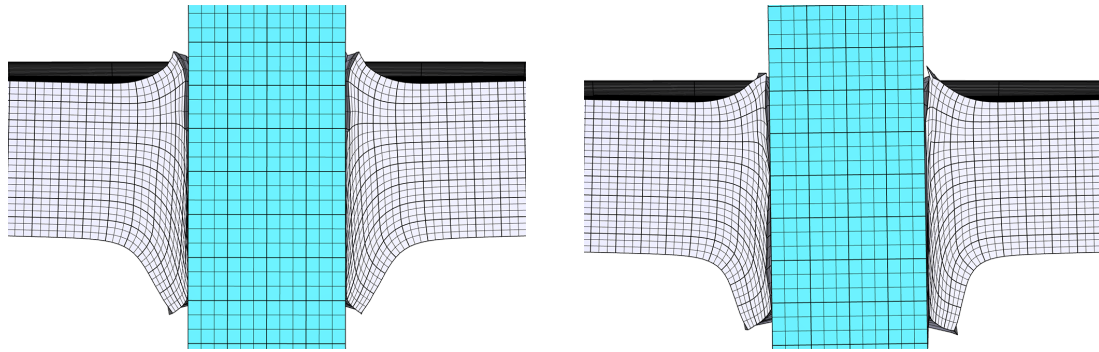
8.1.4 Contact Friction Coefficient

The friction parameter is set to 0.01 in the base model simulations as proposed in Zukas [10]. A study on the effects of friction parameters of 0, 0.01, 0.05, 0.1 and 0.2 is shown in Figure 8.3. Higher friction may cause elements to reach failure ($D \geq 1$) faster, resulting in removed shear stresses for the elements and less resistance in the plate. This may also cause less contact between the core and aluminium plate late in the perforation process as shown in Figure 8.4, when only the after-body of the core is in contact with the plate. An example of this is the frictionless behaviour seen with a contact friction of 0.2 in Figure 8.3b.



(a) Effects of contact friction coefficient on the residual velocity (b) Effects of contact friction on the velocity during perforation of the plate

Figure 8.3: Effects of contact friction.



(a) Cross section, friction parameter of 0.05 (b) Cross section, friction parameter of 0.2

Figure 8.4: Zoomed in pictures showing the effects of contact friction on the element response.

8.2 Slanting Web

A simplified model for the web is shown in Figure 8.5. Also here the symmetry of the problem was exploited and only half the plate and bullet were modelled. The model is used to explore important aspects such as element orientation, bullet type, element size, element erosion and bullet oblique angle. A bullet core with an initial velocity of 400 m/s will only slide against the web without perforating (Figure 8.6). An initial velocity of 500 m/s is therefore used in this investigation unless otherwise is specified. Figure 8.7 shows a snapshot from the high-speed camera with the slanting web and bullet right after perforation. Note that the bullet's orientation rotates against the direction of the slanting web.

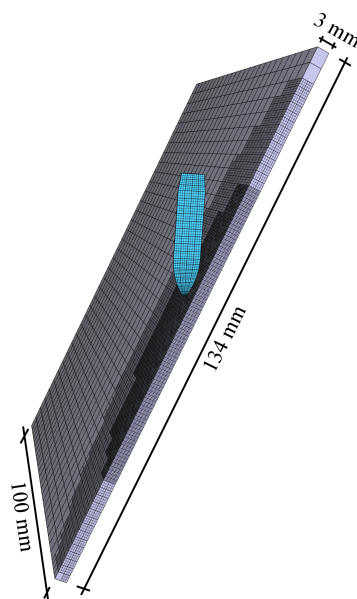


Figure 8.5: Simplified numerical model for the parameter study of the slanting web.

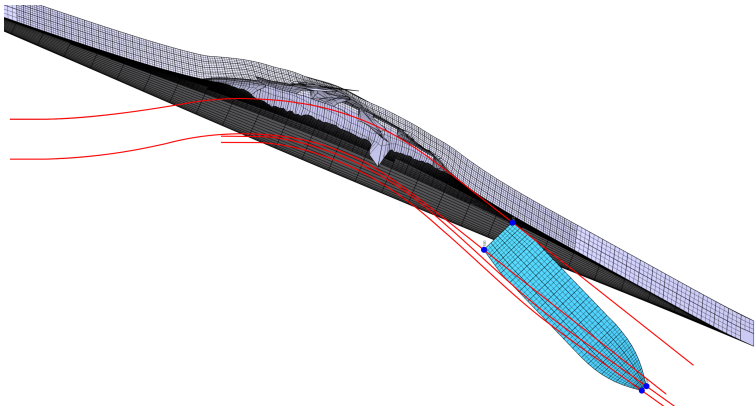


Figure 8.6: Bullet trajectory for $v_i=400$ m/s and $v_r=241.1$ m/s.

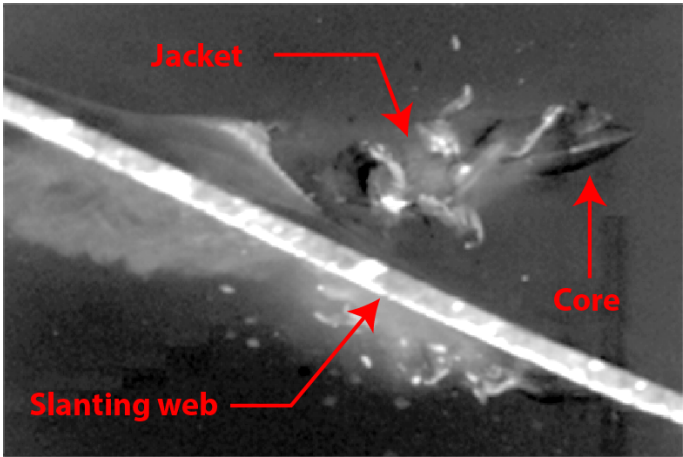


Figure 8.7: Test No. 3 from the experimental testing of empty panels.

8.2.1 Element Orientation

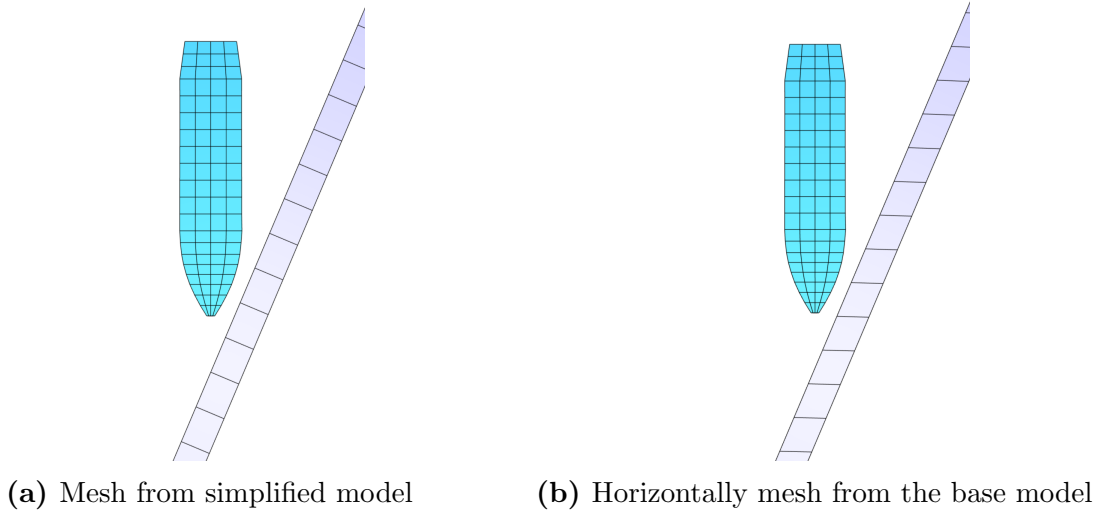


Figure 8.8: Meshes with different element orientation.

The simplified model is created with the elements orientated in the plate thickness, while in the base model the mesh is orientated with the top and bottom boundary horizontally as shown in Figure 8.8. In order to check if this element orientation has any effect on the numerical results, simulations with initial velocities of 400 m/s, 500 m/s, 600 m/s and 900 m/s were performed. Small differences are seen in performance between the two meshes, only for initial velocity of 400 m/s the difference is notable as seen in Table 8.4. At this initial velocity the bullet only slides against the web without perforating. Higher initial velocities give good compliance between the two different meshes.

Table 8.4: Results of element orientation study.

v_i (m/s)	Panel mesh v_r (m/s)	Simplified model v_r (m/s)	Difference %	Comment
400	233.7	241.1	-3.07	Slides, no perforation
500	430.7	432.2	-0.35	-
600	549.7	551.3	-0.29	-
900	863.8	865.0	-0.14	-

8.2.2 Steel Core versus Full Bullet

Due to the high initial velocity needed to perforate the web, the differences seen by modelling the full bullet are small. Tabulated differences can be seen in Table 8.5. At $v_i=400$ m/s both the steel core and the full bullet are sliding, but with a quite varying result in residual velocity. This can be due to the extra excavating of the web carried out by the jacket.

Table 8.5: Results from steel core versus full bullet study for the slanting web.

v_i (m/s)	Full bullet v_r (m/s)	Core v_r (m/s)	Difference %	Comment
400	185.0	241.1	-23.27	Slides, no perforation
500	437.5	432.2	1.23	-
600	539.7	551.3	-2.10	-
900	854.1	865.0	-1.26	-

8.2.3 Mesh Sensitivity

In the base model the impact zone in the web is modelled with element dimensions of $w \times h \times t = 1 \times 1 \times 0.75$ mm, giving four cubic hexahedra elements over the thickness. New simulations with one, two, three, and six elements over the thickness have been run to capture any differences and validate convergence of the base model mesh. Figure 8.9 clearly shows the difference in performance between the meshes, and Table 8.6 shows residual velocity and computational cost for each mesh. To see if fewer elements could be used, meshes with one and two elements over the thickness were tested. It is clearly seen that one element does not capture the nature of the impact problem. The bullet tip is ploughing through the elements, because their time step drops below the 2 ns limit and erodes. This causes the bullet to rotate with the web as indicated by the lines tracing the highlighted elements, with the result of overestimating the resistance in the web. The mesh with two elements is more suitable, but still overestimates the resistance. In the standard model the projectile trajectory looks more as it did in the experiments (Figure 8.7). The bullet is slightly rotating the opposite way of the slanting web after perforation. One finer mesh was tested to check if the base model mesh gives adequate results considering the residual velocity. With this mesh the bullet is rotating slightly more and the residual velocity decreases by 0.22 %. This refined mesh provides better results but also a doubling in the computational cost for this simple model. This shows that the base model mesh provides adequate accuracy compared to computational time.

Table 8.6: Effect from different mesh sizes on the v_r and bullet trajectory for slanting web with $v_i = 500$ m/s.

Dimensions ((w×h×t) mm)	Elements over thickness	v_r (m/s)	Computational time ¹ [h:m]	Difference from standard model (%)
(3×3×3)	1	140.0	[00:26]	-67.61
(1.5×1.5×1.5)	2	384.8	[01:08]	-10.97
(1×1×1)	3	427.8	[01:53]	-1.02
(1×1×0.75) Standard	4	432.2	[04:25]	-
(0.5×0.5×0.5)	6	431.3	[10:28]	-0.22

¹ Note that the computational time is affected by the workload on the server, so only trends in computational time should be considered.

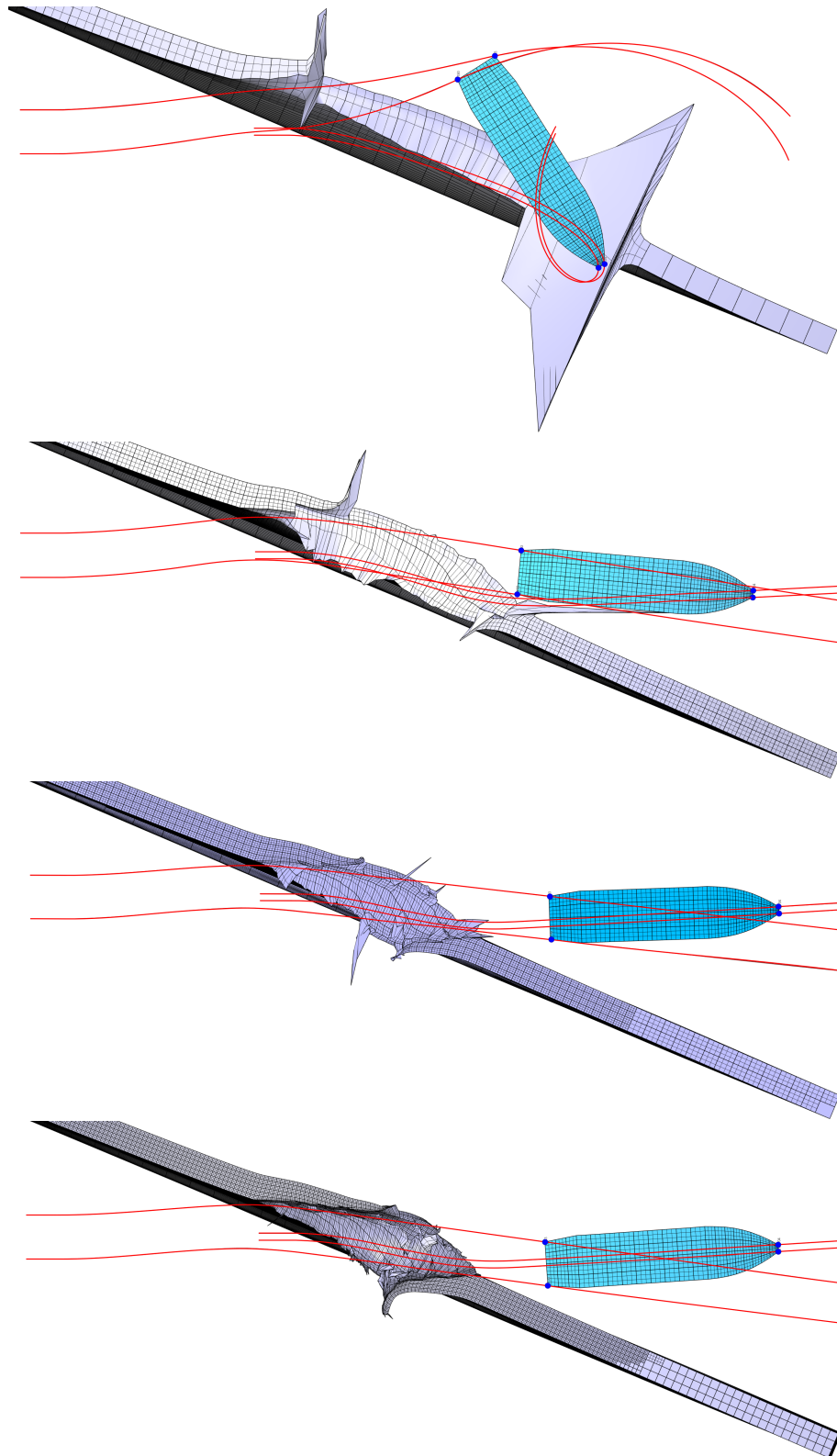


Figure 8.9: Pictures from the mesh sensitivity study for the slanting web. The lines shows the path of the highlighted nodes. From the top; one element over the thickness, two elements over the thickness, the standard model and in the bottom six elements over the thickness.

8.2.4 Bullet Impact Angle to Slanting Web

The impact angle is important for the projectile trajectory and the residual velocity after interaction with the slanting web. Different angles have therefore been tested to capture any effects on the projectile, with the results plotted in Figure 8.10. The numerical results show little change in residual velocity for angles up to 30° . This is also well documented from experimental and numerical work by Børvik et al. [61]. An increasing oblique angle will result in a larger effective plate thickness during the penetration, leading to a reduction in residual velocity. The critical angle for an initial velocity of 500 m/s seems to be between $70-75^\circ$, where the penetration process is transferred from perforation to ricochet. The slanting web seems to have an ideal angle for impact resistance when the bullet impacts normal to the front panel plate for initial velocity of 500 m/s.

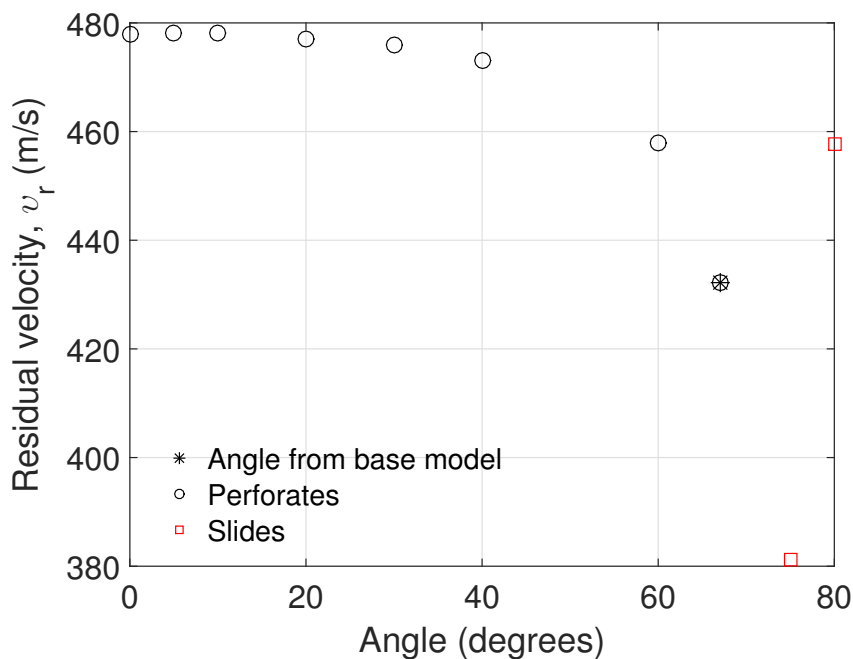


Figure 8.10: Web angle versus residual velocity, $v_i=500$ m/s.

8.3 Sand

The discrete particle module in IMPETUS Afea Solver is employed to represent the sand behaviour as earlier mentioned. The model appearance and behaviour is adjusted by changing the parameters in the rheological model. An overview over the sensitivity for different values of the various parameters is tried shown in this chapter.

Soil-soil Contact Stiffness

The contact stiffness between particles is an important parameter for the interaction between sand particles. Different values of this stiffness have been tested throughout the numerical work. An overview of the resistance effect from the calibration simulations in the range of contact stiffness, k_s , from 50-5000 MN/m, is given in Figure 8.11. The initial velocity was chosen as 250 m/s, while all other parameters in the *PSOIL-card were set to default. The default stiffness of 400 MN/m seems to separate two areas with completely different rate of effect to resistance. Lower stiffness than default clearly reduces the resistance, while increased stiffness would give a slack increase in resistance. The sensitivity check is performed with the circular sand box model containing 1 000 000 particles ($d_s=1.41$ mm) with default values for all relevant soil parameters, except from contact stiffness.

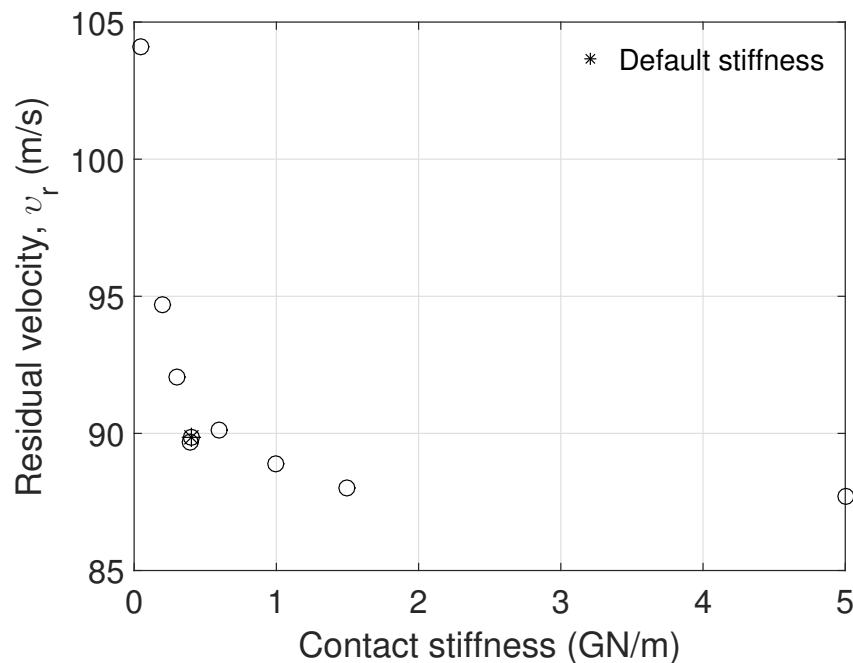


Figure 8.11: Different values of contact stiffness related to residual velocity from the circular sand box simulations.

Soil-structure Contact Coefficient of Friction

The soil-structure contact friction regulates the friction between structural elements and soil particles. The default value for this parameter in standard dry sand is 0. A variety of values were tested during the numerical calibration of sand. In the numerical model with the circular sand box, this parameter is seen to have limited effect in contrast to the friction between soil particles. This is most likely because of the minor area from the sphere projectile in interaction with the particles. Figure 8.12 shows a comparison between soil-structure and soil-soil friction in regards to residual velocity of the projectile or similarly the resistance caused from interaction between particles.

Soil-soil Contact Coefficient of Friction

Friction between particles is adjusted by this Coulomb friction coefficient. The tangential stiffness in the rheological model is further limited by this parameter according to Børvik et al. [3]. The sensitivity study of the circular sand box shows that this coefficient clearly affects resistance from the rheological model of the particle module significantly. In the default settings of dry sand this coefficient is 0.1. Since the movement interaction between soil grains is the main event in this model, it was decided to use this coefficient as the primary tune-in parameter for the calibration of sand from experimental findings. The soil-structure coefficient was taken as the secondary parameter to further fine tweak the resistance.

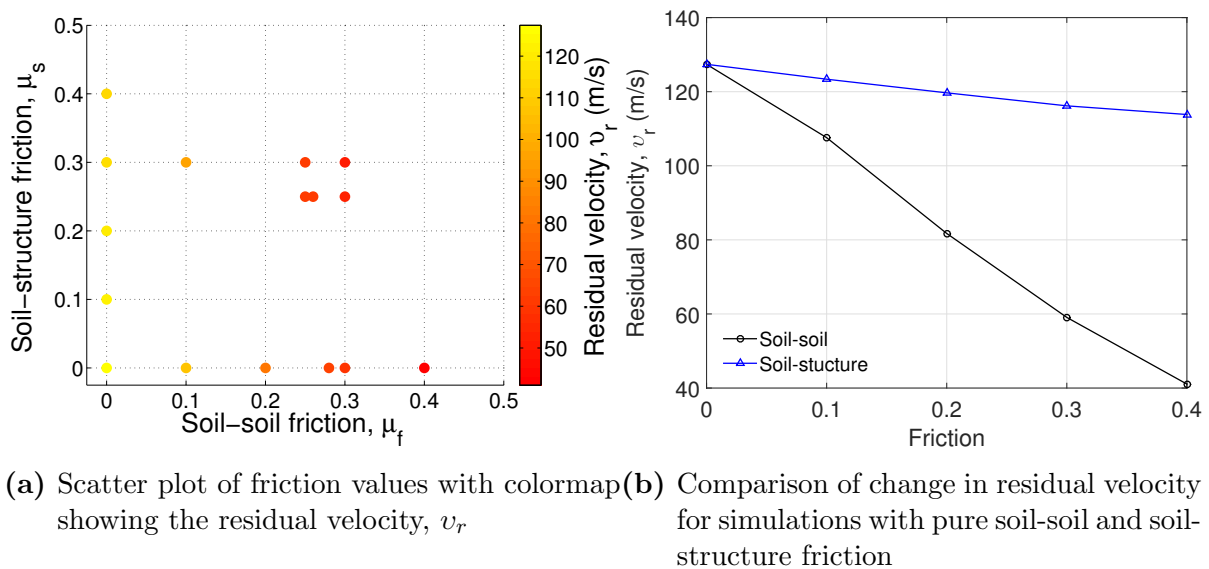


Figure 8.12: The resistance effect of soil-structure friction and soil-soil friction in the circular sand box. Simulations run with initial velocity of $v_i=278.2$ m/s and soil density of 1731.3 kg/m³. Default values of other relevant soil parameters.

Soil-soil Damping Coefficient

The damping coefficient is a fraction of the critical damping in the rheological model, which is by default 0 for dry sand. The sensitivity of this factor has been further checked by simulations with the circular sand box model. With a particle size of 1.0 mm (2 750 000 particles) together with a density of 1730 kg/m³ and default values for other soil parameters, the outcome of adjusting the damping coefficient can be seen in 8.13. The effect of changing this parameter is as seen almost insignificant for reasonable values. Because of the small influence to this problem the coefficient was decided to remain by default value in the calibration of the sand.

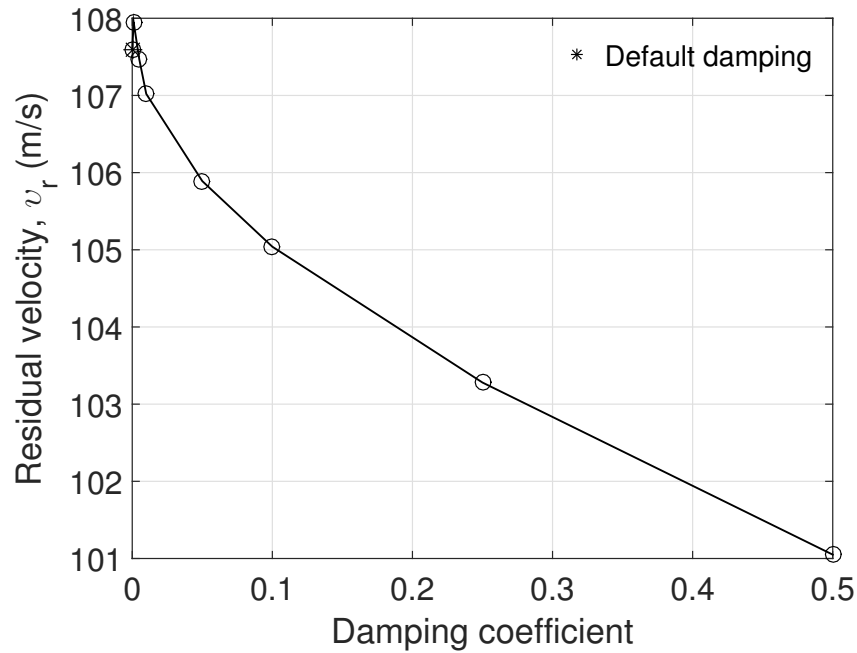


Figure 8.13: Effect of changed damping coefficient for the circular sand box model.

Soil Packing Scheme

The particles in a defined soil domain are positioned in pre-made unit cells implemented in the IMPETUS Afea Solver. The two packing schemes available consists of unit cells with either 1 000 or 10 000 particles, where the former is used in default dry sand. A closer look into Figure 8.14 will show the repeated unit cells in the soil domain. The number of packing cells in a soil domain is further dependent on the particle number. Four different cases from the calibration simulations were tested to both soil packing schemes, giving a deviation from 1-3 % in resistance. All the soil parameters except from soil packing scheme and soil density were set to default during this check.

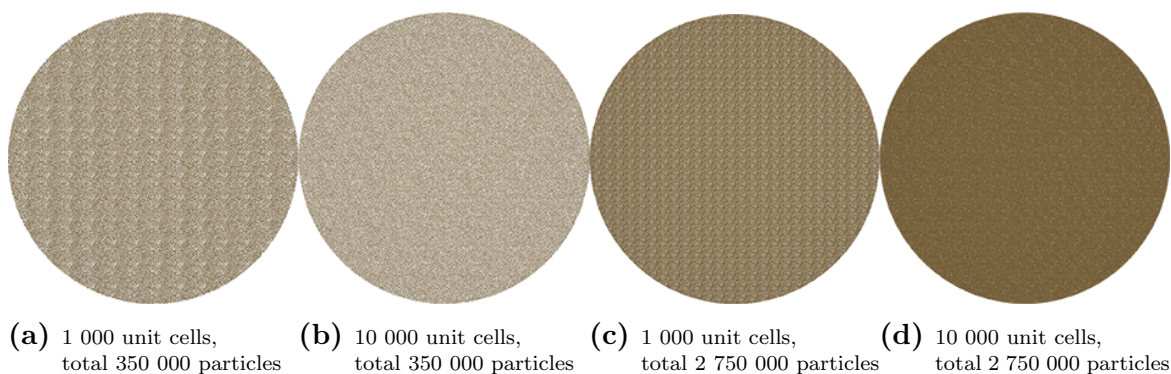


Figure 8.14: The circular sand model from calibration showing the pattern for the two unit cell packing schemes with particle sizes of 2.0 mm (350 000 particles) and 1.0 mm (2 750 000 particles).

Point of Attack in Sand Cell

The implemented unit cell contains randomly arranged particles to better represent a realistic sand sample. Since the particles are not packed in a uniform pattern, the projectile may be subjected to different resistance depending on the penetration path. This factor is further investigated in this section by simulations in the circular sand box model. The initial impact point to the sand sample was varied within the circular opening of 25 mm in diameter. This was assumed to be sufficient to capture the model's anisotropy due to repeated unit cells. The characterized sand density of 1730 kg/m^3 together with default dry sand parameters were used to the 2 750 000 particles in the model, corresponding to 1.0 mm particle size. The variation in residual velocity was found to vary less than 2.5 %.

Number of Particles

The number of particles is as earlier mentioned an important factor in the discrete particle module. The more particles or equivalent less particle size, is seen to give less resistance to penetration. This may be due to that the sand is loosing the effect of discretizing itself, thus behaving more as a continuum because of the many small particles, leading to less need of force exerted in pushing the particles away. The previous statement only holds for smaller particle diameters than 2.0 mm, as the model totally loses the resistance effect at larger grain sizes than $d_s=2.5 \text{ mm}$. Around $d_s=2.0 \text{ mm}$ in particle size seems to give the most resistance with respect to the circular sand box model. A particle size of $d_s=1.0 \text{ mm}$ were carried out to represent the B95 sand in the simulations of the aluminium panel as earlier mentioned. In addition simulations with particle diameter of 2.0 mm were simulated as comparison.

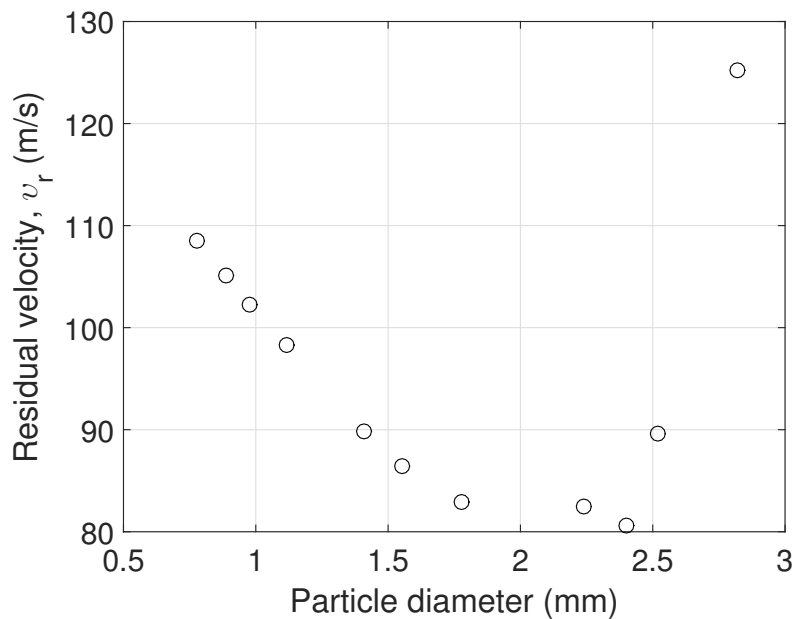


Figure 8.15: Sand particle diameter versus residual velocity, when $v_i=250 \text{ m/s}$ and default dry sand parameters.

Soil Density

The soil density or compaction state is an important feature of a sand sample as mentioned in Chapter 2. The B95 sand used in the component experiments was measured to have a density of 1730 kg/m^3 . This value is therefore also used as soil density in the numerical simulations. Measured density of both loose and dense conditioned sand for the three fractions have been further checked in simulations with respect to performed resistance, as listed in Figure 8.16. The results shows a quite linear behaviour between density and resistance when the soil parameters are default and the particle size is set to $d_s=1.0 \text{ mm}$.

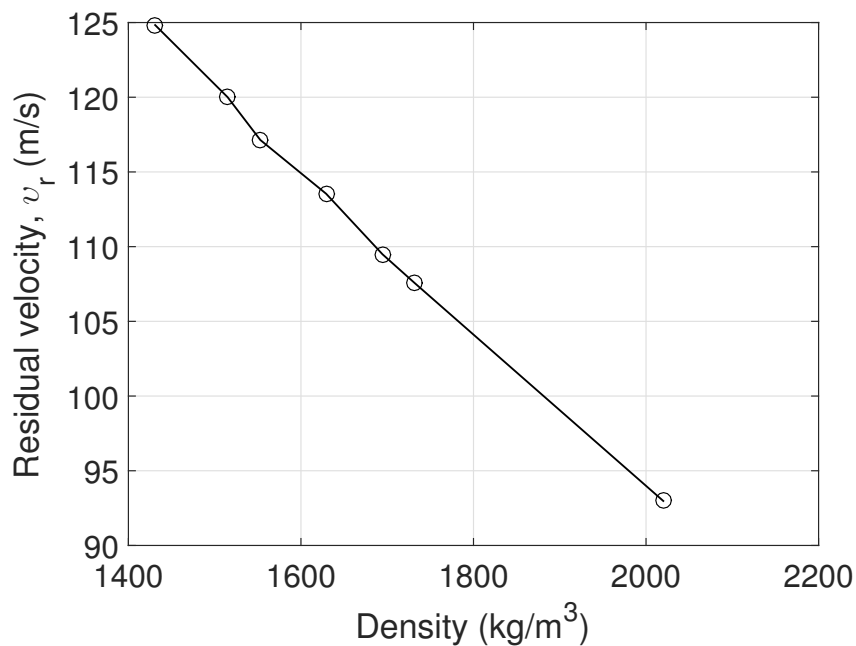


Figure 8.16: Effect of changed soil density for the circular sand box model.

8.3.1 The Variation in Energy Balance

The difficulties to obtain a sufficient energy balance as seen from Section 7.2 have been further investigated. It turns out that the problem originates from the particle model, more particularly from the friction definition. Simulations with different values of the soil-soil friction and soil-structure friction were listed and compared in terms of energy balance, as seen in Figure 8.17. The built-in default parameters for friction in the particle model seem to give a stable energy balance. By increasing the friction values the energy balance tends to drop when the particles are accelerated. Simulations with no friction at all will instead add energy to the system. By looking at the curves one can see that the energy balance fall is most sensitive to the parameter from soil-structure friction, but also the soil-soil friction parameter has an influence.

The customization of friction values in the discrete particle module is a new and relatively unexplored part of the software, so this may be a bug in the calculation of friction energy.

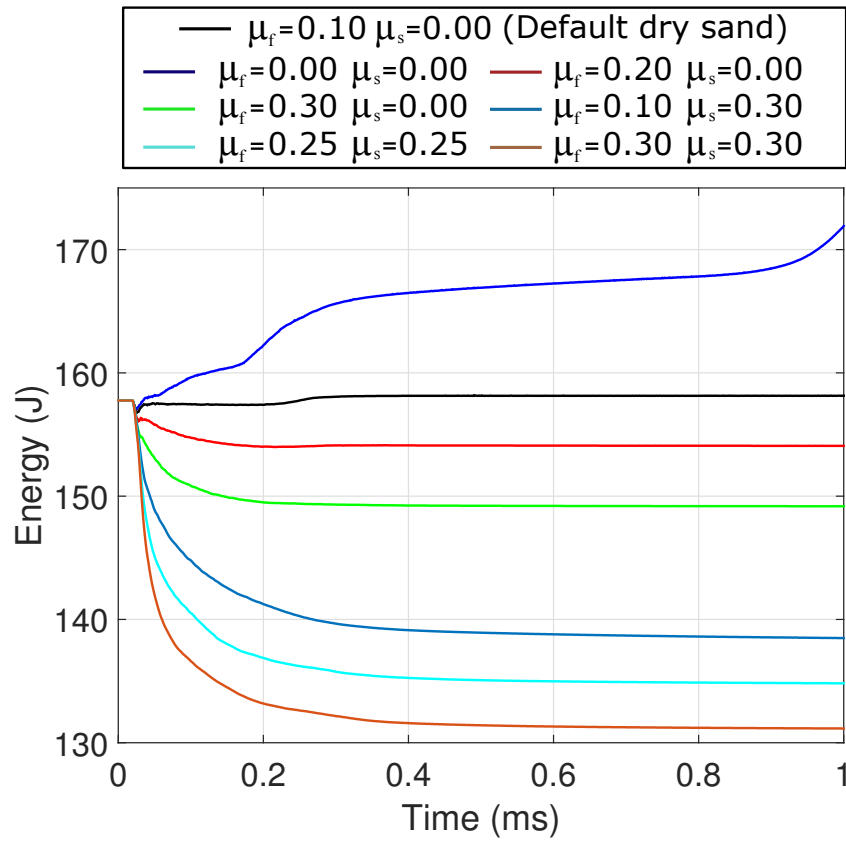


Figure 8.17: Energy balance for several values of soil-soil friction (μ_f) and soil-structure friction (μ_s).

Chapter 9

Discussion

The main objective with this study was to investigate how empty and sand-filled aluminium panels behave under impact loading. In addition an important task was to check whether the novel particle-based method implemented in IMPETUS Afea Solver is able to capture the main trends in the impact problem.

In the following the influence of different parameters and an evaluation of the predictability of the numerical simulations are discussed.

The Numerical Design Process

Optimization of protective systems for a certain bullet type, impact angle and granular filling can have unfortunate outcomes. It is difficult to anticipate the path of least resistance for every case without performing a comprehensive experimental study. The ultimate goal of this thesis is to accurately model impact problems in granular material and to be able to design protective structures without conducting expensive ballistic experiments. The accuracy of the numerical results depends strongly on the analyst's skill and assumptions. In the following the effects of several parameters are discussed with the objective of getting accurate but conservative results.

The numerical models for empty aluminium panels seems to overestimate the ballistic limit velocity. This is most likely due to the slanting web's increased effect when the bullet's kinetic energy drops. This leads to a rotation of the bullet and subsequently an oblique hit angle in the rear plate, increasing the total resistance of the aluminium panel. This effect is seen in the oblique impact angle study and the plate thickness study where small changes in plate thicknesses and oblique angles had a considerable effect on the ballistic limit velocity predicted from numerical simulations.

The lead tip and brass jacket are frequently neglected in numerical simulations to save computational time [18, 63]. This simplification has a significant effect on the ballistic limit velocity in this study where thin, soft plates are investigated. The plastic work done by the jacket and the separation process from the steel core have been shown to influence the results [5], so the full bullet should be modelled to capture these effects.

The contact friction coefficient between structural parts was selected to be 0.01, as suggested in Zukas et al. [10] for ballistic impact problems involving contact in metals. This parameter is repeatedly neglected to obtain conservative results in the numerical simulations [64]. A distinct change in the residual velocity was obtained between different friction parameters in the parameter study. In numerical simulations for design purposes, friction effects may be neglected to obtain conservative results.

The user defined parameter which elements are eroded if their critical time step drops below, Δt_{erode} , is selected to 2 ns in the bulk of the numerical simulations performed in this thesis. It is shown that a higher Δt_{erode} parameter will predict higher residual velocities. This effect should contribute to more conservative simulation.

Element size is of major importance when it comes to computational time and accuracy in the simulations. In the sensitivity study the effect of different meshes was tested. Single conclusions regarding the effect of resistance in the model is difficult to draw as both finer and courser meshes predicts lower residual velocities.

The discrete particle module consists of parameters that greatly affect the predicted resistance in the numerical model. In this thesis the soil-soil friction seems be the most dominant parameter, although all parameters in the module have an effect on the predicted residual velocity to some extent (Section 8.3). However, it is hard to conclude definitely about the conservative or non-conservative effect of each parameter as the parameter set needs to be calibrated as a whole. Overall conservative results are obtained in the numerical simulations for sand-filled panels, even though the calibrated material model for the B95 sand fraction ($d_s=1.0$ mm) gave non-conservative results overestimating the ballistic limit velocity by 5 %.

The Overall Evaluation of the Method

The discrete particle module is a phenomenological approach to the problem. Different grain shapes and multiple grain sizes are not incorporated in the particle module. Two simplifications in the rigid particle module are that the rotational degree of freedom and fracture of individual sand grains are neglected. The energy consumed by these phenomena can be represented as increased inner friction in the phenomenological model [5]. However, the objective is to capture the main behaviour of the impact problem rather than micromechanics in the sand grains.

The discrete particle method has shown excellent qualitative and quantitative results in this study. The capability to numerically recreate the component tests in the higher velocity regimes is exceptional. In low velocity impacts the particle module exhibits weakness to represent the resistance found in the component tests. The reason for this may be that the rheological model were proposed to investigate soil-structural interaction in landmine explosions where high rate deformations are present [15].

Two sets of material constants were calibrated from the component tests in the high velocity regime and used to model the particles for the sand-filled panel. The two calibrations with different particle diameter predicted different results regarding resistance

in the sand-filled panels, ranging from being conservative to non-conservative but still close to the ballistic experiments. Taking the complexity of the problem into account good agreement between experiments and numerical prediction are obtained. The model is able to capture the main trends in the impact problem.

As an alternative strengthening solution for use in protective structures, the sand-filled panels requires certainty to fulfill the relevant ballistic requirements. The lack of this ability could have fatal consequences and shows the importance of a conservative design rather than saving transportation weight and material costs. When the discrete particle-based model is used in design of protective systems including granular media a component test in the same velocity range may assist the analyst to get predictive results. Extra caution in the choices of input parameters should be taken as always if designing without relevant component tests.

The innovative aspects of this idea, both in terms of employing the discrete particle module in design of protective structures and the idea itself of utilizing local granular material from operational areas, seems like one step further in achievement of efficiency and reduced costs. The geometry and dimensions of the extruded aluminium panel and the combination with granular filling could most likely also be optimized to give enhanced capacity and a more reliable design process. This is an aspect which is not investigated in this thesis.

The investigation in this thesis shows that the design without the use of data from ballistic tests is restricted because of several required assumptions. However, the results looks promising when calibrating the material model from experiments in the relevant velocity regime.

Chapter 10

Concluding Remarks

This thesis investigates the effect three different fractions of granular media has on the ballistic properties of extruded AA6005-T6 panels perforated by 7.62 mm APM2 bullets. Sand fractions with median grain sizes of 0.15 mm, 0.55 mm and 0.95 mm were filled in the panel cavities and tested in the impact laboratory located at SIMLab, NTNU. Ballistic limit curves of the empty aluminium panels and in combinations with the three fractions of sand were obtained. Component experiments in different velocity domains were conducted to calibrate the discrete particle model. These component tests were modelled in IMPETUS Afea Solver and the parameters in the rheological sand model determined from the component test results. Complete numerical simulations of empty and sand-filled panels were conducted with good agreement to experimental results. Finally an investigation of the effects some of the numerical parameters had on the residual velocity was conducted on simplified numerical models.

The conclusions presented below are based on the statistically limited experiments conducted in this thesis. This is close to the term "one-shot statistics" referred to in Zukas and Scheffler [65]. Large spread in experiments involving granular material makes the calculated ballistic limit velocities uncertain, e.g. the ballistic limit velocities may be altered if a more statistically significant data set had been available.

A summary of the concluding remarks is listed below.

Experimental Results

- Experiments on empty panels adhere well to the Recht-Ipson equation, although a significant spread in bullet trajectory is seen for varying initial velocity.
- Filling the cavities in the AA6005-T6 aluminium panel can give significant improvement of the ballistic protection. In this thesis it is shown that the ballistic limit velocity is increased by at least 32.5 % when filling the cavities with quartz sand with a median grain size ranging from 0.15 mm to 0.95 mm.
- Differences in ballistic limit velocity between the three fractions of sand tested in

this thesis varied by approximately 7 %. The large spread in experimental data can be due to the varying material behaviour in granular media, packing density and local variations in uniformity of grain sizes.

- Fracture of sand grains was evident in the ballistic testing of sand-filled panels with the observation of fine white powder in the bullets trajectory, often referred to as the white trail.
- The calibration tests performed in the gas-gun facility were easily replicated with the IMPETUS Afea Solver. The 50 mm thick sand layer gave a rather stable residual velocity over the three tests performed. In average an initial velocity of $v_i=278.2$, and a residual velocity of $v_r=60.6$ were obtained.
- The mechanical impacts from the drop-tower gave penetration resistance data from the sand in the low velocity regime. A marked abrupt rise and fall in the force at the terminal portion of penetration in the tests was found. This has been seen in existing literature and may be related to a transition from inertial to frictional resistance.

Numerical Results

- The numerical calibration of the parameters in the rheological model of the discrete particle module was conducted mainly to the gas-gun component tests with excellent qualitative compliance. The tuning was primarily conducted by changing the friction between individual particles.
- The discrete particle module at the lowest penetration velocities showed lacking ability to reproduce the resistance found in the experimental tests. Furthermore, the module shows uncertainties in reproducing the experimental findings from different velocity regimes without re-tweaking the parameters in the rheological model.
- IMPETUS Afea Solver was able to capture many of the observed phenomena from the simulations of ballistic impact in the extruded aluminium panels. Sliding marks in the slanting web, rotation of bullet after perforation of the slanting web, ductile hole growth with thickening around the holes in the front and rear plate were among the observed phenomena.
- For empty aluminium panels, the bullet oblique hit angle was shown to have a major effect on the predicted resistance in the numerical simulations. The reduction in ballistic limit velocity was found to be approximately 17 % for a oblique angle of $\alpha=+3^\circ$.
- In the plates thickness study the total plate thickness was held constant, but the front and rear plate thicknesses were increased or reduced by 0.5 mm. These small variations in the respective plate thicknesses increased the ballistic limit by 3.2 % for thick front plate and reduced the ballistic limit velocity by 7.2 % for thick rear plate. The reason for this difference may be due to the change in impact velocity in the slanting web.

- All the numerical analyses with sand-filled panels gave conservative results with respect to the experimental testing, except from the calibrated material model for the B95 sand fraction with particle size, $d_s=1.0$ mm, which gave non-conservative results overestimating the ballistic limit velocity by 5 %.
- The sensitivity study gave an overview over the conservative or non-conservative effects for various parameters regarding front and rear plate, the slanting web and the rheological model of sand. The model seems to be most sensitive to change in element size, particle size and soil-soil friction coefficient.

Overall numerical results gives good agreement between experimental results and numerical prediction when taking the complexity of the problem into account. It is obtained predictable results in the numerical simulations for sand-filled panels when the parameters in the discrete particle model are calibrated through component tests in the appropriate velocity domain. It is also shown that small changes in geometry, oblique in bullet angle, soil-soil parameters and particle size greatly effects the predicted ballistic limit velocity.

Chapter 11

Further Work

The conclusions from this thesis indicate that there are still many aspects that requires further investigation in order to assess the validity of the results. In addition, lots of ideas were obtained while working on this, which we did not have time to study. Some of them will now be presented as suggestions for further work. This includes experimental and numerical proposals.

- **Experimental tests on saturated sand.** Ballistic experiments in the nominal ordnance range were performed on sand samples with the same almost nonexistent saturation degree. The sand will most likely be in wet state at a time in practical use, so the effect of impact to highly saturated sand would be interesting to check.
- **Compaction state.** Investigate the ballistic properties when the panels are filled of sand with different packing states. All experiments were performed with the same packing procedure in this thesis, so a further investigation would include the changes from different packing states of sand, e.g. in loose state.
- **Sand tests with initial velocity in the range of 500 m/s to 900 m/s.** Since the calibration of the numerical parameters is based on component tests from a lower velocity regime in this thesis, there are some uncertainties regarding the accuracy. Performing component tests with initial velocity in the range of 500 m/s to 900 m/s, giving the same strain/deformation rate as in the ballistic experiments, may give a more accurate calibration and a basis of comparison to the already conducted component tests. An even more accurate calibration could possibly be performed by shooting with the bullet core, such that more material uncertainties are avoided.
- **Investigate different impact points.** The only investigated impact point in this thesis was chosen to be such that the bullet hits the middle of the slanting web. Experimental tests of impact from several other positions and angles may be required to fully validate the ballistic properties from the extruded aluminium panel in combination with granular material.

- **Testing of the sand fractions in the geotechnical laboratory.** Component tests of the sand fractions could be compared to traditional testing procedures like uniaxial compression, Split Hopkinson Pressure Bar, triaxial compression or plane wave shock tests.
- **Run numerical simulations in another software.** The IMPETUS Afea Solver gave good results when combining the FEM-module and the DEM-module. However, it would be interesting to compare and verify against similar explicit nonlinear finite element software, if possible.
- **Check the effect of sand thickness.** In this thesis the material model was calibrated using a 50 mm thick granular sample, while the calibrated parameters was used to model a thickness of approximately 130 mm. This needs further validation by performing component tests on different sand thicknesses.
- **Investigation of the panel geometry.** Check the possibilities for an improved design of the geometry to the extruded aluminium panels. There are many possibilities regarding the geometry and dimensions of the plates and cavities that may give improved design. None of these are investigated in this thesis.

Bibliography

- [1] T. Børvik, S. Dey, and A.H. Clausen. Perforation resistance of five different high-strength steel plates subjected to small-arms projectiles. *International Journal of Impact Engineering*, 36:948 – 964, 2009.
- [2] T. Børvik, A.G. Hanssen, S. Dey, H. Langberg, and M. Langseth. On the ballistic and blast load response of a 20 ft ISO container protected with aluminium panels filled with a local mass — Phase I: Design of protective system. *Engineering Structures*, 30:1605 – 1620, 2008.
- [3] T. Børvik, L. Olovsson, A.G. Hanssen, K.P. Dharmasena, H. Hansson, and H.N.G. Wadley. A discrete particle approach to simulate the combined effect of blast and sand impact loading of steel plates. *Journal of the Mechanics and Physics of Solids*, 59:940 – 958, 2011.
- [4] H.N.G. Wadley, T. Børvik, L. Olovsson, J.J. Wetzel, K.P. Dharmasena, O.S. Hopperstad, V.S. Deshpande, and J.W. Hutchinson. Deformation and fracture of impulsively loaded sandwich panels. *Journal of the Mechanics and Physics of Solids*, 61:674 – 699, 2013.
- [5] T. Børvik, S. Dey, and L. Olovsson. Penetration of granular materials by small-arms bullets. *International Journal of Impact Engineering*, 75:123 – 139, 2015.
- [6] Wikipedia. Ballistics: <http://en.wikipedia.org/wiki/Ballistics>. Obtained in May 2015.
- [7] M. Omidvar, M. Iskander, and S. Bless. Response of granular media to rapid penetration. *International Journal of Impact Engineering*, 66:60 – 82, 2014.
- [8] D.E. Carlucci and S.S. Jacobson. *Ballistics*. CRC Press, 2 edition, 2013.
- [9] J.A. Zukas. Impact Dynamics: Theory and Experiment. Technical report, Army Ballistic Research Lab Aberdeen Proving Ground, 1980.
- [10] J.A. Zukas. *High velocity impact dynamics*. Wiley, New York, 1990.
- [11] M.E. Backman and W. Goldsmith. The mechanics of penetration of projectiles into targets. *International Journal of Engineering Science*, 16:1 – 99, 1978.

-
- [12] R. F. Recht and T. W. Ipson. Ballistic perforation dynamics. *Journal of Applied Mechanics*, 30:384–390, September 1963.
- [13] J.P. Lambert and G.H. Jonas. Towards Standardization in Terminal Ballistics Testing: Velocity Representation. Technical report, USA Ballistic Research Laboratories, Aberdeen Proving Ground, Maryland, 1976.
- [14] O.S. Hopperstad and T. Børvik. TKT4135 Material Mechanics - Lecture Notes Part 1. Booklet, 2013.
- [15] V.S. Deshpande, R.M. McMeeking, H.N.G. Wadley, and A.G. Evans. Constitutive model for predicting dynamic interactions between soil ejecta and structural panels. *Journal of the Mechanics and Physics of Solids*, 57:1139 – 1164, 2009.
- [16] S. Dey. *High-strength steel plates subjected to projectile impact : an experimental and numerical study*. PhD thesis, Structural Impact Laboratory, Department of Structural Engineering, Norwegian University of Science and Technology, Trondheim, 2004.
- [17] F. Grytten. *Low-Velocity Penetration of Aluminium Plates*. PhD thesis, Norwegian University of Science and Technology, Faculty of Engineering Science and Technology, Department of Structural Engineering, 2008.
- [18] J.K. Holmen and J. Johnsen. Effects of Heat Treatment on the Ballistic Properties of AA6070 Aluminium Plates. Master’s thesis, Norwegian University of Science and Technology, Faculty of Engineering Science and Technology, Department of Structural Engineering, 2012.
- [19] G.R. Johnson and W.H. Cook. A Constitutive Model and Data for Metals Subjected to Large Strains, High Strain Rates and High Temperatures. *Proceedings of the 7th International Symposium on Ballistics*, 7:541–546, 1983.
- [20] T. Børvik, O.S. Hopperstad, T. Berstad, and M. Langseth. A computational model of viscoplasticity and ductile damage for impact and penetration. *European Journal of Mechanics - A/Solids*, 20:685 – 712, 2001.
- [21] G.T. Camacho and M. Ortiz. Adaptive Lagrangian modelling of ballistic penetration of metallic targets. *Computer Methods in Applied Mechanics and Engineering*, 142:269–301, March 1997.
- [22] M.G. Cockcroft and D.J. Latham. Ductility and the Workability of Metals. *Journal of the Institute of Metals*, 96:33–39, 1968.
- [23] G.R. Johnson and W.H. Cook. Fracture characteristics of three metals subjected to various strains, strain rates, temperatures and pressures. *Engineering Fracture Mechanics*, 21:31–48, 1985.
- [24] R.D. Cook. *Concepts and applications of finite element analysis*. Wiley, New York, 2002.
- [25] IMPETUS Afea AS. IMPETUS Afea: <http://www.impetus-afea.com/>. Obtained in May 2015, 2015.

- [26] IMPETUS Afea AS. *IMPETUS Afea Solver, User guide & Commands*, 3.0b edition, March 2015.
- [27] M. Omidvar, M. Iskander, and S. Bless. Stress-strain behavior of sand at high strain rates. *International Journal of Impact Engineering*, 49:192 – 213, 2012.
- [28] H.M. Jaeger, S.R. Nagel, and R.P. Behringer. Granular solids, liquids, and gases. *Reviews of Modern Physics*, 68:1259–1273, 1996.
- [29] B. Robins. *New principles of gunnery : containing, the determination of the force of gun-powder, and an investigation of the difference in the resisting power of the air to swift and slow motions. By Benjamin Robins, ..* printed for J. Nourse, London, 1742.
- [30] P. Umbanhowar and D.I. Goldman. Granular impact and the critical packing state. *Physical review. E, Statistical, nonlinear, and soft matter physics*, 82:010301–, 2010.
- [31] Z. Chen, M. Omidvar, M. Iskander, and S. Bless. *Visualizing the Fundamental Physics of Rapid Earth Penetration Using Transparent Soils*, chapter 243, pages 2617–2626. American Society of Civil Engineers, 2015.
- [32] A.L. Collins, J.W. Addiss, S.M. Walley, K. Promratana, F. Bobaru, W.G. Proud, and D.M. Williamson. The effect of rod nose shape on the internal flow fields during the ballistic penetration of sand. *International Journal of Impact Engineering*, 38:951 – 963, 2011.
- [33] M.E. Backman. Terminal Ballistics, 1976.
- [34] R.V. Whitman. The response of soils to dynamic loading. Report No. 26, Final Report. Technical report, Massachusetts Inst. of Tech and Cambridge Dept. of Civil Engineering, 1970.
- [35] M.W. Emerson and Jr Hendron, A.J. Measurement of Stress and Strain during One-Dimensional Compression of Large Compacted Soil and Rockfill Specimens. Technical report, University of Illinois, 1971.
- [36] Q.M. Li and E.A. Flores-Johnson. Hard projectile penetration and trajectory stability. *International Journal of Impact Engineering*, 38:815 – 823, 2011.
- [37] H. M. Horn and D. U. Deere. Frictional Characteristics of Minerals. *Géotechnique*, 12:319–335(16), 1962.
- [38] B.E. Martin, W. Chen, B. Song, and S.A. Akers. Moisture effects on the high strain-rate behavior of sand. *Mechanics of Materials*, 41:786 – 798, 2009. Advances in the Dynamics of Granular Materials.
- [39] M. Iskander, E. Suescun-Florez, N. Machairas, and M. Baamer. *Strain Rate Dependency of Sand Response under Uniaxial Monotonic Loading*, chapter 18, pages 171–181. American Society of Civil Engineers, 2015.
- [40] C.W. Young. Penetration equations. Technical report, Sandia National Labs., Albuquerque, Oct 1997.

-
- [41] M.J. Forrestal and V.K. Luk. Penetration into soil targets. *International Journal of Impact Engineering*, 12:427 – 444, 1992.
- [42] P.A. Cundall. A discontinuous future for numerical modelling in geomechanics? *Proceedings Of The Institution Of Civil Engineers-Geotechnical Engineering*, 149:41–47, 2001.
- [43] G. Barla. Editorial. *Rock Mechanics and Rock Engineering*, page 1, August 2014.
- [44] J.E. Andrade, Q. Chen, P.H. Le, C.F. Avila, and T.M. Evans. On the rheology of dilative granular media: Bridging solid- and fluid-like behavior. *Journal of the Mechanics and Physics of Solids*, 60:1122 – 1136, 2012.
- [45] J.E. Hatch. *Aluminum : properties and physical metallurgy*. American Society for Metals, Metals Park, Ohio, 1984.
- [46] T. Børvik, A.H. Clausen, M. Eriksson, T. Berstad, O. S. Hopperstad, and M. Langseth. Experimental and numerical study on the perforation of AA6005-T6 panels. *International Journal of Impact Engineering*, 32:35 – 64, 2005. Fifth International Symposium on Impact Engineering.
- [47] P.K. Saha. *Aluminum extrusion technology*. ASM International, Materials Park, Ohio, 2000.
- [48] S.H. Park, H.S. Kim, and B.S. You. Prediction of grain size and yield strength of Mg-7Sn-1Al-1Zn alloys extruded at various temperatures and speeds. *Metals and Materials International*, 20:291–296, 2014.
- [49] Aalco Metals Ltd. Aluminium Alloy 6005A - T6 Extrusion Datasheet: <http://www.aalco.co.uk>. Obtained in May 2015, 2013.
- [50] Wikipedia. Sand: <http://en.wikipedia.org/wiki/Sand>. Obtained in May 2015.
- [51] International Organization for Standardization. ISO 14688-1 Geotechnical investigation and testing - Identification and classification of soil - Part 1: Identification and description, 2002.
- [52] R.D. Holtz, T.C. Sheahan, and W.D. Kovacs. *An introduction to geotechnical engineering*. Pearson, Upper Saddle River, 2011.
- [53] J. Borg, A. Van Vooren, H. Sandusky, and J. Felts. Sand Penetration: A Near Nose Investigation of a Sand Penetration Event. In Bo Song, Dan Casem, and Jamie Kimberley, editors, *Dynamic Behavior of Materials, Volume 1*, Conference Proceedings of the Society for Experimental Mechanics Series, pages 363–371. Springer International Publishing, 2014.
- [54] W.L. Cooper and B.A. Breaux. Grain fracture in rapid particulate media deformation and a particulate media research roadmap from the PMEE workshops. *International Journal of Fracture*, 162:137–150, 2010.
- [55] B.M. Das. *Advanced soil mechanics*. Taylor & Francis, London, 2008.

-
- [56] Wikipedia. Bullet: <http://en.wikipedia.org/wiki/Bullet>. Obtained in May 2015.
- [57] T. Børvik, A. Burbach, H. Langberg, and M. Langseth. On the ballistic and blast load response of a 20ft ISO container protected with aluminium panels filled with a local mass — Phase II: Validation of protective system. *Engineering Structures*, 30:1621 – 1631, 2008.
- [58] K. Watanabe, K. Tanaka, K. Iwane, S. Fukuma, K. Takayama, and H. Kobayashi. Sand Behavior Induced by High-Speed Penetration of Projectile. Technical report, Osaka University and Chubu University, 2011.
- [59] G.R. McDowell and M.D. Bolton. Effect of particle size distribution on pile tip resistance in calcareous sand in the geotechnical centrifuge. *Granular Matter*, 2(4):179–187, 2000.
- [60] J.K. Holmen, O.S. Hopperstad, and T. Børvik. Low-velocity impact on multi-layered dual-phase steel plates. *International Journal of Impact Engineering*, 78:161 – 177, 2015.
- [61] T. Børvik, L. Olovsson, S. Dey, and M. Langseth. Normal and oblique impact of small arms bullets on AA6082-T4 aluminium protective plates. *International Journal of Impact Engineering*, 38:577 – 589, 2011.
- [62] IMPETUS Afea AS. *IMPETUS Afea Solver, An introduction*, February 2015.
- [63] H. Thorsen and E. Orthe. Ballistic Perforation of Surface Hardened Mild Steel Plates. Master’s thesis, Norwegian University of Science and Technology, Faculty of Engineering Science and Technology, Department of Structural Engineering, 2014.
- [64] J. Johnsen, J.K. Holmen, O.R. Myhr, O.S. Hopperstad, and T. Børvik. A nano-scale material model applied in finite element analysis of aluminium plates under impact loading. *Computational Materials Science*, 79:724 – 735, 2013.
- [65] J.A Zukas and D.R Scheffler. Practical aspects of numerical simulations of dynamic events: effects of meshing. *International Journal of Impact Engineering*, 24:925 – 945, 2000.

Appendix A

Chemical Components and Sieve Analysis of Granular Media

Chemical composition and sieve analysis of the three granular materials used in this thesis are given below.

AB Baskarpsand
 Baskarp
 566 92 HABO

Beställningsnummer saknas
 Provets ankomstdatum 2008-11-25
 Analysen avslutad 2009-01-05

ANALYS AV SAND

Analys av provet har skett enligt överenskommelse. Uppslutning och kemisk analys har skett med ackrediterade metoder om sådana är tillgängliga. För sand baseras metoderna på BS 2975. Dock har atomabsorption har använts för slutbestämning av samtliga element, utom kisel.

För varje prov analyseras två delportioner och ett medelvärde beräknas. Mätosäkerheten anges i samma enhet som resultaten, normalt vikt% oxid.

Resultat i vikt% .

		Provbeteckning		
		B15		
Analysmetod	Analysparameter		Mätosäkerhet	Enhet
BS 2975:1988	Kisel	88,5	± 0,5	% SiO ₂
BS 2975:1988 mod.	Aluminium	6,3	± 0,3	% Al ₂ O ₃
BS 2975:1988 mod.	Järn	0,50	± 0,02	% Fe ₂ O ₃
BS 2975:1988	Kalcium	0,50	± 0,01	% CaO
BS 2975:1988	Magnesium	0,10	± 0,01	% MgO
BS 2975:1988	Natrium	1,39	± 0,03	% Na ₂ O
BS 2975:1988	Kalium	2,61	± 0,05	% K ₂ O
BS 2975:1988 mod.	Glödförlust vid 1000 °C	0,28	*	vikt %
-	Andel fri kvarts	72	*	vikt %
-	Sintringstemperatur	1225	± 25 *	°C

*Ackreditering saknas

Växjö den 8 januari 2009
GLASFORSKNINGSINSTITUTET


 Peter Sundberg
 Laboratoriechef

Denna rapport få endast återges i sin helhet, om inte utförande laboratorium i förväg godkänt annat

Glafo - glasforskningsinstitutet

Postadress	Besöksadress	Telefon	E-post / Internet	Bankgiro	PlusGiro	Org.nummer
Glafo	Vejdes plats 3	0470-76 70 50	info@glafo.se	470-3302	40258-6	556111-6855
Box 5157	352 52 Växjö		www.glafo.se			
350 05 Växjö						

AB Baskarpsand
 Baskarp
 566 92 HABO

Beställningsnummer saknas
 Provets ankomstdatum 2008-11-25
 Analysen avslutad 2009-01-05

ANALYS AV SAND

Analys av provet har skett enligt överenskommelse. Uppslutning och kemisk analys har skett med ackrediterade metoder om sådana är tillgängliga. För sand baseras metoderna på BS 2975. Dock har atomabsorption använts för slutbestämning av samtliga element, utom kisel.

För varje prov analyseras två delportioner och ett medelvärde beräknas. Mätosäkerheten anges i samma enhet som resultaten, normalt vikt% oxid.

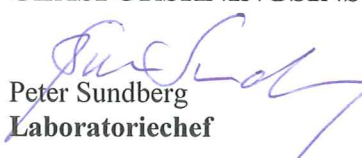
Resultat i vikt% .

Analysmetod	Analysparameter	Provbeteckning		
		B55	Mätosäkerhet	Enhet
BS 2975:1988	Kisel	90,1	± 0,5	% SiO ₂
BS 2975:1988 mod.	Aluminium	5,3	± 0,3	% Al ₂ O ₃
BS 2975:1988 mod.	Järn	0,57	± 0,02	% Fe ₂ O ₃
BS 2975:1988	Kalcium	0,42	± 0,01	% CaO
BS 2975:1988	Magnesium	0,11	± 0,01	% MgO
BS 2975:1988	Natrium	1,20	± 0,03	% Na ₂ O
BS 2975:1988	Kalium	2,06	± 0,04	% K ₂ O
BS 2975:1988 mod.	Glödförlust vid 1000 °C	0,30	*	vikt %
-	Andel fri kvarts	73	*	vikt %
-	Sintringstemperatur	1275	± 25 *	°C

*Ackreditering saknas

Växjö den 7 januari 2009

GLASFORSKNINGSINSTITUTET


 Peter Sundberg
 Laboratoriechef

Denna rapport få endast återges i sin helhet, om inte utförande laboratorium i förväg godkänt annat

Glafo - glasforskningsinstitutet

Postadress	Besöksadress	Telefon	E-post / Internet	Bankgiro	PlusGiro	Org.nummer
Glafo	Vejdes plats 3	0470-76 70 50	info@glaf.se	470-3302	40258-6	556111-6855
Box 5157	352 52 Växjö		www.glaf.se			
350 05 Växjö						

AB Baskarpsand
Baskarp
566 92 HABO

Beställningsnummer saknas
Provets ankomstdatum 2008-11-25
Analysen avslutad 2009-01-05

ANALYS AV SAND

Analys av provet har skett enligt överenskommelse. Uppslutning och kemisk analys har skett med ackrediterade metoder om sådana är tillgängliga. För sand baseras metoderna på BS 2975. Dock har atomabsorption använts för slutbestämning av samtliga element, utom kisel.

För varje prov analyseras två delportioner och ett medelvärde beräknas. Mätosäkerheten anges i samma enhet som resultaten, normalt vikt% oxid.

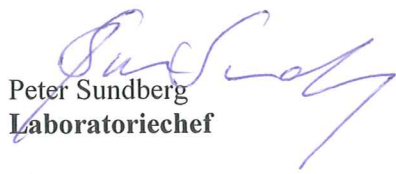
Resultat i vikt% .

		Provbeteckning		
		B95		
Analysmetod	Analysparameter		Mätosäkerhet	Enhet
BS 2975:1988	Kisel	77,1	± 0,5	% SiO ₂
BS 2975:1988 mod.	Aluminium	12,5	± 0,5	% Al ₂ O ₃
BS 2975:1988 mod.	Järn	1,42	± 0,05	% Fe ₂ O ₃
BS 2975:1988	Kalcium	1,03	± 0,02	% CaO
BS 2975:1988	Magnesium	0,34	± 0,01	% MgO
BS 2975:1988	Natrium	3,04	± 0,06	% Na ₂ O
BS 2975:1988	Kalium	4,19	± 0,08	% K ₂ O
BS 2975:1988 mod.	Glödförlust vid 1000 °C	0,60	*	vikt %
-	Andel fri kvarts	54	*	vikt %
-	Sintringstemperatur	1225	± 25 *	°C

*Ackreditering saknas

Växjö den 7 januari 2009

GLASFORSKNINGSINSTITUTET


Peter Sundberg
Laboratorieförman

Den här rapporten får endast återges i sin helhet, om inte utförande laboratorium i förväg godkänt annat

Glafo - glasforskningsinstitutet

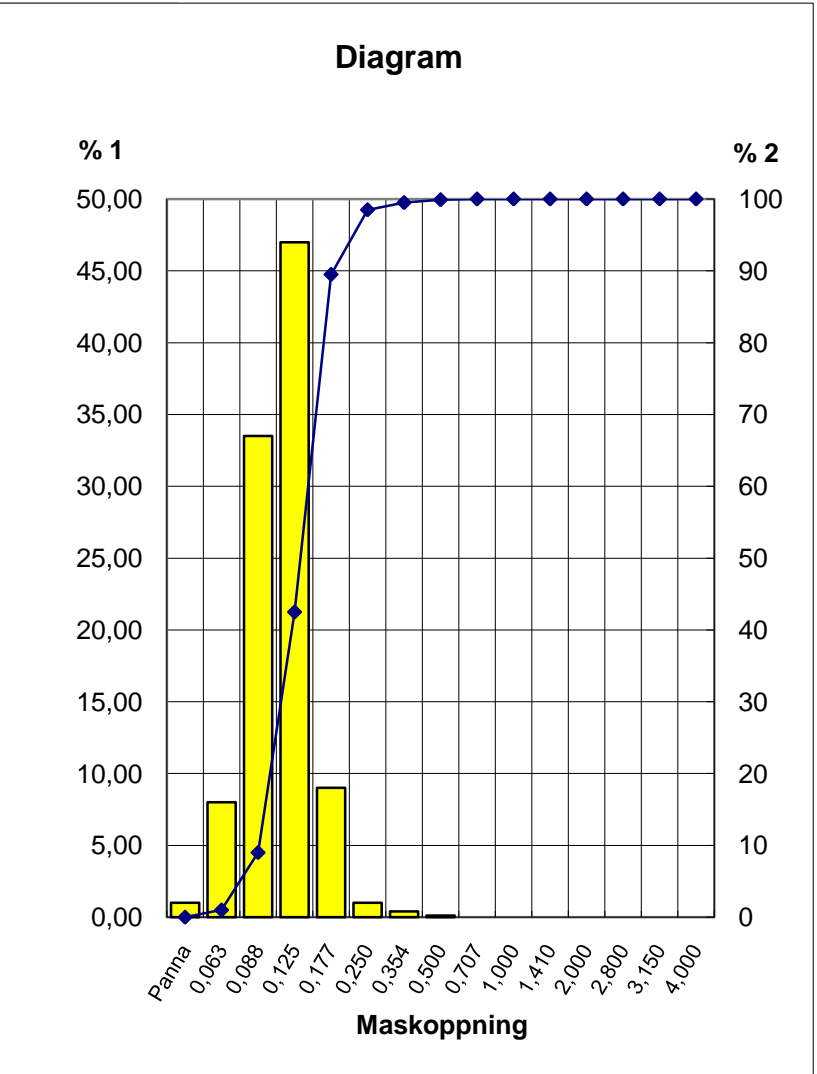
Postadress	Besöksadress	Telefon	E-post / Internet	Bankgiro	PlusGiro	Org.nummer
Glafo	Vejdes plats 3	0470-76 70 50	info@glaf.se	470-3302	40258-6	556111-6855
Box 5157	352 52 Växjö		www.glaf.se			
350 05 Växjö						

Baskarpsand

Siktanalys

Material:	B15	Datablad
Provplats:	Baskarp	

ASTM Sikt nr	Fraktion mm	Mängd 1) på sikt %	Mängd 2) genom sikt
5	4,000	0,00	100,00
	3,150	0,00	100,00
7	2,800	0,00	100,00
10	2,000	0,00	100,00
14	1,410	0,00	100,00
18	1,000	0,00	100,00
25	0,710	0,00	100,00
35	0,500	0,10	99,90
45	0,355	0,40	99,50
60	0,250	1,00	98,50
80	0,180	9,00	89,50
120	0,125	47,00	42,50
170	0,090	33,50	9,00
230	0,063	8,00	1,00
Panna	Panna	1,00	
Medelkornstorlek (mm)			0,146



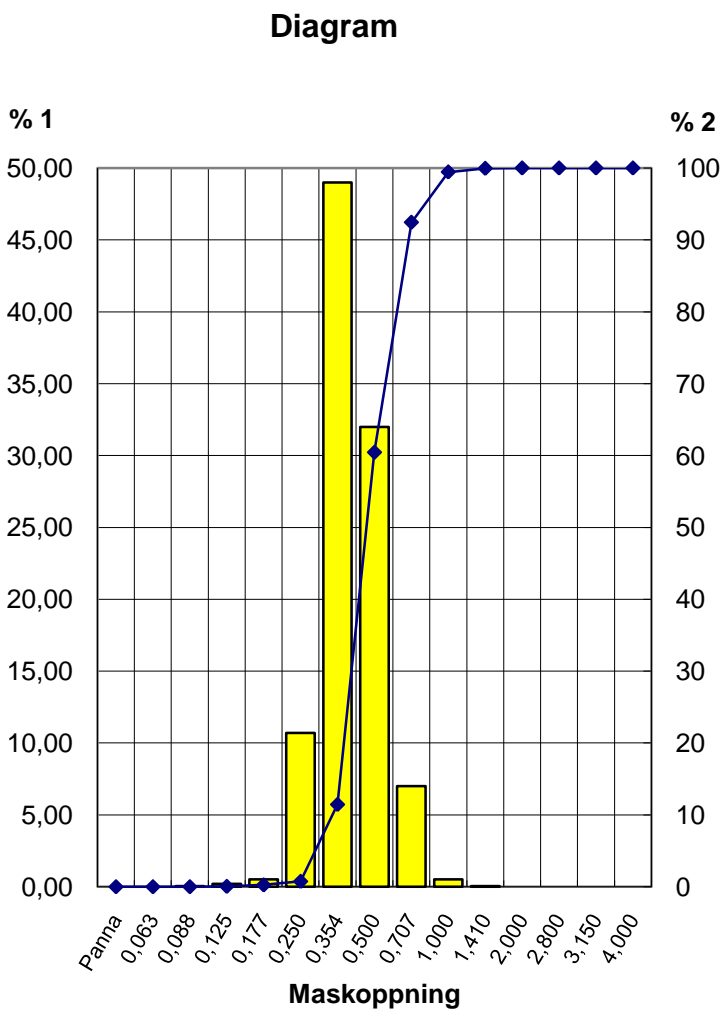
Anmärkning	Sign lab AH	Fastställdedatum 2008-04-29
------------	----------------	--------------------------------

Baskarpsand

Siktanalys

Material:	B55	DB
Provplats:	Baskarp	

ASTM Sikt nr	Fraktion mm	Mängd 1) på sikt %	Mängd 2) genom sikt
5	4,000	0,00	100,00
	3,150	0,00	100,00
7	2,800	0,00	100,00
10	2,000	0,00	100,00
14	1,410	0,05	99,95
18	1,000	0,50	99,45
25	0,710	7,00	92,45
35	0,500	32,00	60,45
45	0,355	49,00	11,45
60	0,250	10,70	0,75
80	0,180	0,50	0,25
120	0,125	0,20	0,05
170	0,090	0,05	0,00
230	0,063	0,00	0,00
Panna	Panna	0,00	
Medelkornstorlek (mm)			0,550



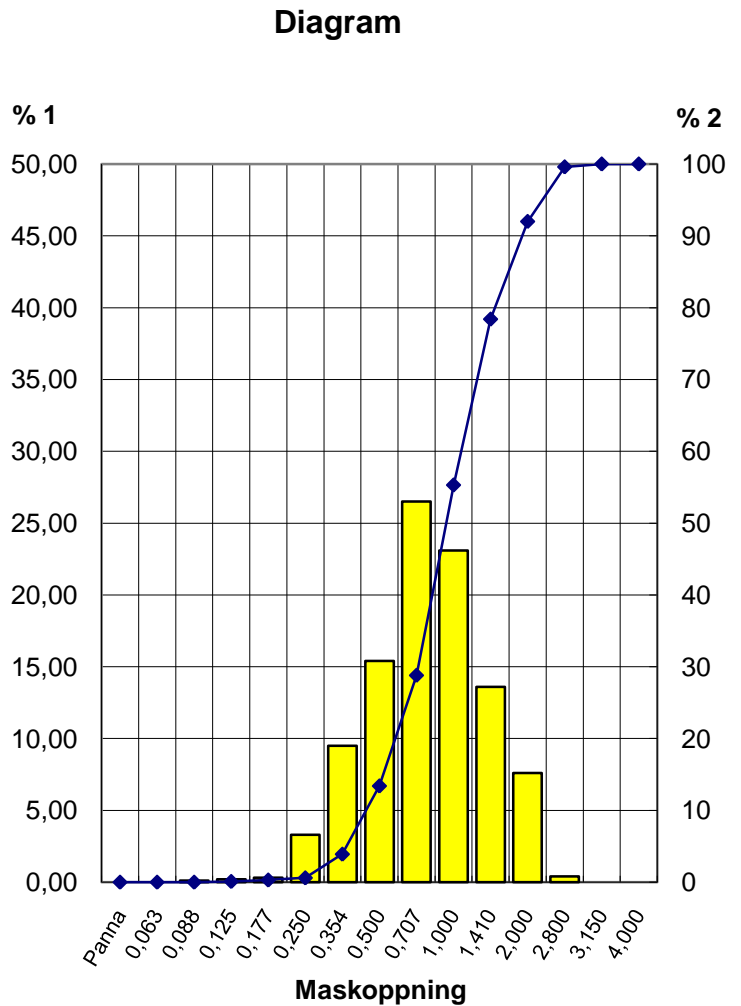
Anmärkning	Sign lab AH	Fastställdedatum 2008-09-26
------------	----------------	--------------------------------

Baskarpsand

Siktanalys

Material:	B95	Datablad
Provplats:	Baskarp	

ASTM Sikt nr	Fraktion mm	Mängd 1) på sikt %	Mängd 2) genom sikt
5	4,000	0,00	100,00
	3,150	0,00	100,00
7	2,800	0,40	99,60
10	2,000	7,60	92,00
14	1,410	13,60	78,40
18	1,000	23,10	55,30
25	0,710	26,50	28,80
35	0,500	15,40	13,40
45	0,355	9,50	3,90
60	0,250	3,30	0,60
80	0,180	0,30	0,30
120	0,125	0,20	0,10
170	0,090	0,10	0,00
230	0,063	0,00	0,00
Panna	Panna	0,00	
Medelkornstorlek (mm)		0,950	



Anmärkning	Sign lab AH	Fastställdedatum 2008-09-10
------------	----------------	--------------------------------

Appendix B

Water Content Calculations

	B15		B55		B95	
	dense	Loose	dense	Loose	dense	Loose
Measured density (kg/m ³)	1629.2	1431.0	1694.5	1514.9	1731.3	1552.9
Solid density* (kg/m ³)	2650.0	2650.0	2650.0	2650.0	2650.0	2650.0
Wet measured (g)	500.1	500.1	500.0	500.0	500.0	500.0
Dry measured (g)	498.0	498.0	498.4	498.4	498.5	498.5
Liquid volume (kg/m ³)	6.84	6.01	5.42	4.85	5.19	4.66
Sand volume (kg/m ³)	1622.3	1425.0	1689.0	1510.0	1726.1	1548.2
Volume of voids (air+liquid)	38.8 %	46.2 %	36.3 %	43.0 %	34.9 %	41.6 %
Volume of sand	61.2 %	53.8 %	63.7 %	57.0 %	65.1 %	58.4 %
Volume of air	38.1 %	45.6 %	35.7 %	42.5 %	34.3 %	41.1 %
Volume of liquid	0.68 %	0.60 %	0.54 %	0.48 %	0.52 %	0.47 %
Moisture content	0.42 %	0.42 %	0.32 %	0.32 %	0.30 %	0.30 %
Degree of saturation	1.76 %	1.30 %	1.50 %	1.13 %	1.49 %	1.12 %

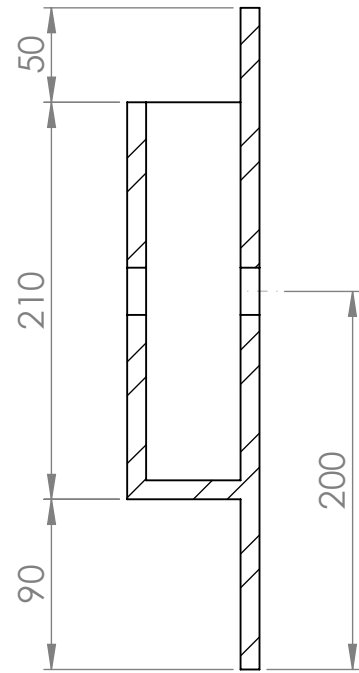
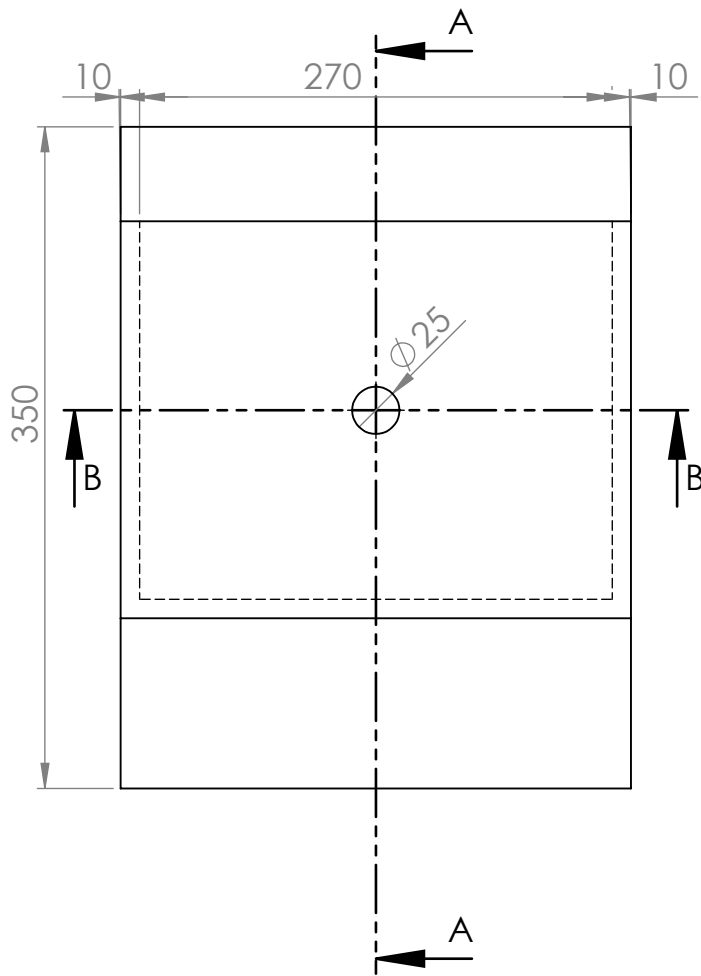
*From data sheet

Table B.1: Saturation degree calculation.

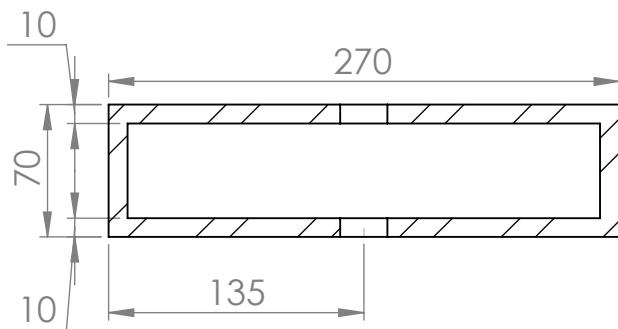
Appendix C

Sand container

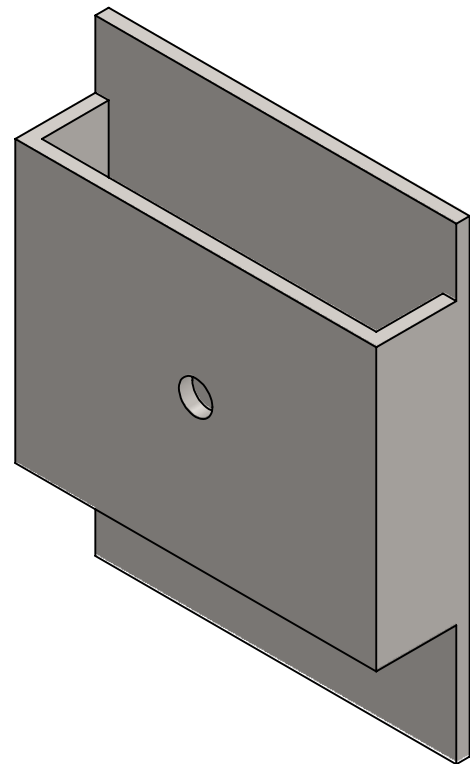
Drawings of sand container design by the authors and used to establish material constants in the rheological model for the sand grains.



SECTION A-A



SECTION B-B



**SolidWorks Student Edition
For Academic Use Only.**

MATERIAL:
Plain Carbon Steel
WEIGHT: 14330.02

PART:
Sand container
SCALE: 1:4

SHEET 1 OF 1

A4

Appendix D

IMPETUS Afea Solver Input Files

Input file for some of the simulations run in this thesis is given below:

- **C.1:** Base model aluminium panel filled with sand
- **C.2:** Sand container simulation

D.1 Extruded Aluminium Panel With Sand

The input-file for the base model including the aluminium panel, full bullet and 5 000 00 particules.

```

#-----
#
#           Extruded aluminium panel with sand
#
#-----
#-----
*UNIT_SYSTEM
SI
*PARAMETER
%v0           = 900.0           # Initial velocity
%termination_time = 4.0e-4           # Termination time
%time_erode     = 2.0e-9           # Element erosion time step
%flag_erode     = 0               # Erode flag
%contact_friction = 0.01          # Coulomb coefficient of friction
#Sand Parameters
%N              = 5000000         # Number of particles
%S_pack         = 1               # Packing
%S_density      = 1731.3          # Soil density
%S_stiff        = 4.0e8           # Soil-soil contact stiffness
%Structure_fr   = 0.30           # Soil-structure friction coefficient
%S_fr          = 0.25            # Soil-soil friction coefficient
%S_damp         = 0               # Soil-soil damping coefficient
*TIME
[%termination_time]
#-----
#           Including mesh
#-----
*INCLUDE
Mesh_4mm_4mm_3mm.k
0.001, 0.001, 0.001, 1000000
*INCLUDE
bullet.k
1, 1, 1
0, 0, 0, 0.025, 0.125, 0.1
0, -1, 0, 1, 0, 0
*INCLUDE
Dummy.k
0.001, 0.001, 0.001, 2000000, 2000000
0, 0, 0, 0, 0, 0.2
#-----
#           Defining geometry for refine and polynomial order
#-----
*GEOMETRY_PIPE
121
0.025, -0.02, 0.1, 0.025, 0.2, 0.1, 0.015
*GEOMETRY_PIPE
122
0.025, -0.02, 0.1, 0.025, 0.2, 0.1, 0.025
*GEOMETRY_BOX
123
-0.13, -0.02, -0.02, 0.13, 0.135, 0.22
*GEOMETRY_BOX
124
-0.13, 0, 0.0, 0.13, 0.135, 0.20
*COMPONENT_BOX
212, 6, 15, 1, 3
-0.14, -0.00325, .05, 0.14, -0.00975, 0
*COMPONENT_BOX
213, 6, 15, 1, 3
-0.14, -0.00325, .2, 0.14, -0.00975, 0.15
*GEOMETRY_PART

```



```

125
5
#-----
#           1 Material definition
#-----
#           1.1 Aluminium profile material properties:
#-----
*MAT_JC
1, 2700, 70000.0E6, 0.3, 11, 12
270.0E6, 134.0E6, 0.514, 0.008598, 0.703, 293, 893, 0.001
910, 0.9
*PROP_DAMAGE_JC
11, [%flag_erode]
0.06, 0.497, -1.551, 0.03412, 6.8, 1.0E-3, 293, 893
*PROP_THERMAL
12, 2.3e-5, 910, 0, 0.9, 293
#-----
#           1.2 Brass jacket material properties:
#-----
*MAT_JC
2, 8520, 115000.0E6, 0.31, 21, 22
206.0E6, 505.0E6, 0.42, 0.01076, 1.68, 293, 1189, 0.00005
385, 0.9
*PROP_DAMAGE_CL
21, 1
914.0E6
*PROP_THERMAL
22, 1.9e-5, 385, 0, 0.9, 293
#-----
#           1.3 Tip/cap material properties:
#-----
*MAT_JC
4, 10660, 10000.0E6, 0.42, 21, 22
24.0E6, 300.0E6, 1, 0.2293, 1, 293, 760, 0.00005
124, 0.9
*PROP_DAMAGE_CL
31, 1
175.0E6
*PROP_THERMAL
32, 2.9e-5, 124, 0, 0.9, 293
#-----
#           1.4 Bullet/lead core material properties:
#-----
*MAT_RIGID
3, 7800
*PSOIL
PS, 1, 123, 125, user, [%N], [%Structure_fr]

[%S_pack], [%S_density], [%S_stiff], [%S_fr], [%S_damp]
#-----
#           2.0 Parts
#-----
*PART
"profile"
1,1, , , , [%time_erode]
"jacket"
2,2, , , , [%time_erode]
"bullet"
3,3
"tip"

```

```

4,4, , , , [%time_erode]
"Clamp"
6,3
"dummy_sand"
5,3
#-----
#           3.0 Changing polynomial order of bullet and impact area
#-----
*CHANGE_P-ORDER
ALL, 0, 3, 122
#-----
#           4.0 Merging aluminium profile mesh
#-----
*MERGE_DUPLICATED_NODES
P, 1, P, 1, 0.0005
#-----
#           5.0 Refining hit point area
#-----
*REFINE
P, 1, 4, 121, 0
*REFINE
P, 1, 2, 122, 0
#-----
#           6.0 Smoothing bullet
#-----
*SMOOTH_MESH
PS, 2, 45, 1
#-----
#           6.0 Contact definition
#-----
*CONTACT
"General contact"
PS, 1, PS, 1, [%contact_friction], 1.0e15
1, 0.5
#-----
#           7.0 Boundary condition for clamping plates
#-----
*BC_MOTION
1
P, 6, XYZ, XYZ
#-----
#           8.0 Velocity definition
#-----
*INITIAL_VELOCITY
PS, 2, 0, [-%v0], 0
#-----
#           9.0 Part sets
#-----
*SET_PART
1
1,2,3,4,6
*SET_PART
"bullet"
2
2,3,4
#-----
#           THE END
#-----
*END

```

D.2 Circular Sand Box Simulation

Input-file for sand container simulations. Containing a projectile.

```

#-----
#           Sand parameter study
#
#           #Circular sand box#
#-----
#           0 Initializing
#-----
*UNIT_SYSTEM
SI
*PARAMETER
%termination_time =0.0010           # Termination time
%t                =0.002            # Plate thicknesses
%v0               =278.2             # Initial velocity
%bullet_st_off    =0.01             # Initial position for projectile
%bullet_rad       =0.005            # Projectile radius
%pl_st_off        =0.05             # Sand thickness
%p_r              =0.125            # Circular sand box radius
%hole_rad         =0.0125           # Radius for opening holes
#-----
#           Sand Parameters
#-----
%N                =2750000          # Number of particles
#Soil_type=user   # User defined soil parameters
%Structure_fric   =0.30             # Soil-structure friction coefficient
%S_packing        =1               # Soil packing scheme
%S_density        =1731.3           # Soil density
%S_stiffness      =4.0e8            # Soil-soil contact stiffness
%S_friction       =0.25             # Soil-soil friction coefficient
%S_damping        =0               # Soil-soil damping coefficient
*TIME
[%termination_time]
#-----
#           1 Plate, bullet and sand geometry
#-----
*COMPONENT_PIPE
10, 1, 1, 20, 6
0, 0, 0, 0, 0, [%t], [%p_r], [%hole_rad]
*COMPONENT_PIPE
20, 2, 1, 20, 6
0, 0, [-%pl_st_off], 0, 0, [-%pl_st_off-%t], [%p_r], [%hole_rad]
*COMPONENT_SPHERE
30, 3, 6
0, 0, [%bullet_st_off], [%bullet_rad], 0
*GEOMETRY_BOX
100
[-%p_r-0.05], [-%p_r-0.05], [-%pl_st_off-0.05], [%p_r+0.05], [%p_r+0.05], 0.05
*GEOMETRY_PIPE
200
0, 0, 0, 0, 0, [-%pl_st_off], [%p_r], 0
*GEOMETRY_PIPE
300
0, 0, [-%pl_st_off-0.05], 0, 0, 0.05, 0.04, 0
#-----
#           2 P-order and smoothing optimalization
#           for bullet and plate hole vicinity
#-----
*CHANGE_P-ORDER
ALL, 1, 3, 300
*SMOOTH_MESH

```

```

PS, 2, 45, 1
#-----
#           3 Part definition
#-----
*PART
"Initial_plate"
1, 1
"Residual_plate"
2, 1
"Bullet"
3, 1
#-----
#           3.1 Part sets
#-----
*SET_PART
1
1, 2
*SET_PART
2
1, 2, 3
#-----
#           4 Material definition
#-----
#-----
#           4.1 Sand holding plates
#-----
*MAT_RIGID
1, 7800
#-----
#           4.2 Soil definition
#-----
*PSOIL
PS, 2, 100, 200, user, [%N], [%Structure_fric]

[%S_packing], [%S_density], [%S_stiffness], [%S_friction], [%S_damping]
#-----
#           5 Contact definition and boundary conditions
#-----
*CONTACT
PS, 1, PS, 1, 0.01, 1.0e15
1, 0.5
*BC_MOTION
1
PS, 1, XYZ, XYZ
#-----
#           6 Initial velocity for bullet
#-----
*INITIAL_VELOCITY
P, 3, 0, 0, [-%v0]
#-----
#           THE END
#-----
*END

```

D.3 Sand Drop-Tower Simulation

```

#-----
#-----
#           Drop-Tower experiment
#           with hollow impactor
#
#-----
#-----
*UNIT_SYSTEM
SI
*PARAMETER
#----- Geometry measures
%P_h           = 0.35           # Height of sand cylinder
%P_r           = 0.0615        # Radius of sand cylinder
%Sand_filling  = 0.3           # Sand filling height
%Imp_rad       = 0.01          # Impactor radius
%Imp_length    = 0.13          # Impactor length
%Imp_distance  = 0             # Ini. impactor dist. from sand field
%Imp_thickn    = 0.002        # Thickness of hollow impactor walls
#----- Misc.
%Term_time     = 1.3E-2        # Termination time
%v0            = 2             # Initial velocity
%N_particles   = 4000000      # Number of particles
%Structure_frict = 0.3         # Soil-structure friction coefficient
#----- Sand parameters
%S_pack        = 1             # Soil packing scheme
%S_density     = 1731.3        # Soil density
%S_stiffness   = 4.0e8        # Soil-soil contact stiffness
%S_friction    = 0.25         # Soil-structure friction coefficient
%S_damping     = 0             # Soil-soil damping coefficient
*TIME
[%Term_time]
#-----
# Components and geometries
#-----
*INCLUDE
Impactor_mesh.k
0.001, 0.001, 0.001
0, 0, 0, 0, [%Imp_distance+%Sand_filling+%Imp_rad], 0
*COMPONENT_PIPE
1, 1, 18, 20, 1
0, 0, 0, 0, [%P_h], 0, [0.001+%P_r], [%P_r]
*COMPONENT_BOX
2, 2, 10, 1, 10
[-0.01-%P_r], -0.010, [-0.005-%P_r], [0.01+%P_r], 0.000, [0.01+%P_r]
*GEOMETRY_PIPE
10
0, 0, 0, 0, [%Sand_filling], 0, [%P_r], 0
*GEOMETRY_BOX
20
[-0.01-%P_r], -0.1, [-0.005-%P_r], [0.01+%P_r], [%P_h+0.1], [0.01+%P_r]
#-----
# Part definition
#-----
*Part
"Pipe"
1, 1
"Bottom"
2, 1
"Impactor"
5, 1

```

```

*SET_PART
"Sand container"
1
1, 2
*SET_PART
"Impactor"
2
5
#-----
# Materials
#-----
*MAT_RIGID
1, 320800.6568
*PSOIL
All, 1, 20, 10, user, [%N_particles], [%Structure_frict]

[%S_pack], [%S_density], [%S_stiffness], [%S_friction], [%S_damping]
#-----
# Smoothing and changing P-order
#-----
*Smooth_mesh
PS, 2, 45, 0
*CHANGE_P-ORDER
PS, 2, 3
#-----
# Velocity definition
#-----
*INITIAL_VELOCITY
PS, 2, 0, [-%v0], 04
#-----
# Gravity definition
#-----
*LOAD_GRAVITY
Y, 100
*FUNCTION
100
9.81
#-----
# Boundary conditions
#-----
*BC_MOTION
1
PS, 1, XYZ, XYZ
*BC_MOTION
2
PS, 2, ZX, XYZ
#-----
# END OF CONVERSATION
#-----
*END

```